6-21-2022

Non-Dominated Adaptive-Restart Genetic Algorithm Optimization of Tractive Induction Motor Rotor Bar Considering Dynamic Operation Through Center of Gravity Method

Tim Stachl
University of Windsor

Follow this and additional works at: https://scholar.uwindsor.ca/etd

Non-Dominated Adaptive-Restart Genetic Algorithm Optimization of Tractive Induction Motor Rotor Bar Considering Dynamic Operation Through Center of Gravity Method

By

Tim Stachl

A Thesis
Submitted to the Faculty of Graduate Studies
through the Department of Electrical & Computer Engineering
in Partial Fulfillment of the Requirements for
the Degree of Master of Applied Science
at the University of Windsor

Windsor, Ontario, Canada

2022

Non-Dominated Adaptive-Restart Genetic Algorithm Optimization of Tractive Induction
Motor Rotor Bar Considering Dynamic Operation Through Center of Gravity Method

by

Tim Stachl

APPROVED BY:

_____
H. Hu

Department of Mechanical, Automotive & Materials Engineering

_____
B. Balasingam

Department of Electrical & Computer Engineering

_____
N. C. Kar, Advisor

Department of Electrical & Computer Engineering

May 19, 2022

DECLARATION OF CO-AUTHORSHIP/PREVIOUS PUBLICATION

I hereby declare that this thesis incorporates material that is result of joint research, as follows:

This thesis contains the outcomes of publications which include the contributions of co-authors who were/are post-doctoral fellows, graduate students or associate professors under the supervision of Dr. Narayan C. Kar. In all cases, only my primary contributions towards these publications are included in this thesis. The contribution of co-authors was primarily with respect to refinement and editing process. In Chapter 2, I was the co-author in which I was actively part of experimental testing and assisted in data analysis. The model developed by the primary author, A. Fatima, in this publication is used by the proposed method and is therefore described in this chapter. Chapter 5, I was the co-author in which I applied the proposed method to predict dynamic performance characteristics. Only the sections with my personal contribution are included in this thesis to analyze the performance of the proposed method described in this thesis.

I am aware of the University of Windsor Senate Policy on Authorship and I certify that I have properly acknowledged the contribution of other researchers to my thesis, and have obtained written permission from each of the co-author(s) to include the above material(s) in my thesis. I certify that, with the above qualification, this thesis, and the research to which it refers, is the product of my own work. This thesis includes three original papers that have been previously published/submitted to journals for publication, as follows:

Thesis Chapter	Publication title/full citation	Publication status
Chapter 2	A. Fatima, **T. Stachl**, M. S. Toulabi; W. Li, J. Tjong, G. Byczynski, and N. C. Kar, "Permeance–Based Equivalent Circuit Modeling of Induction Machines Considering Leakage Reactances and Non–Linearities for Steady–State Performance Prediction," *IECON 2021–47th Annual Conference of the IEEE Industrial Electronics Society*, 2021, pp. 1-6.	*Published*
Chapter 3	**T. Stachl**, A. Fatima, M. S. Toulabi; W. Li, A. Lombardi, J. Tjong, and N. C. Kar, "Torque and Loss Optimized Rotor Bar Design for an Induction Machine Using a Nondominated Genetic Algorithm Through Objective Function Modeling," *IECON 2021–47th Annual Conference of the IEEE Industrial Electronics Society*, 2021, pp. 1-6.	*Published*
Chapter 5	B. D. S. G. Vidanalage, M. S. Toulabi, **T. Stachl**, A. Lombardi, J. Tjong, and N. C. Kar, "Winding Function-Based Analytical Modeling of Core Loss in an Induction Machine Considering Slotting Effects and the Frequency-Dependent B-H Curve Characteristics," *IEEE Transactions on Magnetics*, early access. 2022. doi: 10.1109/TMAG.2022.3148759.	*Published*

I certify that I have obtained a written permission from the copyright owner(s) to include the above published material(s) in my thesis. I certify that the above material describes work completed during my registration as a graduate student at the University of Windsor.

I declare that, to the best of my knowledge, my thesis does not infringe upon anyone's copyright nor violate any proprietary rights and that any ideas, techniques, quotations, or any other material from the work of other people included in my thesis, published or otherwise, are fully acknowledged in accordance with the standard referencing practices. Furthermore, to the extent that I have included copyrighted material that surpasses the bounds of fair dealing within the meaning of the Canada Copyright Act, I certify that I have obtained a written permission from the copyright owner(s) to include such material(s) in my thesis. I declare that this is a true copy of my thesis, including any final revisions, as approved by my thesis committee and the Graduate Studies office, and that this thesis has not been submitted for a higher degree to any other University or Institution.

ABSTRACT

New electric vehicles demand higher performing, more cost-effective electric motors leading to the tractive induction motor (IM) being a promising choice for electric vehicles. Tractive IMs, however, have lower torque densities and slightly lower efficiency due to losses incurred in the rotor must be improved through rotor bar optimization to improve torque and reduced losses considering dynamic operating conditions. Numerous design factors, material limitations and performance characteristics must be considered during the design of tractive IMs prompting the use of optimization algorithms capable of systematically optimizing multiple design aspects. Unfortunately, conventional optimization algorithms are time consuming, limited objectives and input variables and susceptible to function bias resulting in undesirable traits for IM optimization. Therefore, a novel, robust non-dominated adaptive restart genetic algorithm capable of geometric rotor bar optimization considering dynamic operation is developed and proposed. To attain the desired optimization algorithm and optimal rotor bar geometry, this thesis: (1) Analyzes the challenges of IM design optimization, identifying optimization targets and design constraints. (2) Investigates and selects an optimization algorithm fit for IM design applications. (3) Proposes novel hyperbolic tangent based objective functions ensuring non-dominated solution. (4) A new adaptive restart genetic algorithm is developed with enhanced resistance to stalling minimizing run time. (5) The novel algorithm is implemented to optimize the torque and losses producing an optimal rotor bar which is validated and compared to a baseline IM. The proposed method is applicable to various IM topologies for multiple objective targets.

DEDICATION

This thesis is dedicated to my other half, Miranda, and my family, Mara, Sonja, Chris and Tala. I love you all very much. Thank you for all your understanding, motivation, strength and support along the way. I would not have made it to where I am now without all of you.

To my friends who never failed to brighten my day, thank you gators. I appreciate and love you all. $20 to the first one of you to read it cover to cover!

ACKNOWLEDGEMENTS

TABLE OF CONTENTS

LIST OF TABLES

LIST OF FIGURES

LIST OF ABBREVIATIONS

Abbreviation	Description
EV	Electric Vehicle
GHG	Greenhouse Gas
IEA	International Energy Agency
iZEV	Zero Emissions Vehicle Infrastructure Program
IM	Induction motor
PMSM	Permanent Magnet Synchronous Motor
OA	Optimization Algorithm
ECM	Electric Equivalent Circuit
MEC	Magnetic Equivalent Circuit
FEA	Finite Element Analysis
PECM	Permeance Based Equivalent Circuit Model
PS	Parametric Search
PSO	Particle Swarm Optimization
GA	Genetic Algorithm
OF	Objective Function
HWFET	Highway Fuel Economy Test Cycle
WLTC	Global Harmonized Test Cycle
DUT	Device Under Test
DYNO	Dynamometer

NOMENCLATURE

Variable	Description
S_1	Number of stator slots
S_2	Number of rotor bars
P	Number of poles
m	Number of phases
L_{ub}	Local upper bound
L_{lb}	Local lower bound
j	Input variable index
$iter$	Current iteration
$x_{\min}$	Best known location to the individual
K_{red}	Reduction factor
$step$	Step size
res	Search resolution
v_{ij}	Particle velocity
i	Individual or particle index
G_{min}	Global best-known location
x_{ij}	Current particle position
λ_r	Rotor slot permeance
λ_z	Rotor zigzag leakage permeance
λ_t	Rotor tooth top leakage permeance
X_2	Total rotor slot reactance
$R_{r\,dc}$	DC rotor bar resistance
ρ_{Al}	Resistivity of aluminum
T_{ph}	Turns per phase
p	Poles
$R_{2\,ac}$	AC rotor bar resistance
f	Operating frequency
L	Axial length
Q	Poles per phase

y_r	Rotor slot pitch
l_{eg}	Effective air gap
SA_b	Rotor bar cross sectional area
h	Rotor bar heights
W	Rotor bar widths
kw_s	Stator winding factor
ξ	Current penetration depth
K_c	Carters coefficient
T_{out}	Output torque
ω_s	Synchronous frequency
V_g	Air gap voltage
R_2	Rotor resistance
s	Rotor slip
P_{loss}	Total losses
P_{out}	Output power
P_{in}	Input power
η	Efficiency
OF_{tor}	Torque based OF
OF_{loss}	Loss based OF
T_{ref}	Reference torque
P_{ref}	Reference losses
gen	Current generation
K_{Bias}	Bias factor
K_{tor}	Torque scaling factor
K_{loss}	Loss scaling factor
c_j	Centroid with respect to each input variable
P_{surf}	Predicted core loss surface
ε_{rsm}	RMS error
B	Flux density
P_{curve}	Predicted core loss curve

L_r	Rolling resistance
K_{roll}	Rolling coefficient
G_{curb}	Vehicle curb weight
α	Road gradient
L_a	Aerodynamic resistance
ρ	Air density
c_{drag}	Drag coefficient
SA	Vehicle frontal area
v	Vehicle speed
L_g	Gradient resistance
L_i	Inertial resistance
a	Acceleration
t_{step}	Time step
E_c	Centroid energy consumption
r	Sub-region index
T_c	Centroid torque
v_c	Centroid speed
N_i	Number of individuals
N_r	Number of sub regions
T_{best_r}	Best known torque of the sub region
P_{best_r}	Best known losses of the sub region

CHAPTER 1   Introduction

1.1. Electric Vehicles–A Green Form of Personal Transportation

In the area of personal transportation, advances in vehicle electrification have allowed the use of electric vehicles (EVs) to become more popular. EVs exhibit several advantages over conventional combustion engine powered vehicles, the most obvious of which is that EVs depend on a renewable energy source, no longer relying on gas or diesel for fuel. As a result, EVs produce zero emissions which can significantly contribute to reducing the greenhouse gas (GHG) emissions in the private transportation sector. The transportation sector was the second largest contributor to Canada's GHG emissions in 2018, as seen in Fig. 1.1(a) [1], [2] and has been a major contributor to the production of harmful gasses such as carbon monoxide over the last 30 years, as shown in Fig. 1.1(b).
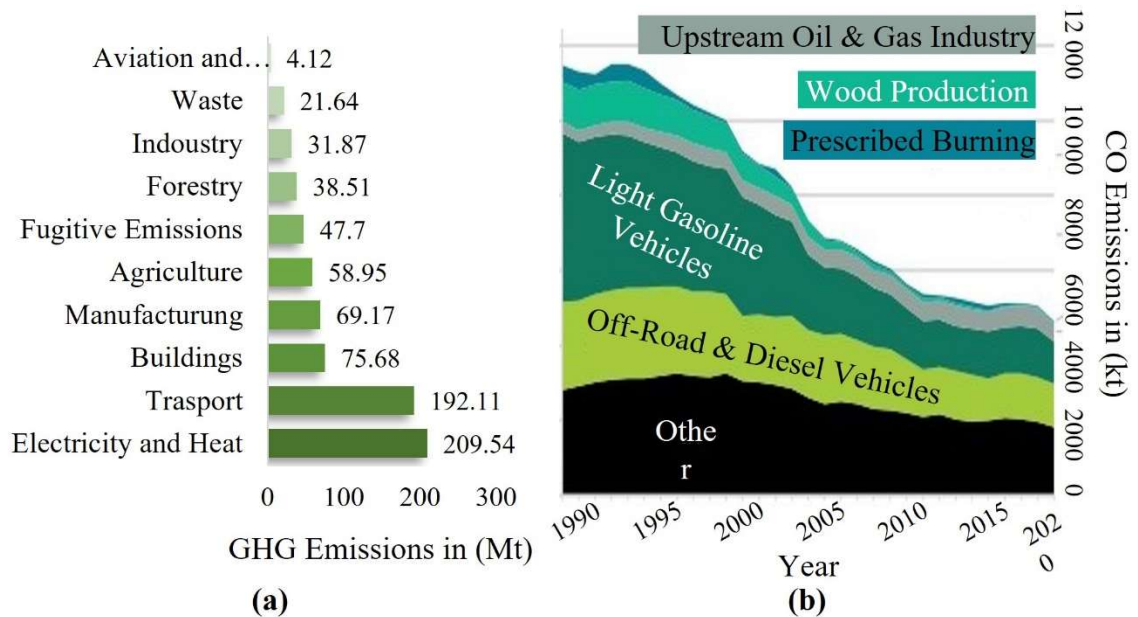
Fig. 1.1. Demonstrates the significance of passenger vehicle emissions. (a) The GHG emissions produced in Canada by sector in 2018. (b) The falling trend of Canadian carbon monoxide emissions by sector from 1990 to 2020. [1], [2]

Increased use of EVs has already had an impact on greatly reducing the total emissions produced not only by fossil fuel burning vehicles but also a decreased demand on the oil extraction and refinement industry which is also a leading contributor to GHGs [1], [3], [4]. In addition to the environmental benefits EVs have, they are also much quieter than combustion engines. This greatly reduces the noise pollution caused by combustion vehicles, especially in large cities leading to an improvement in the quality of life for the city's residents. EVs also require less maintenance as there are fewer moving mechanical parts as a result of the tractive electric motor used to power the vehicle. The unique design of the electric motor used by an EV allows the motor to spin the axel of the vehicle directly without the need for a gear box, meaning no mechanical losses are experienced by the drive system adding to the overall efficiency of EV systems [5], [6]. This also results in no torque drops as a result of gear changes enabling smooth vehicle acceleration comparable to high performance combustion vehicles at much more affordable prices. All EVs drive systems are comprised of three main components [7]–[9] as seen in Fig. 1.2. The battery of the EV
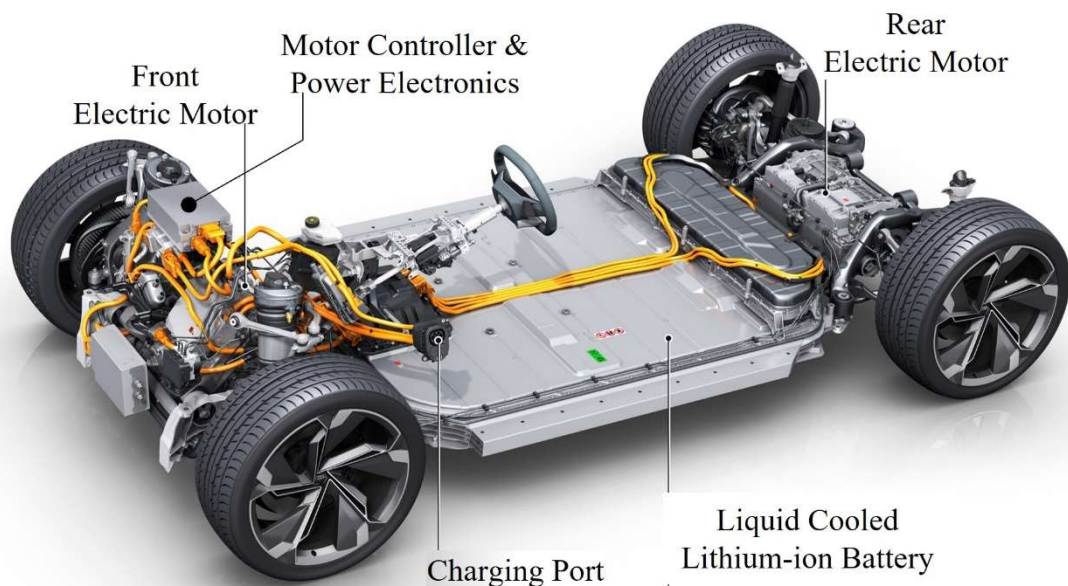
Fig. 1.2. Depicts the major components and relative configuration of tractive EVs. [7]

2

is used to store electrical energy on board the vehicle, which can then be discharged during operation. The capacity of the battery limits the amount of energy that can be stored by the vehicle and therefore limits the amount of energy that can be consumed by the electric motor and power electronic device. The purpose of power electronic devices is to convert the direct current supplied by the battery of the vehicle into a controlled input to the electric motor with respect to the demand of the vehicle's driver [10]. Power electronic devices are known to consume very little power with operating efficiencies as high as 99.8% in the case of industry leading EVs [11]–[14] meaning the majority of the power sored in the battery will be used to operate the electric motor. Therefore, the efficiency of the electric motor plays a large role in determining the total range of the EV with respect to the size of the battery. With increasing support from governments and private institutions, research into improving EVs in every aspect is sure to rapidly increase the quality and performance of EVs available on the market in the coming future.

1.1.1. A Surging Interest in Electric Vehicles

The global interest in EVs has greatly increased over the past decade through the initiatives set by global organizations and international governments supporting the growth of the EV industry and the switch to renewable energy-based transportation [15], [16]. The EV30@30 Campaign was initiated in 2017 by the Clean Energy Ministerial and backed by fourteen countries, including Canada, and 30 international companies and organizations setting a collective goal of EVs holding at least a 30% market share in every country by 2030 [17]. The EV30@30 Campaign stands on five actions, including supporting and tracking the development of EV charging stations while sparking public and private sector interest through incentives and commitments. The research and development of EVs are

fueled by increasing policy research and information exchanges as well as supporting governments through training and capacity building. The last goal of the initiative is to establish the Global Electric Vehicle Pilot City Program aimed at achieving 100 cities globally converted to EV friendly cities to provide a model and learning opportunity for EV infrastructure. Global initiatives such as this have led to the exponential increase in the EV stock between 2010 and 2020 [18] as demonstrated in Fig. 1.3 and the number of vehicle registrations and market share depicted in Fig. 1.4 [19]. One of the primary driving forces behind EVs interests in Canada is the global ecological benefits in that EVs have the potential to reduce GHG emissions by the transportation sector of society. To maintain the Sustainable Development Scenario, 2000 to 2030 developed by the International Energy Agency (IEA) [20], encouraging the shift to EVs would greatly reduce the emissions of passenger road vehicles and road freight sectors which are the primary contributors to GHG emissions such as carbon dioxide as seen in Fig. 1.5. Numerous incentives have been put into effect by the Canadian government to increase the popularity
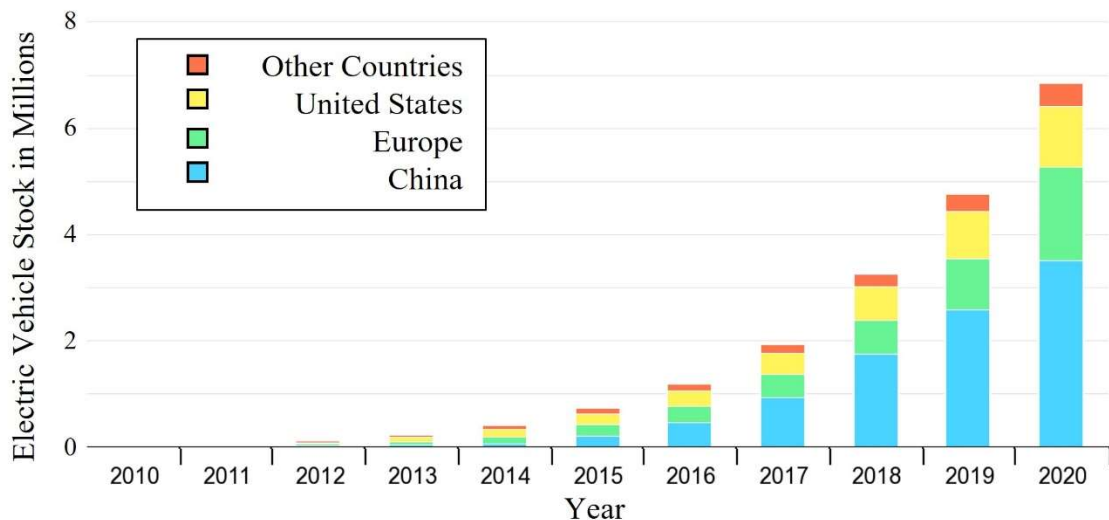
Fig. 1.3. Indicates the exponential growth of the global EV stock from 2010 to 2020. China is seen to hold the largest EV stock as of 2020. [18]

4
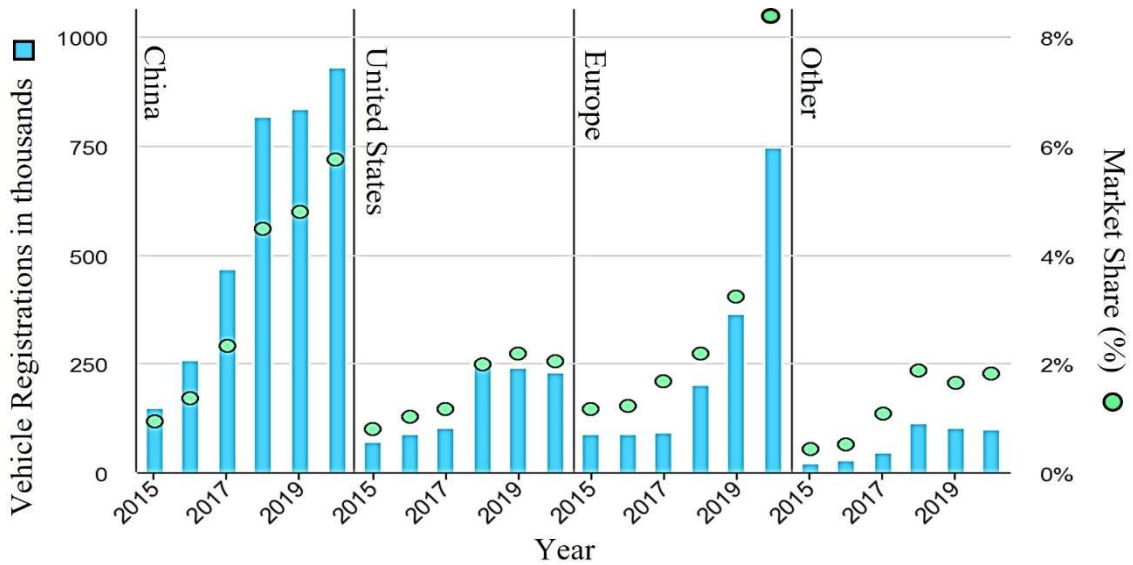
Fig. 1.4. The number of global EV registrations in various regions is depicted against the total vehicle market share held by EVs. [19]

of EVs, including a $150 million CAD Zero Emissions Vehicle Infrastructure Program (iZEV) focused on the installation of fast charging stations for apartments and workplaces as well as improving the charging infrastructure within Canada. Areas with high traffic, such as cities and highways, are being equipped with rapid charging stations available to EV owners, as well as priority lanes and parking in high traffic areas. The Canadian government also offers $5,000 [21] in purchase incentives for individuals purchasing a new
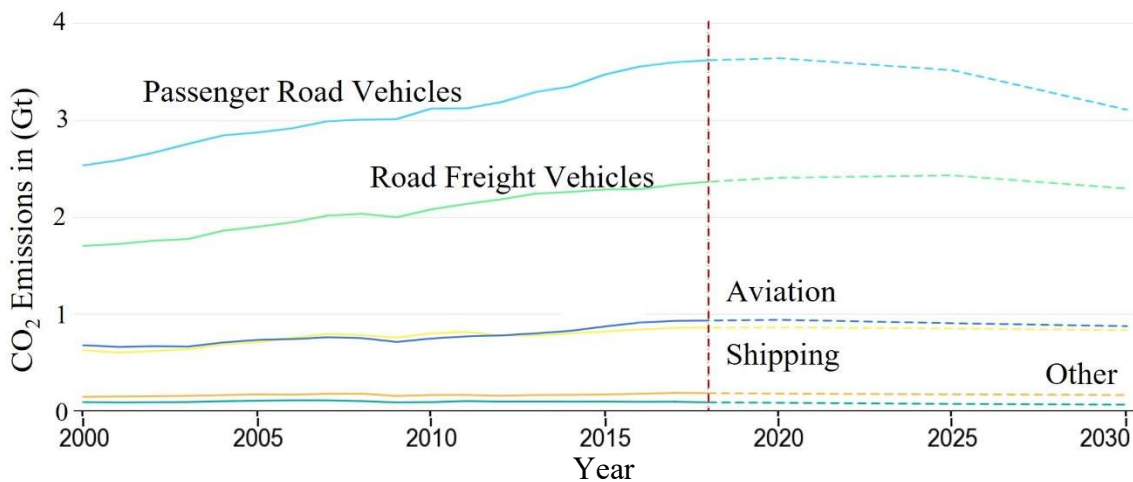
Fig. 1.5. Under the Sustainable Development Scenario, the global CO2 emissions are forecasted to decrease after its implementation in 2017. [20]

5

EV as well as providing businesses with opportunity tax incentives on the purchase of EV fleets for transportation and shipping. As a result of this incentivized program, the sales share of zero emissions vehicles has risen from 2.3% in 2018 to 3.1% in 2019 to 3.8% in 2020. In more recent developments, Stellantis North America COO has announced they will be updating and retooling automotive assembly plants in Windsor and Brampton, Ontario expanding the plants' capabilities to produce EVs and EV batteries. The $3.6 billion dollar investment will also lead to large amounts of funding for the research and development centers for all aspects of EVs [22]. This influx of funding and cutting-edge research will rapidly improve the quality and performance of EVs.

1.1.2. Industry Leading Electric Drive System for Tractive Applications

As the global interest in EVs increases and markets begin to shift away from combustion engines, the number of EVs will increase, and the performance of EVs will significantly increase as companies compete to dominate the market. The global market shares seen in Fig. 1.6 [18] held by leading automotive companies with respect to the EV

Fig. 1.6. The global overview of EV manufacturers with respect to market share held by manufacturer. [18]

6

market in 2021 shows Tesla held the largest market share of 13.84%, followed by the VW Group with an 11.28% share. As consumer demand continues to increase, EV market will become flooded with new EV models, as indicated by Fig. 1.7, which shows the number of EV models globally from 2015 to 2020 [19] to compete for a place in the market. This competition leads to the rapid improvement of the major limitations of EVs, such as the vehicle range, which is also greatly improved as a result of design, material and process improvements. Through the analysis of the current EV topologies, performance targets can be set with respect to motor type, drive configuration, market pricing and range to ensure new EVs are competitive within the market. Therefore, Table 1.1 provides an overview of crucial factors such as the cost, range and motor type of the 2022 Audi e-tron, 2022 BMW iX3, 2022 Hyundai Ioniq 5, 2022 Ford Mustang Mach-E and the 2022 Tesla Model X [23]–[25]. Similar vehicle types were chosen for this analysis to ensure a fair comparison between all 5 models. The analysis shows that the usable battery capacity of the average
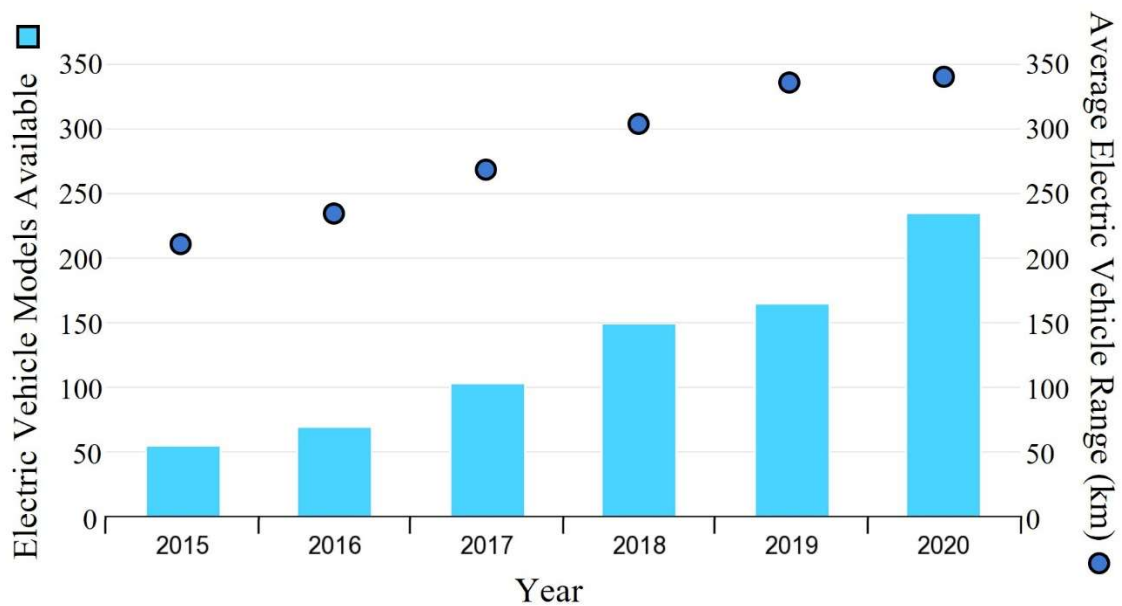
Fig. 1.7. Demonstrates the increase in average EV range as more models become available to consumers over a five-year period from 2015 to 2020. [19]

7

current EV is between 70 and 90 kWh while the range lies between 400 to 500 km. The vehicle weight and charging capacity are relatively similar across all models, while the peak torque and power are between 400 to 670 Nm and 210 to 325 kW, respectively. The Highest peak torque and the output power were produced by the 2022 Audi e-tron, which utilizes two tractive induction motors (IMs) to generate an acceleration time of 5.7 seconds. This has caused the range of the vehicle to suffer as its total range is the lowest therefore, if the operating efficiency of the vehicle could be increased, while the torque and power density are also increased, the acceleration time may be further reduced to compete with the leading acceleration of the Tesla Model Y which also features an IM. EVs featuring IMs are also capable of higher top speeds, as seen by the 200 km/h and 217 km/h top speeds of the Audi e-tron and Tesla Model Y, respectively.

TABLE 1.1

COMPARISON BETWEEN 2022 ELECTRIC VEHICLES [23]–[25]

Vehicle Specifications	Audi e-tron	BMW iX3	Ford Mustang Mach-E	Hyundai Ioniq 5	Tesla Model Y
Base Price (CAD)	111,655	92,201	87,269	66,993	82,152
Drive Configuration	Dual Motor AWD	Single Motor RWD	Dual Motor AWD	Dual Motor AWD	Dual Motor AWD
Motor Type (F=front, R=Rear)	F: IM R: IM	PMSM	F: PMSM R: PMSM	F: PMSM R: PMSM	F: IM R: PMSM
Battery Capacity	95 kWh	80 kWh	98.7 kWh	72.6 kWh	82 kWh
Usable Battery Capacity	86.5 kWh	74 kWh	88 kWh	70 kWh	75 kWh
Average Range (Mild Temp.)	410 km	440 km	475 km	425 km	505 km
Average Range (Cold Temp.)	315 km	325 km	360 km	315 km	365 km
Acceleration (0 to 100 km/h)	5.7 s	6.8 s	5.8 s	5.2 s	5 s
Top Speed	200 km/h	180 km/h	180 km/h	185 km/h	217 km/h
Energy Consumption (Mild Temp.)	211 Wh/km	168 Wh/km	185 Wh/km	165 Wh/km	149 Wh/km
Energy Consumption (Cold Temp.)	275 Wh/km	228 Wh/km	244 Wh/km	222 Wh/km	205 Wh/km
Peak Torque	664 Nm	400 Nm	580 Nm	605 Nm	493 Nm
Peak Power	300 kW	210 kW	258 kW	225 kW	324 kW
Vehicle Weight	2565 kg	2260 kg	2218 kg	2095 kg	2054 kg
Vehicle Height	1.616 m	1.668 m	1.625 m	1.605 m	1.624 m
Vehicle Width	1.935 m	1.891 m	1.881 m	1.89 m	1.921 m
Fast-Charger Average Power	146 kW	100 kW	90 kW	185 kW	110 kW
Fast-Charge Rate	590 km/h	490 km/h	410 km/h	910 km/h	600 km/h
Fast-Charge Time (10 to 80%)	26 min	33 min	43 min	17 min	30 min

1.2. State of the Art Electric Motors for Tractive Applications

The ideal motor for tractive applications is able to produce the operating conditions described by torque-speed curve depicted in Fig. 1.8 [26] which represents the operating regions of tractive electric motors. The constant torque region spans from starting to the rated speed of the motor [27]. If the synchronous speed is increased past the rated speed of the motor, the maximum torque will begin to decrease as the speed continues to increase. This tradeoff between speed and torque occurs as a result of the current in the rotor bars being reduced. The reason the current ion rotor bars must be reduced is to avoid magnetic field weakening and over voltage caused by high levels of flux saturation within the stator and rotor core. In this operating region, it is the output power that remains constant over the entire region, and therefore the second operating region of tractive IMs referred to the field weakening or constant power region. To maximize the performance of an IM for tractive applications, every aspect of the electromagnetic design must be considered.
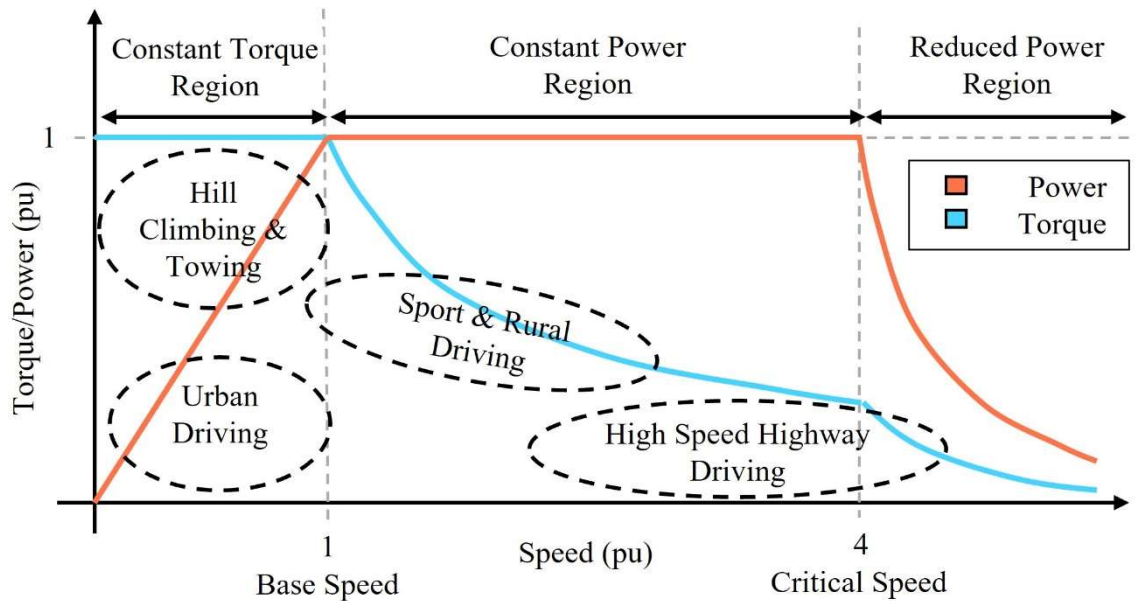
Fig. 1.8. Depicts the desired torque and power performance required by different operating regions that appear in tractive applications.

Under operating speeds less than the base speed, constant torque can be delivered to the vehicle by the motor, which is useful for urban and aggressive driving as well as low speed hill climbing. The constant power operating region corresponds to high-speed highway and sport driving while the motor delivers constant power with respect to the speed and torque of the motor. Lastly, the reduced power region represents operation past 4 times the base speed of the electric motor resulting in reduced power and torque as the speed continues to increase. To ensure the power demands of Fig. 1.8 can be met, tractive electric motors are designed for high torque and power density to generate high starting torque for low-speed operation and high-power capabilities at high speeds. The constant power region is generally considered to be approximately 3 to 4 times the size of the constant torque region to provide a reasonable compromise between the peak torque requirements of the vehicle and the rating of the required inverter. High efficiency operation is essential to the vehicle's energy consumption and range. Therefore, it must be maximized over the entire operating range. Lastly, the motor must have a robust, durable design suitable for manufacturing and use in an EV [28]. Fig. 1.9 [29] depicts the two types of electric motors considered for tractive EV applications, which are IMs and permanent magnet synchronous motors (PMSM) [30]–[32]. Both motors are capable of providing a wide range of operating speeds while meeting tractive torque demands. Tractive PMSM and IM designs have similar stator structure. The major difference between the two designs is the rotor design and the materials required for rotor field production. Current EVs feature a number of variations of both IMs and PMSMs, however, they are largely dominated by variations of permanent magnet machines for their high-power density due to a smaller size and a higher efficiency when compared to induction machines [33]. The constant magnetic

11

field generated by the permanent magnets in the rotor hold several advantages over the induced magnetic field used by tractive IMs. By eliminating the need for slip to exist between rotor and stator field, PMSMs is able to decrease heat losses which raises the overall machine efficiency. In addition, since there is no need for currents to flow in the rotor to excite the machine, PMSMs have no losses due to electromagnetic losses in the rotor [34]. The downfall of PMSMs lies in its dependence on the rare earth metals such as neodymium and dysprosium used to produce strong magnets with high magnetic flux density favorable for EV applications. These materials are not readily available and require extensive processing before being incorporated into an EV. In addition to the already limited nature of these metals, according to the Institute of French International Relations, China is dominating the rare earth metal market, holding about 97% of the market share in 2010 [35]. This monopoly over the industry essentially lowers the availability of these materials even more to the remainder of the world. In turn, these high material and production costs means the price of PMSMs is also high, which inevitably trickles down to the consumer. In the hopes of producing electric motor that can compete with the performance of a PMSM for tractive applications while eliminating the dependence on limited and expensive materials, tractive IMs have peaked the interest of research institutes and industry leaders across the globe. Boasting high maximum speeds, relatively low current during no load operation and a robust, cost-efficient design, IMs are an ideal candidate for the electrification process by optimizing the motor to combat the major drawbacks of induction machines [36]–[38]. Due to a higher weight and volume, tractive IMs offer a lower torque density than rival PMSMs, as well as higher losses incurred in the rotor. A more detailed breakdown of the advantages and disadvantages associated with

PMSMs and IMs is seen in Table 1.2. To improve the drawbacks associated with the tractive IM, the torque density of the induction machine as well as the operating efficiency must be improved to be considered a competitive contender for EV applications. Many aspects of the electromagnetic design of tractive IMs, including the rotor and stator size and geometry, slot and bar shape and material and the winding configuration may be considered for optimization to ensure the best possible performance for EV applications.

TABLE 1.2

ADVANTAGES AND DISADVANTAGES OF IMs AND PMSMs [39], [40]

PMSM	Advantage	• Various configurations and adjustable performance • High torque and power density due to smaller size • High efficiency and power factor • Good heat dissipation due to no rotor losses
	Disadvantage	• High material cost due to rare earth elements • Control is difficult especially in flux weakening operation • Lower efficiencies at high speeds • High temperatures may lead to demagnetization on PMs • High back EMF in case of a fault
IM	Advantage	• Robust design resistance to ware and damage • Low production and material costs • Various configurations and adjustable performance • High peak torque, overload capability • Relatively simple control methods • Well established manufacturing process
	Disadvantage	• More demanding design process due to slightly lower performance • Lower efficiency due to rotor losses being present • Generally larger and therefore lower torque and power densities • Lower power factor • Rotor thermal management must be considered to dissipate heat

1.3. Literature Survey on Traction Induction Motor Design and Geometry

IMs for tractive applications must be specifically designed for high performance tractive applications. The same basic operating principles are exploited through new materials and manufacturing methods to ensure peak performance over a wide speed range. The design process of tractive IMs is analyzed to identify key design attributes crucial to determining the performance of IMs, the torque density, and the efficiency of IMs [39], [40]. These design aspects can then be optimized to offer optimal performance with respect to the desired target performance. Throughout the design process, key design factors must be constantly evaluated to provide an overall balanced design. Economic factors consider the cost of the overall product in order to be competitive within the market, which as a result of cost effective and available materials, IMs have the economic advantage. Material limitations always contribute to the constraints of the overall design and must be considered throughout the design process. Design specifications and safety regulations also play an important role in determining the limitations of a given design and depend on the application. The most crucial design factors with respect to tractive IM design is the electromagnetic design of the motor encompassing all electrical and magnetic components of the motor. It is these design factors that determine the preliminary constraints of the design problem specifying the desired power, speed, voltage, and frequency ratings required for EV applications. The design process begins with the desired performance and available electric loading of the application being used to define the size and power rating of the motor. The size and length of the rotor and stator are defined by sizing equations based on the desired performance and size constraints of the design application. The number of phases and the number of poles of the IM are assigned, tractive EV applications

typically feature 3 or 6 phases with 2, 4 or 8 poles [41]. Once the basic dimensions, performance and electric ratings are known, the design moves to the stator to develop the number of stator slots, the winding type and configuration and the selection of end winding connection summarized in the following section.

1.3.1. Stator Design and Geometry

The stator design process of IMs is similar to the design of permanent magnet synchronous machines and is therefore subject to similar improvements from a design perspective. The stator design begins with the selection of the stator slot shape. Commonly used stator slot shapes are the open and semi-closed stator slots, as seen in Fig. 1.9 [42], [43]. Open slots are typically designed with form wound winding bundles in mind to allow the ridged winding structures to be easily inserted into the slot and are ideal for applications with high power and voltage rating beyond the range used in EV. Therefore, the majority of EV stator slots are based on semi-closed slot designs as they offer smoother synchronous field production due to smaller air gaps and less harmonics. Semi closed stator slots must

(a)   (b)
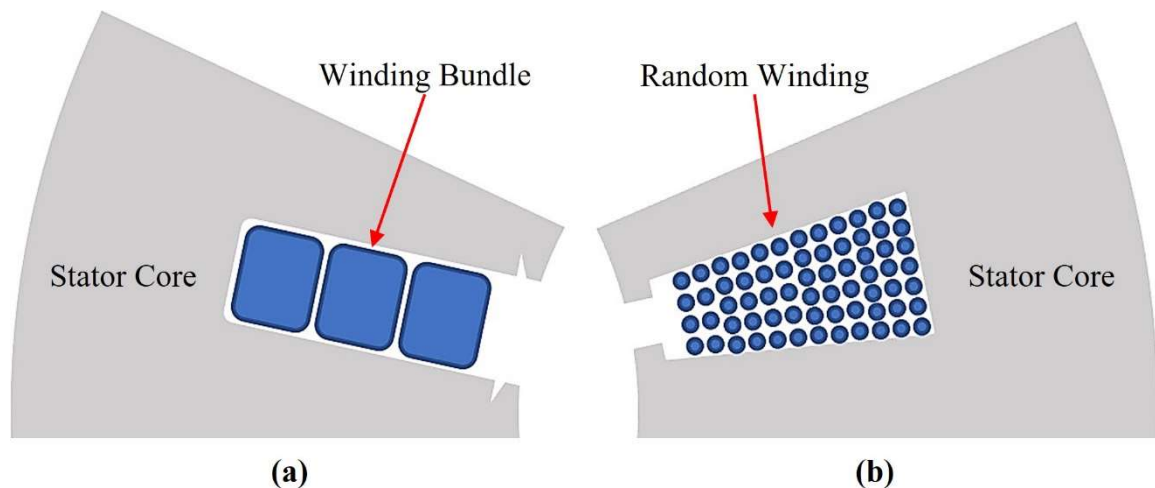
Fig. 1.9. Commonly used stator slot designs can be classified into two main slot types. (a) Depicts an open stator slot with winding bundles. (b) Depicts a semi-closed stator slot holding randomly wound coils.

be randomly wound due to the limited opening at the neck of each slot. The stator winding configuration is next to be decided and can take one of two commonly used winding types. Concentrated windings see stator windings wound about only 1 stator tooth best suited for applications that require short tractive IMs with large diameters due to shorter end windings. Concentrated windings are easier to manufacture and produce slightly higher torque than distributed windings however incur higher losses and higher harmonics as a result. Most EVs rely on some form of distributed winding configuration [44]–[46] where the winding of each phase is wound over two or more stator teeth, as seen in Fig. 1.10. Multiple winding layers sit in each slot, ensuring the smoothest possible synchronous magnetic field overlapping the next phase [47]–[49]. The number of stator slots spanned by the coil of each phase and the number of slots occupied by each phase must be carefully determined to ensure minimal harmonic losses leading to the higher efficiency of the designed motor. Once the winding configuration is determined and the coil span, slot pitch
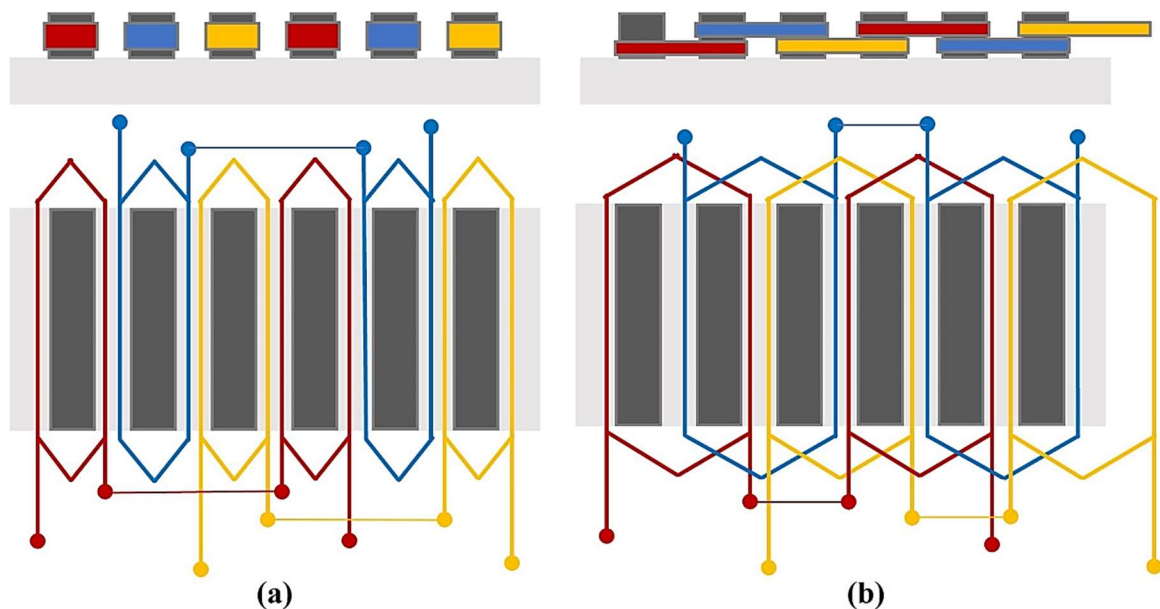
Fig. 1.10. The top and side view of an unrolled stator demonstrates the difference between three phase stator windings. (a) Concentric winding configuration features only one phase per stator tooth. (b) Distributed windings overlap phases.

and pole pitch are known, the coil type usually random fill or press fit, end winding connection of either Wye or Delta and conductor sizing based on standardized requirements are determined. The last step in stator design is selecting the number of stator slots which effects design factors such as the breakdown torque, torque ripple and starting currents of the tractive IM and therefore are chosen to be either 36,48 or 54 slots for tractive IM applications [50], [51]. This ensures an even magnetic field distribution and therefore higher efficiency operation while maintaining smooth output torque production. The preliminary stator design is complete, and the optimal rotor design to fit the stator.

1.3.2. Rotor Design and Geometry

The rotor structure of tractive induction machines is the most unique part about its design and therefore hold the potential to greatly improve the performance of the motor when optimally designed. Before investigating different rotor bar shapes, the first step in rotor bar design is to determine the number of rotor bars that complement the number of stator slots chosen during the stator design process. The selection of the correct number of rotor bars is crucial as certain slot combinations result in poor motor performance. To ensure a compatible slot combination is selected, the following cases outlined in Table 1.3 must be avoided. Slot combinations that satisfy case 1 in which S_1 is the number of stator slots and S_2 are the number of rotor bars, respectively, while P represents the number of poles, result in extremely high noise and engine vibration, which would greatly impact the safety and comfort level if the motor were used for tractive applications. If a slot combination satisfying case 2 is chosen, the resulting torque and speed curves may develop sharp cusps rendering the motor undesirable for use in EVs. Lastly, cogging issues resulting in stalling or the inability to start can occur with slot combinations that satisfy case 3, where

17

TABLE 1.3

STATOR SLOT AND ROTOR BAR COMBINATIONS TO AVOID [41], [52], [53]

Case	Stator Slot and Rotor Bar Combination
Case 1	$S_1 - S_2 = \begin{cases} \pm 2 \\ (P \pm 1) \\ (P \pm 2) \end{cases}$
Case 2	$S_1 - S_2 = \begin{cases} \pm P \\ (\pm 2P) \\ (\pm 5P) \end{cases}$
Case 3	$S_1 - S_2 = \begin{cases} 0 \\ \pm mP \end{cases}$

(m) is the number of phases. If a suitable number of rotor bars is selected and the slot combination does not satisfy any of the three cases, the most crucial and final step in tractive IM rotor design is determining the size and geometry of the rotor bar. From this analysis, the basic rotor bar in Fig. 1.11 demonstrates two distinct rotor bar regions that have a greater effect on specific output characteristics. Region 1 is considered to be the torque region of the rotor bar as it greatly affects the starting torque and torque density of the IM, while region 2 has a greater effect on the power density and efficiency of the IM. The National Electrical Manufacturers Association (NEMA) [54], [55]classifies four
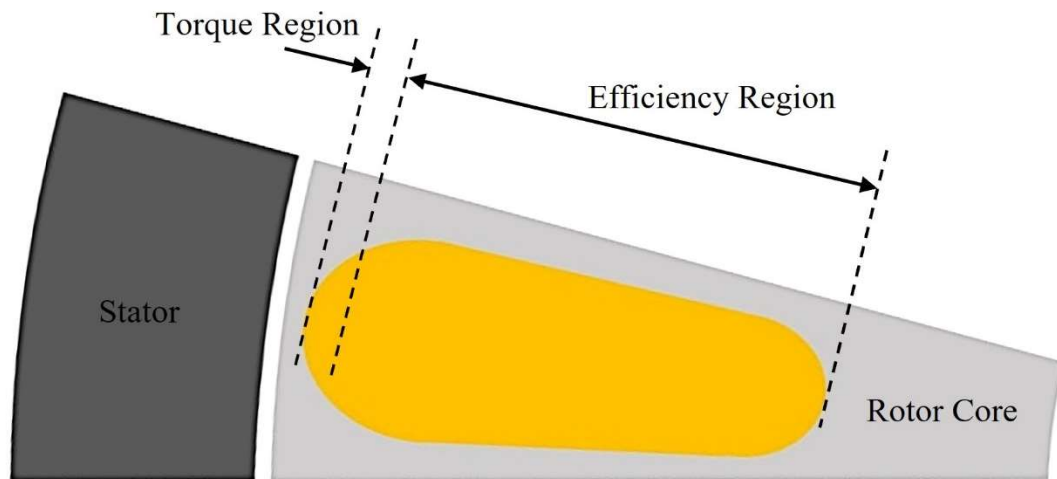
Fig. 1.11. Demonstrates the regions of the rotor bar and their respective affects on the performance characteristic the IM.

conventional rotor bars by geometry with respect to the performance characteristics of each to assist in the selection of a base rotor bar shape that can then be modified to suite the specific application. NEMA rotor bar classes A to D and their typical respective normalized torque-speed curves are depicted with respect the percentage of rated torque produced and the rotor slip in Fig. 1.12. Based on the torque-speed characteristics of each rotor bar class, and overview of the effect of different rotor bar geometries has on the overall motor performance with respect to all four NEMA classes is provided in Table 1.4. When designing rotor bars, the primary performance tradeoff is with respect to the resistance of the bar. Class A and B rotor bars are designed to have lower resistance as a result of a larger surface area leading to lower losses and higher efficiency while sacrificing starting torque. Class A and B rotor bars operate under low slip conditions resulting in higher torque, while
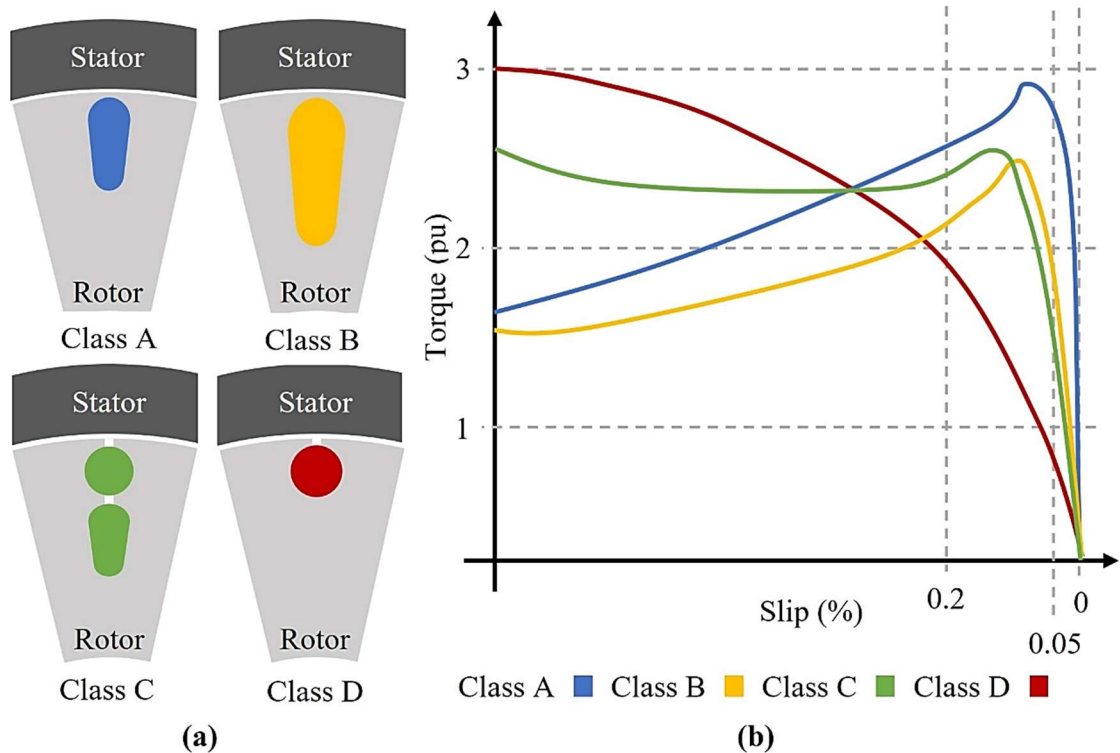
Fig. 1.12. NEMA classifications assist in the early IM design process. (a) Possible examples of the four NEMA rotor bar classifications are depicted. (b) The torque performance is displayed with respect to the slip for each rotor bar class.

19

TABLE 1.4

SUMMARY OF NEMA CLASS ROTOR BAR CHARACTERISTICS [55]–[57]

Operating Characteristics	Class A	Class B	Class C	Class D
Starting Torque	100% of Rated for large motors	100% to 150% of Rated for large motors	200% to 250% of Rated for large motors	250% to 300% of Rated
Starting Current	800% Rated	500% to 600% Rated	600% to 800% Rated	800% to 1200% Rated
Pullout Torque	200% to 300% of Rated	Greater than 200% of Rated	Slightly > class A	50% of Rated
Pullout Slip	<0.2	<0.2	Slightly > Class A	<1.0
Rated Slip	<0.05 slightly lower than class B	Between <0.05 and <0.03	<0.05 slightly higher than class B	Very High, typically <0.7 to <0.11

the bars are under less current, meaning more efficient operation when compared to class C or D rotor bar designs. Class D rotor bars depend on extremely high resistance, generating high starting torque, making them ideal for high inertial load scenarios however do not meet the efficiency standards required by tractive vehicle applications. Class A rotor bars may be used for tractive applications however, due to the low resistance-based design of class A designs, high inrush currents are experienced by the bars during starting often requiring specialized starting methods. Therefore, class B and C rotor bar designs are preferred for EV applications as they exploit current effects, including skin effect and skin depth to achieve a variable resistance with respect to operating condition. Class C rotor bar designs consist of two separate rotor bars entirely exploiting material properties to as to generate high starting torque as only the outer cage conducts during motor startup. This increased starting torque, however, causes a decrease in the efficiency of class D motors that is not justified in EVs leaving the ideal rotor bar geometry to be based on the class B

rotor bar design. Class B rotor bars offer the ideal balance between high torque performance while maintaining high operating efficiency due to lower losses [58]. Through the iterative modification and analysis of the effect of rotor bar dimensions and geometry on IM performance, the optimal rotor bar shape with respect to maximum operating torque and minimal losses.

1.3.3. Summary of the Effect of Geometry on Design Factors

Due to the computationally intensive nature of the design process, it is common to see the complete detailed design process be followed to develop a single motor. Different aspects of the design are then scaled to achieve the desired performance targets while upholding the same speed, flux density and current density as the detailed design. To summarize the effect size and geometry has on various design factors, Table 1.5 considers a motor in which all design aspects have been scaled up by the same factor. Although, in this case, the entire machine size increases, similar effects are observed in conductive and magnetic elements if only one specific design parameter were to be scaled. The effect changing size of various design aspects are directly or indirectly linked to the performance characteristics of the tractive IM and, therefore, must be carefully analyzed to strategically target the area with the greatest impact on optimization targets.

In conclusion, the design process of tractive IMs requires the simultaneous consideration of numerous design factors that have adverse effects on one another. Optimizing the IM design with respect to all considerable design factors would be impossible. Therefore, a balance with respect to several significant objectives depending on the application should instead be established. The rotor structure is unique to IMs, and a direct relationship between the rotor bar geometry and the output torque and losses of the

motor have been described. These output characteristics provide excellent objective targets for optimization. Optimal rotor bar design with respect to these targets will inevitably yield an IM with higher torque density and operating efficiency for EV applications.

TABLE 1.5

EFFECT OF SCALING ON DESIGN FACTORS

Design Factors	Effect of Increased Scaling by Factor k
Weight	Since all linear dimensions of the machine increase by a factor of k, the volume and therefore the weight will increase by k^3
Terminal Voltage	Increase in the core area and flux path by a factor of k^2 results in terminal voltage by k^2 if the number of turns is not changed
Load Current	The area of conducting materials increases by k^2, therefore the current carrying can be increased by k^2
Input Power	Since the terminal voltage and load current increase by a factor of k^2, respectively, the power input will increase by k^2
Resistance	Since the cross-sectional area of conducting materials will be increase by a factor of k^2, however, the length will increase by a factor of k, resulting in a reduction in resistance by a factor of k
Copper Loss	Since current increases by k^2 and the resistance goes down by a factor of k, the copper losses will increase by a factor of k^2
Iron Loss	Since flux density in iron components remains constant and the volume increases by a factor of k^3, the iron losses will increase by k^3
Power Output	Since the input power increase by a factor of k^4 while the losses increase by a factor of k^3, the output power increases at a rate slightly less than k^4.
Efficiency	Since the input power increased by a factor of k^4 and the output power by a factor slightly less than k^4 depending on the losses, the efficiency will be increase slightly with large increases in factor k.
Power Density	Since the input power increases by a factor of k^4 while the volume increases by a factor of k^3, the power density increases by factor k therefore explaining why larger machines eventually have higher efficiency.

1.4. Tractive Induction Motor Optimization

Tractive IM design is an extremely difficult and time-consuming process that involves countless multi-disciplinary design factors which have opposing effects on the output performance of the motor with respect to multiple conflicting desired performance requirements. Therefore, the design of a tractive IM for EV applications may vary greatly depending on the emphasis placed on each requirement by the designer. Due to the computationally heavy and time-consuming nature of tractive IM design, an initial design is generated in the effort to meet the desired performance targets required by the application [59]. The initial designs performance can only be verified after the complete design is created, often leading to a moderate design that fails to meet all requirements. Due to the large number of possible solutions, the initial design's performance is often less than the desired performance meaning the design must be further refined in order to provide optimal operating characteristics for tractive applications. This makes the design process iterative by nature, as the designer must sequentially adjust various aspects of the motors design to achieve the optimal design with respect to the design requirements. Once an initial design has been produced, this iterative process may be greatly assisted by an Optimization Algorithm (OA) [60], [61]. OAs are capable of solving for a set of design factors that minimizing or maximizing multiple desired performance objectives. An analytical model capable of determining the motor performance of all required objectives based on the selected design factor is coupled through OFs to the OA, as illustrated in Fig. 1.13 [62]. The run time and solution quality of the OA greatly depends on the speed and accuracy of the analytical model used and, therefore, must be carefully considered when selecting the type of model to be implemented.

23
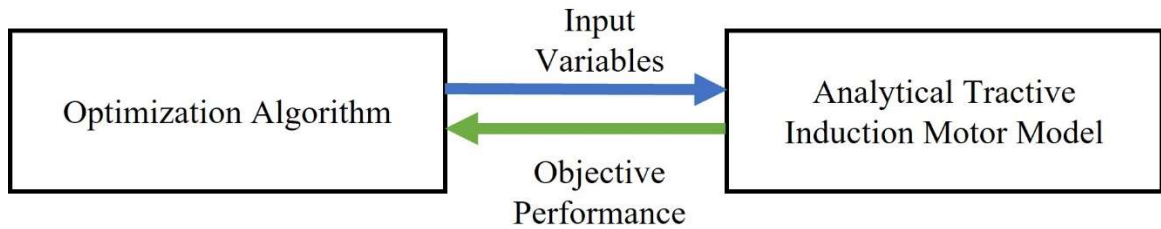
Fig. 1.13. This simple flow chart demonstrates the information that flows between the OA and the analytical model of the tractive IM.

1.4.1. Tractive Induction Motor Analytical Modeling for Optimization

Tractive IM analytical models for optimization purposes serve to simulate the output characteristics of the IM with respect to the set of chosen input variables allowing the OA to slightly altered and re-evaluate the motor performance under different combinations of input variables [63]–[65]. Depending on the algorithm, this iterative performance calculation takes place extremely often, and therefore the simulation time of the analytical model greatly affects the overall run time of the algorithm and furthermore the total number of possible solutions that can be discovered by the algorithm. The three most commonly used analytical models used for tractive IM optimization are electric equivalent circuit modeling (ECM), magnetic equivalent circuit modeling (MEC) and finite element analysis (FEA) based models compared in Table 1.6. FEA based modeling consists of breaking the entire motor assembly into a fine interconnected mesh of nodes at which all electromagnetic effects are considered. The smaller the mesh, the higher the mesh density becomes allowing the performance of the IM to be simulated at nearly any point that exists within the design. FEA produces extremely high-quality simulation results with respect to a wide range of possible performance objectives as well as being capable of simulating transient effects [66], [67]. The drawback of FEA is that due to its high computational nature, the simulation run times are extremely long and

24

TABLE 1.6

ADVANTAGES AND DISADVANTAGES OF ANALYTICAL MODELS [68]–[72]

FEA	**Advantage**	• Extremely high accuracy simulation capable of calculating the simultaneous effect of electromagnetic performance • Accurately models both magnetic and electrical losses under transient conditions • Multi-disciplinary effects may be considered
	Disadvantage	• Extremely high run times make FEA based OAs very computationally heavy and therefore slow • The search space, number of input variables, and objectives must be greatly reduced to accommodate for high run times • The model is not easily adjusted or modified
MEC	**Advantage**	• Less complicated computations leading to shorter run times • Focused on modeling magnetic components including rotor and stator cores • Accurately models magnetic leakage flux losses experienced by the IM • Easily modified to incorporate various effects and increase simulation accuracy
	Disadvantage	• Less accurate in determining performance characteristics than FEA simulation • Electrical loss effects are not closely considered • Must be modified to increase simulation accuracy for use in tractive motor optimization
ECM	**Advantage**	• Less complicated computations leading to shorter run times • Focused on modeling electrical motor components including rotor bars and stator windings • Accurately models electrical losses experienced by the IM • Capable of linking characteristic performance to rotor bar design • Easily modified to incorporate various effects and increase simulation accuracy
	Disadvantage	• Less accurate in determining performance characteristics than FEA simulation • Electric loss effects are not closely considered • Must be modified to increase simulation accuracy for use in tractive motor optimization

therefore, makes FEA an ideal tool when attempting to validate a specific design, however a poor choice for complex multi-objective optimization. The Magnetic equivalent circuit modeling is based on the magnetic effects that occur withing magnetizing elements of the IM. An equivalent circuit modeling the stator and rotor core with respect the flux path generated at any instant in time while the IM is under a magnetic loading. Although magnetic equivalent circuit modeling is less precise than FEA, the mathematical based model provides relatively high accuracy results while considering numerous magnetic effects that may affect the performance of the overall design [73]–[76]. The computation time associated with this method is much lower as a result of the motor geometry and effects being simplified into a simple circuit. As the name suggests, the electrical equivalent circuit is similar to the magnetic equivalent circuit. However, it considers the electrified components, specifically the stator windings and rotors of the tractive IM. Both magnetic and ECMs are favoured for optimization purposes as they are easily modified to fit the selected subject of the optimization and the desired performance targets, offer much faster run times and offer relatively accurate results [77]–[79]. The decision between the two is often made based on the function of the subject of the optimization and the nature of the output characteristics selected as targets by the designer.

1.4.2. Induction Motor Optimization Input Variables and Objective Targets

The proposed method focuses on optimizing the rotor bar geometry to offer 3% higher torque performance while minimizing the total losses of the base design by 3%. Therefore, an ECM is selected to analytically model and simulate the output torque and total losses of the tractive IM with respect to changes in the rotor bar geometry determined by the OA. Fig. 1.14 depicts the rotor bar dimensions are defined by three widths and four
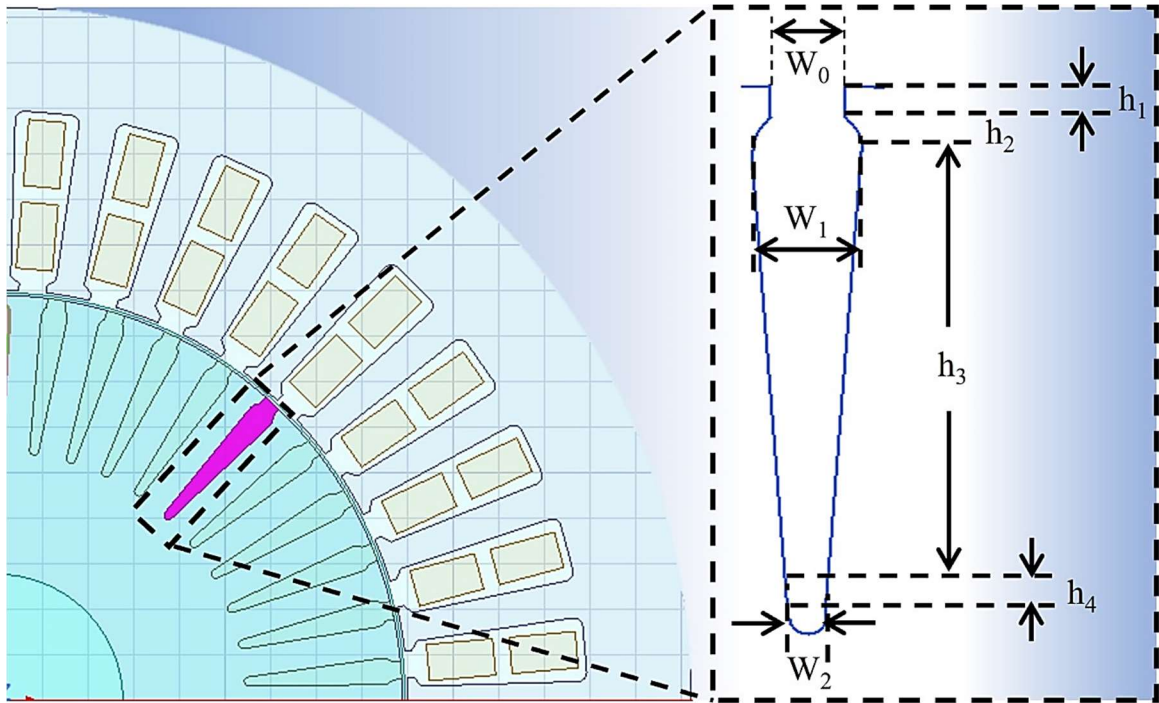
Fig. 1.14. The rotor bar is broken into 4 heights and 3 widths to be given to the OA as input variables.

heights seen in making up the seven input variables to the OA. The search space is defined

by the limits placed on each dimension of the rotor bar. To provide a reasonably large

search space to the OA, limits are set 75% above and below the base design. To ensure the

design is still structurally feasible and the tooth width is maintained, the search space is

also limited to 60% of the slot pitch. This ensures the tooth width is maintained while

allowing the largest possible search space to the algorithm. The other constraint placed on

the design is the maximum magnetic loading of 1.7T allowed in the rotor tooth to avoid

magnetic saturation and temperature rise [80]. The equivalent circuit model will determine

the output torque and total losses of the induction machine and relay the performance back

to the OA through OFs in an iterative loop until the optimal rotor bar geometry is found.

Table 1.7 summarizes the input variables, constraints, and output targets of the problem.

27

TABLE 1.7

OPTIMIZATION INPUT VARIABLES AND OBJECTIVE TARGETS

Subject and Number of Input Variables	The rotor bar is the subject of the optimization and is divided into 7 input variables to describe the geometry
Input Variable Bounds	The rotor bar geometry is given ±75% of the baseline rotor bar design to endure a large search space
Input Variable Constraints	The rotor bar geometry is constrained by occupying a maximum of 60% of the rotor slot pitch
Design Constraints	The maximum flux density in the rotor teeth may not exceed 1.7T
Performance Objective	The output torque and total losses are selected as the performance objectives of the optimization
Torque Objective Target	The target is to increase the output torque by 3%
Loss Objective Target	The target is to decrease the total losses by 3%

1.5. Research Motivations

To properly outline the objectives and the motivations of all aspects of the proposed method, multiple perspectives must be considered to determine the target and subject of the research presented. On the vehicle level, the entire EV must be considered and determines the desired performance of the entire system. The desired performance characteristics favorable for tractive application are investigated, and the components of EVs with the most influence on these characteristics are identified for further study. This has led to the electric motor becoming the focal point of EV performance resulting in a set of motor level objectives aimed at improving the major drawbacks of IMs for tractive applications. The rotor bar is unique to IMs and therefore is selected as the subject of the design optimization as they play a crucial role in determining the performance of the

desired targets. Since the design process of induction machines is complicated and time consuming, an algorithm is required to greatly reduce the time spent on designing the rotor bar and greatly improve the quality of the solution produced. To determine the modifications to the OA required to accommodate the design problem, algorithm level objectives and motivations are defined to address the challenges associated with rotor bar optimization of tractive induction machines.

1.5.1. Vehicle Level Motivations

As a relatively new technology, EVs offer a promising emissions free solution to personal transportation, which has led to the recent increase in the public interest and garnered the support of international governments and industries. To satisfy consumer demand while competing with traditional internal combustion vehicles, crucial performance characteristics of EVs, including range and torque density, must be improved. Although there are numerous factors that determine the performance capabilities of an EV, the efficiency and torque density of the electric motor selected are essential. Through increased research and development into the electromagnetic design of electric motors, the desired performance characteristics of EVs must be enhanced.

1.5.2. Motor Level Motivations

With their robust structure and cost-effective materials and manufacturing process, IMs offer high peak torque and overload capabilities, making them an ideal choice for tractive applications. Since IMs offer slightly lower efficiency due to the presence of losses in the rotor and lower torque densities as a result of a larger size when compared to more

commonly used permanent magnet motors, the design of the rotor bar may be optimized to reduce the total losses and increase the IMs torque capabilities.

1.5.3. Algorithm Level Motivations

The rotor bar optimization of a tractive IM poses a complex multi-variable optimization problem. In order to generate a high-quality solution under a maximum algorithm run time of 300 seconds, an OA must be developed that is capable of non-dominated multi-objective optimization considering the dynamic nature of the application. Conventional optimization strategies must be modified to reduce the computation time, improve the solution quality, and ensure a balanced solution that satisfies both optimization objectives while avoiding stalling, function bias and premature convergence.

1.6. Research Objectives

The global objective of the proposed method is to develop a robust, novel multi-objective GA capable of optimizing the rotor bar geometry of a tractive IM considering the dynamic operation for use in commercially available EVs, leading to improvements in the overall performance of future EVs. The vehicle level objectives are to increase the range and torque density of commercial EVs through design optimization of a tractive electric motor raising the efficiency by 1% and torque density by 3%. This is achieved through an optimized rotor bar geometry resulting in the motor level objectives of 3% higher torque and 3% lower losses. To determine the optimal rotor bar geometry, the algorithm level objective is to develop a non-dominated, robust GA capable of optimizing the rotor bar geometry for higher torque and lower losses over the entire operating range while maintaining low run times and high solution quality.

1.7. Research Contribution and Deliverables

To satisfy the algorithm level objectives, a novel, non-dominated adaptive restart GA capable of optimizing the rotor bar geometry for higher torque and lower total losses with respect to driving cycle based dynamic operating points is proposed and implemented to achieve the motor level objectives by proposing an optimal rotor bar design which produces higher torque and lower losses over the entire operating range. When used in tractive EV application, the proposed optimal rotor bar offers a cost effective, durable tractive IM with 3% higher torque density and 1% higher efficiency leading to improved EV boasting longer ranges and higher power density, fulfilling vehicle level objectives.

1.8. Organization of Thesis

This thesis proposes a novel method of geometric rotor bar optimization to increase the torque density and efficiency of a tractive IM for tractive applications while considering dynamic operating conditions through the implementation of a non-dominated adaptive restart GA. The major sections of this thesis are as follows:

1) Chapter 1 provides an overview of EVs, tractive electric machines and the use of OAs in induction machine optimization, demonstrating the motivations, challenges and objectives associated with the proposed method from a vehicle level to the motor level and the incorporation of the algorithm level.

2) The baseline tractive IM considered for optimization is introduced in chapter 2, outlining the base rotor bar shape and the baseline torque and loss performance is determined. The modified permeance based equivalent circuit model used in the proposed method is described and validated, and the optimization algorithm to be used is selected.

31

3) A novel OF modeling strategy is proposed and tested in chapter 3 to ensure all function bias is eliminated between the torque and loss objectives during optimization. The elimination of function bias ensures a balanced optimal solution across all objectives.

4) The development of a robust adaptive restart GA is detailed in chapter 4 to improve the algorithms ability to resist stalling and early convergence, increase the final solution quality and reduce the overall run time through intelligent search space reduction.

5) Chapter 5 incorporates the effects of various dynamic operating conditions required by tractive IMs into the optimization process. These dynamic operating points are determined over the WLTP -3 drive cycle and reduced using the energy center of gravity method ensuring operating conditions of the highest energy consumption are represented.

6) Chapter 6 analyzes the optimized rotor bar shape and performance against the baseline motor and validates using FEA. The algorithm performance of the novel non-dominated adaptive restart GA is analyzed and discussed.

7) Chapter 7 summarizes the results generated through the proposed method and identifies the future scope of the proposed research and developed method in the area of IMs and algorithm-based IM optimization.

CHAPTER 2 Permeance Based Equivalent Circuit Modeling of Induction Motors and Optimization Algorithm Selection

2.1. Baseline Tractive Electric Motors

The tractive IM considered as the baseline motor is a small scale 11 kW IM designed as a prototype for tractive applications. The baseline IM offers 36.34 Nm of continuous torque under rated conditions requiring a 400 V DC supply for SUV style tractive applications seen in Fig. 2.1(a), and a cross section of the rotor and stator structure is depicted in Fig. 2.1(b). The motor was selected as it offers output characteristics designed for tractive applications while offering small-scale size allowing it to be easily tested at various operating points under laboratory conditions. Table 2.1 details the physical parameters and rated performance. Therefore, if the performance of the baseline IM can be improved through rotor bar optimization, the prototype may be scaled up to meet the design ratings

(a)   (b)
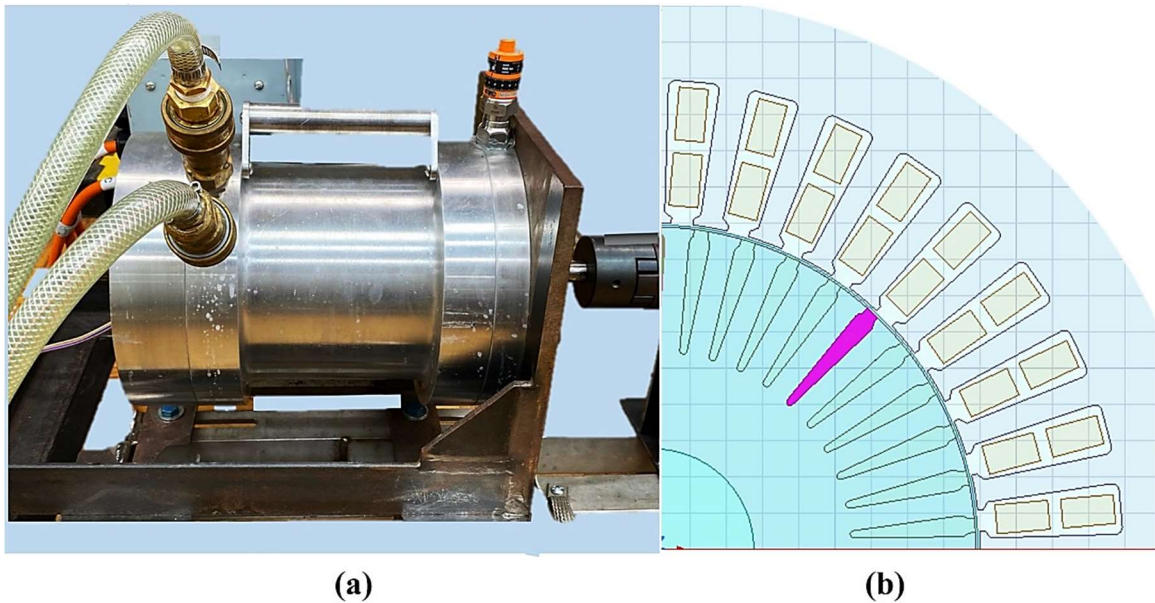
Fig. 2.1. The scaled down prototype tractive IM used as the baseline IM to be optimized. (a) Depicts the baseline prototype tractive IM used for experimental validation. (b) The rotor and stator structure of the baseline IM.

33

TABLE 2.1

BASELINE TRACTIVE INDUCTION MOTOR PARAMETERS AND RATINGS

Physical Parameters		Rated Characteristics	
Parameter	Baseline	Characteristic	Baseline
Stator Inner Diameter	89.4 mm	Rated DC Voltage	396 V
Rotor Outer Diameter	88.9 mm	Peak Line to Line Voltage	227.9 V
Air Gap Length	0.5 mm	Peak Input Current	480 A
Motor Weight	21.5 kg	Output Power	11 kW
Core Material	Steel	Rated Torque	36 Nm
Winding Material	Copper	Rated Speed	3000 rpm

of commercially available tractile IMs. The baseline motor allows for experimental model validation at various operating points ensuring high solution quality and drive-cycle based testing to identify operating regions requiring further optimization. The rotor bar geometry with respect to the seven rotor bar dimensions of the baseline tractive IM defined by the input variables of the OA are depicted in Fig. 2.2.
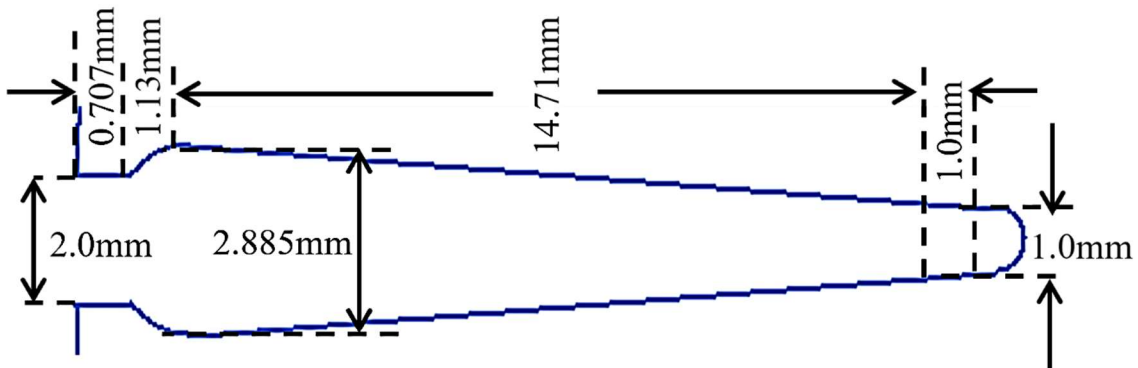
Fig. 2.2. The rotor bar dimensions of the baseline tractive IM with respect to the seven input variables defined for the optimization problem.

2.2. Permeance Base Equivalent Circuit Modeling of Induction Motors

To accurately model the baseline tractive IM, a modified electrical equivalent circuit is selected as the analytical model for the OA. The permeance based equivalent circuit model [81] allows for the consideration of magnetic flux leakage effects and electrical non-linearities caused by alternating supply currents required in tractive applications [82]–[84]. Since magnetic leakage effects, including slot, zig-zag, and tooth top leakage, greatly depend on the rotor and stator geometry, they must be closely considered during optimization to ensure the magnetic characteristics of a particular rotor bar design are accurately modeled. Non-linearities in electrical equivalent circuit parameters are the result of alternating current direction and magnitude and are also influenced by the rotor and stator slot and bar geometry. Through the incorporation of slotting and skin effects in all current carrying elements [85], the simulation accuracy of the permeance based equivalent circuit model provides the OA a better opportunity to generate a higher quality solution. The permeance based equivalent circuit is depicted in Fig. 2.3, can evaluate the output torque, total loss and operating efficiency of the baseline tractive IM performance accuratly at a fraction of the computational complexity of FEA simulation. The benefit of incorporating the specific permeance of baseline motor is that it allows for the geometry
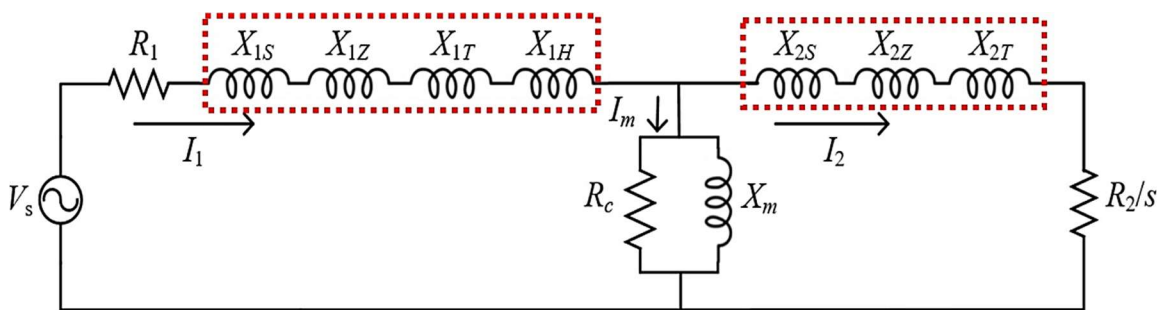
Fig. 2.3. Depicts the permeance based equivalent circuit model with stator, rotor and magnetization branches incorporating non-linearities and leakage effects.

35

to be directly related to electromagnetic equivalent parameters. The reactance modeling of the rotor bar, along with the incorporation of leakage flux effects are defined for the rotor in the following section. The simultaneous integration of non-linearities into the rotor resistance modeling is described. The same effects are applied to the stator in the same manner leading to the calculation of the output torque, total losses and operating efficiency of the baseline tractive IM.

2.2.1. Incorporation of Leakage Effects

To determine a direct relation between the rotor bar geometry and the reactance of the rotor, a permanence-based model is implemented. Through the incorporation of magnetic flux leakage effects, including rotor slot, zigzag, and tooth top leakage flux, the accuracy of the analytical model and, therefore, the solution quality produced by the GA will improve. Rotor slot leakage permeance λ_r can be calculated using (1) and represents the flux loss in the slot to the surrounding core not contributing to the useful flux at the top of the rotor bar near the air gap. Dependent on the cross-sectional area SA_b and shape of the rotor bar determined by the rotor bar dimensions.

$$\lambda_r = \frac{h_r}{3W_1}\left[1 - \frac{\pi W_1^2}{8a_b}\right]^2 + 0.66 - \frac{h_0}{2W_1} + \frac{h_0^2}{W_0} \tag{1}$$

Zigzag leakage effects are the result of flux interaction between the rotor and stator teeth and therefore depends on the stator and rotor tooth top width w_{ts} and w_{tr}. Since the tooth top width of the rotor teeth are directly dependent on the rotor bar dimensions, Zigzag leakage permeance λ_z is calculated using (2) incorporating the tooth widths of both the stator and rotor and y_s and y_r representing the stator and rotor slot pitch.

$$\lambda_z = \frac{\mu_0 \times W_{ts} \times W_{tr} \times (W_{ts}^2 \times W_{tr}^2)}{12 \times l_{eg} \times y_s^2 \times y_r} \tag{2}$$

Rotor tooth top leakage permeance λ_t is a result of flux loss in the rotor teeth, which depends on air gap permeability μ_0, the rotor slot pitch y_r and the effective air gap length l_{eg} is modeled using (3).

$$\lambda_t = \frac{\mu_0 \times l_{eg}}{y_r} \tag{3}$$

The equivalent circuit reactance components of the rotor are calculated using (4) in which n represents the respective subscripts for the slot X_r, zigzag X_z and tooth-top X_t reactances. The operating synchronous frequency is given by f, T_{ph} is the number of turns per phase in the stator, L is the axial stack, p is the number of poles and Q is the number of poles per phase.

$$X_n = 8\pi \times f \times T_{ph}^2 \times L \times \left(\frac{\lambda_n}{p \times Q}\right) \tag{4}$$

A similar technique is applied to incorporate the three before mentioned leakage effects in stator slots, as well as an additional overhang leakage component due to overhanging stator turns. The summation of these leakage effects determines the total rotor reactance X_2 of the baseline tractive IM in (5).

$$X_2 = X_r + X_t + X_z \tag{5}$$

2.2.2. Incorporation of Non-Linearities

The equivalent DC resistance of the rotor bar is calculated using (6) and has a direct relation to rotor bar geometry through the cross-sectional area SA_b and axial length of the rotor bar L_b. The stator winding factor k_{ws}, the number of phases m, the number of rotor bars S_r also contribute to the equivalent DC resistance. Lastly, D_e and SA_e are the diameter and cross-sectional area of the end ring and ρ_{Al} is the resistivity of the material.

$$R_{r\,dc} = \rho_{Al} \times m \times T_{ph}^2 \times p \times k_{ws}^2 \left[\frac{L_b}{S_r \times SA_b} + \frac{2\pi \times D_e}{p^2 \times SA_e}\right] \tag{6}$$

37

To incorporate the effects of alternating supply currents, skin and slotting effects must be incorporated to further improve the accuracy of the permeance based equivalent circuit model. Skin effect describes the tendency of more current to flowing near the outer edge of a conductor, essentially changing the resistance of the bar as a function of its height. Skin effect is therefore incorporated through dividing the rotor bar geometry into sub-section and determining the resistance of each sub section iteratively based on the ratio between the conductor height and the penetration depth ξ in equation (7).

$$R_{2 \text{ ac}} = \left(\xi \frac{(\sin 2\xi + \sin 2\xi)}{(\cosh 2\xi - \cos 2\xi)}\right) \times R_{r \text{ dc}} \tag{7}$$

Caused by the slight change in air gap length due to rotor bar openings, the slotting effect is incorporated through the use of the Carter coefficient K_c calculated in (8). The Carter coefficient changes the effective air gap as a function $f(\alpha)$ dependent on α representing the ratio between the tooth widths and the air gap length l_g. The Carters coefficient is then multiplied by the air gap to solve for the effective air gap length l_{eg}

$$K_c = \frac{W_{ts} + W_{tr}}{W_{tr} + W_{ts} - l_g f(\alpha)} \tag{8}$$

The effects of these non-linearities are incorporated in the stator, all equivalent parameters incorporate the slot, tooth top, and zigzag leakage effects, as well as skin and slotting effect allowing the reactance and resistance of the rotor, stator and magnetization branch to be calculated. The output torque, T_{out}, is determined by (9) and depends on the slip s, the calculated rotor and stator reactance and resistance, synchronous speed ω_s, and the air gap voltage V_g.

$$T_{out} = \frac{3V_g^2 \left(R_2/s\right)}{\omega_s \left(R_1 + R_2/s\right)^2 + (X_s + X_2)^2} \tag{9}$$

The total losses P_{loss} of the baseline, IM are found through the summation of the rotor core

losses $P_{r\,core}$, rotor copper loss, $P_{r\,Cu}$ and stator core $P_{s\,core}$ and copper $P_{s\,Cu}$ seen in (10).

$$P_{loss} = P_{r\,Cu} + P_{r\,core} + P_{s\,Cu} + P_{s\,core} \tag{10}$$

The resultant output torque and total losses of each respective rotor bar design

generated by the GA is then fed to the algorithm through the OFs to determine the overall

fitness of the particular rotor bar design. The respective input and output powers of the

baseline tractive IM P_{out} and P_{in} are used to determine the efficiency η in (11), which is

an important characteristic with respect to the vehicle level objectives proposed.

$$\eta = \frac{P_{out}}{P_{in}} \times 100 \tag{11}$$

The permeance based equivalent circuit model must now be validated to ensure

simulation accuracy against FEA of the baseline tractive IM, ensuring a high solution

quality is produced by the GA.

2.2.3. Permeance Based Model Validation

To validate the accuracy of the permeance based equivalent circuit model (PECM)

to be used as the analytical model for optimization, the output torque, total losses and

efficiency produced by the PECM at various operating points are compared to FEA and

experimental test results. Operating points at speeds above and below the base speed of

3000 rpm were selected to ensure the baseline motor is analyzed in both the constant torque

and constant power operating regions. The experimental setup used to test the baseline

motor is shown in Fig. 2.4 in which the baseline motor is depicted as the DUT. The baseline

IM is coupled through a variable gear box to a low speed, torque-controlled DYNO used

to apply the required load torque at each test point. The use of a variable gearbox is

necessary because the baseline IM has a high speed and low torque rating, while the DYNO

39
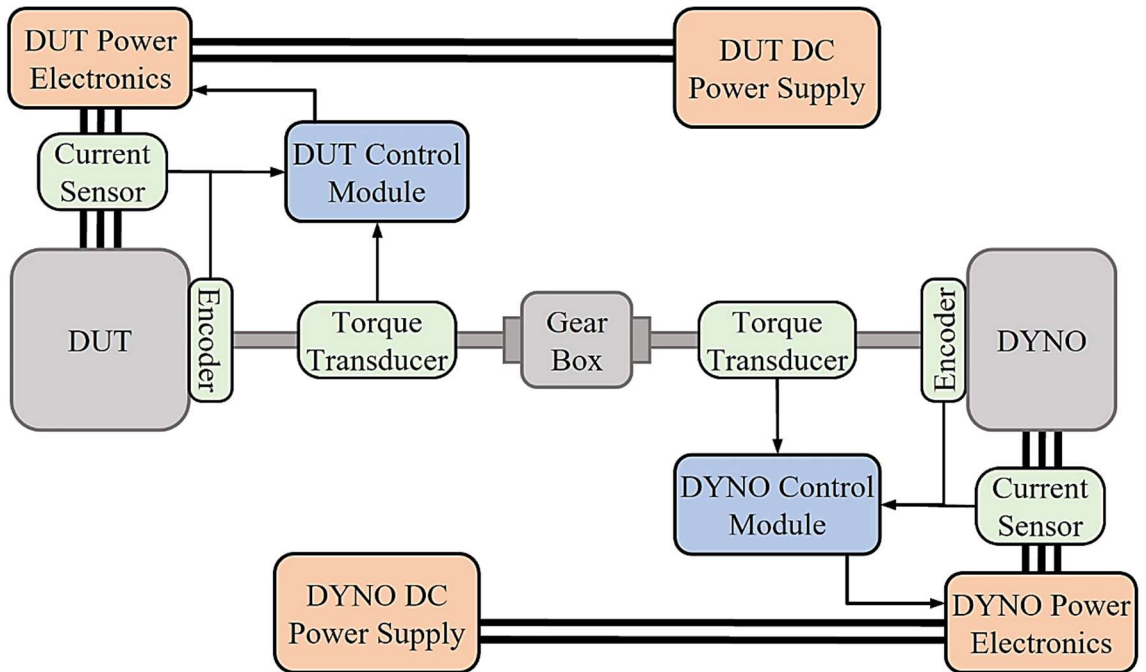
Fig. 2.4. Depicts the experimental setup used to test the 11 kW baseline IM at various operating points in both the constant torque and constant power region for permeance based model validation.

has a low speed and low torque rating. Therefore, variable gear box is implemented to

allow a wide range of operating points to be tested. The torque, speed and input power of

the baseline IM are measured through sensors and used to validate the results produced by

the PECM. The measured torque can be directly compared, while the total losses and

efficiency can be calculated through measured parameters.

The results collected experimentally from the baseline IM and through FEA

simulation are compared in Fig. 2.5 with respect to the output torque, total losses and

operating efficiency at 5 operating points. The PECM was able to predict the output torque

and total losses with an average error of 5.2% and 6.8%, respectively, while predicting the

operating efficiency with an average error of 1.8% of the measured performance. The close

correlation of the PECM output characteristics and the results produced through FEA and

experimental testing in both the constant torque and constant power regions are within an
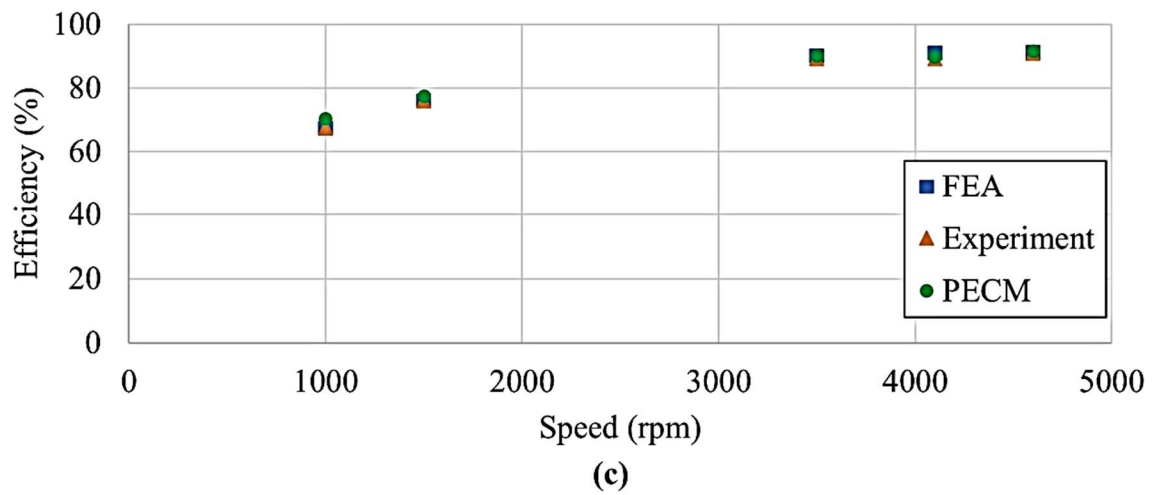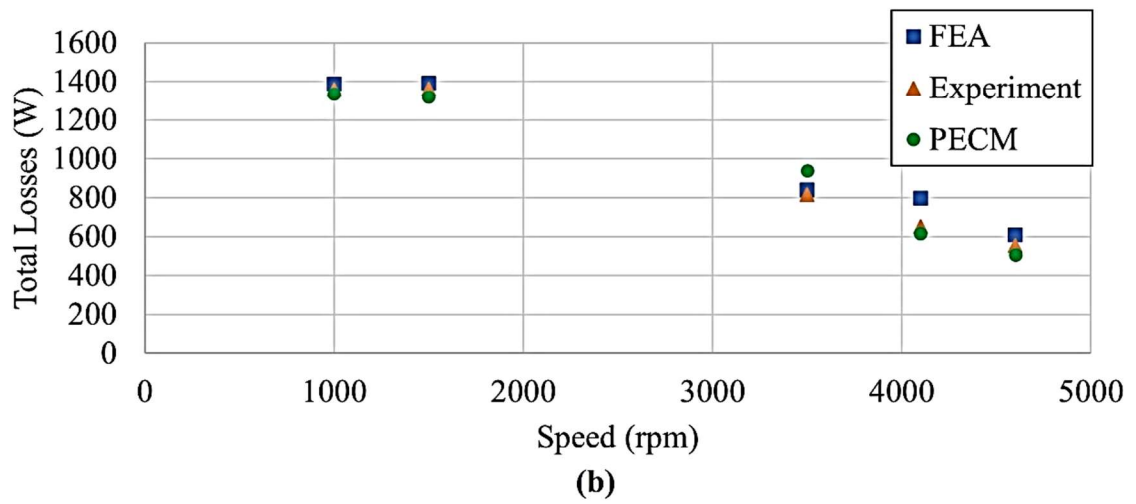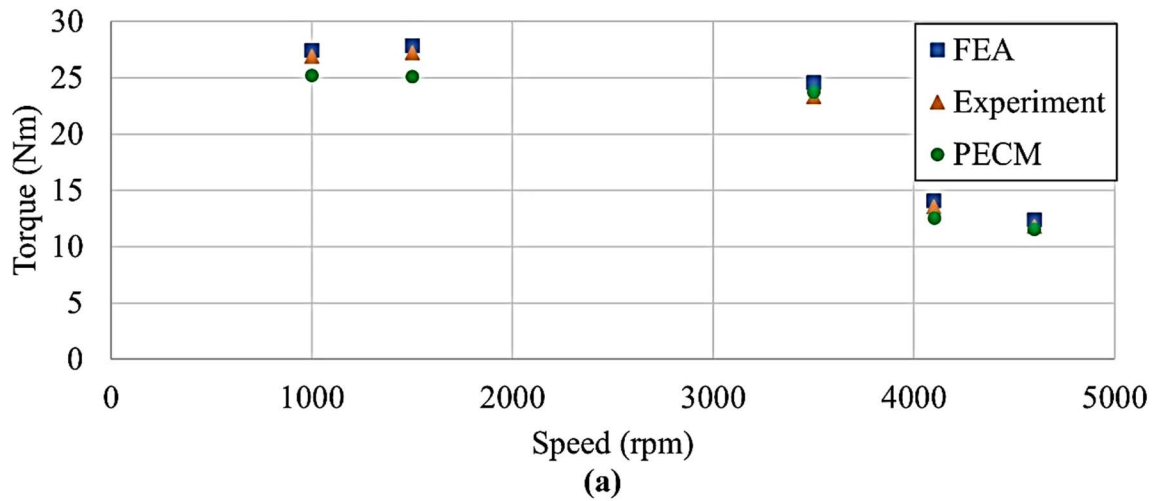
Fig. 2.5. Torque, total losses and operating efficiency validation on 5 test points. (a) Depicts the torque relationship. (b) Validates the total losses produced by the PECM. (c) Depicts the efficiency validation.

acceptable error margin to ensure the OA produces a high-quality solution while maintaining low run times. With the PECM selected as the analytical model, linking the rotor bar shape to the desired objective targets, a multi-objective OA must now be selected to optimize the rotor bar geometry of the baseline IM for higher torque and lower losses.

2.3. Optimization Algorithms

In its simplest form, optimization is finding the input variable or set of input variables that result in the minimum or maximum value of one or more selected OFs. In many cases, the OF may be subject to constraints limiting the search space and increasing the complexity of the algorithm [86]–[88]. The larger the search space of an algorithm, the better the chances of finding a high-quality optimal solution. A constrained optimization problem can be converted to an unconstrained optimization problem through various constraint handling methods, such as the addition of a penalty function [89]–[93]. The reason unconstrained optimization problems are preferred lies in the simple fact that without constraints, the algorithm is able to search without limitation, offering the highest probability of finding the optimal solution. Simple optimization problems with little computation and known constraints can be solved through parametric search (PS) based algorithms [61], [94], [95] while complex multi-variable applications of OAs such as optimizing the geometry of a tractive IM requires the aid of higher-level algorithms. Genetic or Particle Swarm based algorithms draw their inspiration from biological and social mechanisms and are well suited to handle complex optimization problems due to the application flexible stochastic optimization methods [36], [96]–[102]. The following section will highlight three types of OAs and present a case study examining the single objective performance when applied to minimize an optimization test function with respect

42

to two input variables. The results of this case study will ultimately determine which OA is best suited for geometric optimization of the rotor bar for improved output torque and reduced total losses for tractive IM applications.

2.3.1. Parametric Search Based Optimization

The premise of a PS algorithm is essentially a grid-based sweep across the entire search space, making PS algorithms among the simplest OAs to implement. Through iteratively reducing the search space while centering it at the best-known point from the previous iteration, the PS algorithm is able to solve simple multi-variable and multi-objective with increasing accuracy the more iterations are performed. The main limitation of PS algorithms is the algorithm run time. Since the number of calculations performed by the algorithm depends on the grid resolution, even at low resolution, the number of computations is much higher than evolution or swarm-based algorithms. In addition to high run times, PS algorithms are prone to premature convergence to a local minimum as a result of low search grid resolution. The conventional flow of a PS algorithm is demonstrated in figure 2.6. [103], [104]. The initialization step sets the global bounds of the search space with respect to each input variable, the reduction factor determining the percentage reduction in search bounds and the grid resolution, which determines how many samples will be taken between the search bounds of each iteration. During the initial iteration, the search bounds are set to the global bounds allowing a course sweep of the entire search space. Each iteration, the search bounds are reduced and centered about the best-known point using (12) and (13).

$$L_{ub_j}(iter) = x_{min_j}(iter-1) + (1-K_{red}) \times \left| L_{ub_j}(iter-1) - x_{min_j}(iter-1) \right| \quad (12)$$

43

$$L_{lb_j}(iter) = x_{min_j}(iter - 1) - (1 - K_{red}) \times \left| L_{lb_j}(iter - 1) - x_{min_j}(iter - 1) \right| \quad (13)$$

From the search bounds and the resolution, (14) determines the step size at each iteration.

$$step_j(iter) = \frac{L_{ub_j}(iter) - L_{lb_j}(iter)}{res(iter)} \quad (14)$$

```
┌─────────────────────────┐
│  Initialize Search       │
│  Parameters & Global     │
│  Bounds                  │
└─────────────────────────┘
            │
            ▼
┌─────────────────────────┐
│ Establish Local Bounds   │◄──────────┐
│ & Step Size              │           │
└─────────────────────────┘           │
            │                          │
            ▼                          │
┌─────────────────────────┐   ┌──────────────┐
│ Grid Search of Objective │   │ Iteration + 1│
│ Determines Output Array  │   └──────────────┘
└─────────────────────────┘           ▲
            │                          │
            ▼                          │
┌─────────────────────────┐           │
│ Identify Minimum Fitness │           │
│ & Percent Change in      │           │
│ Fitness                  │           │
└─────────────────────────┘           │
            │                          │
            ▼            No            │
       ◇ Check for ◇ ─────────────────┘
       ◇ Convergence ◇
            │ Yes
            ▼
┌─────────────────────────┐
│ Display the Global       │
│ Minimum Solution         │
└─────────────────────────┘
```
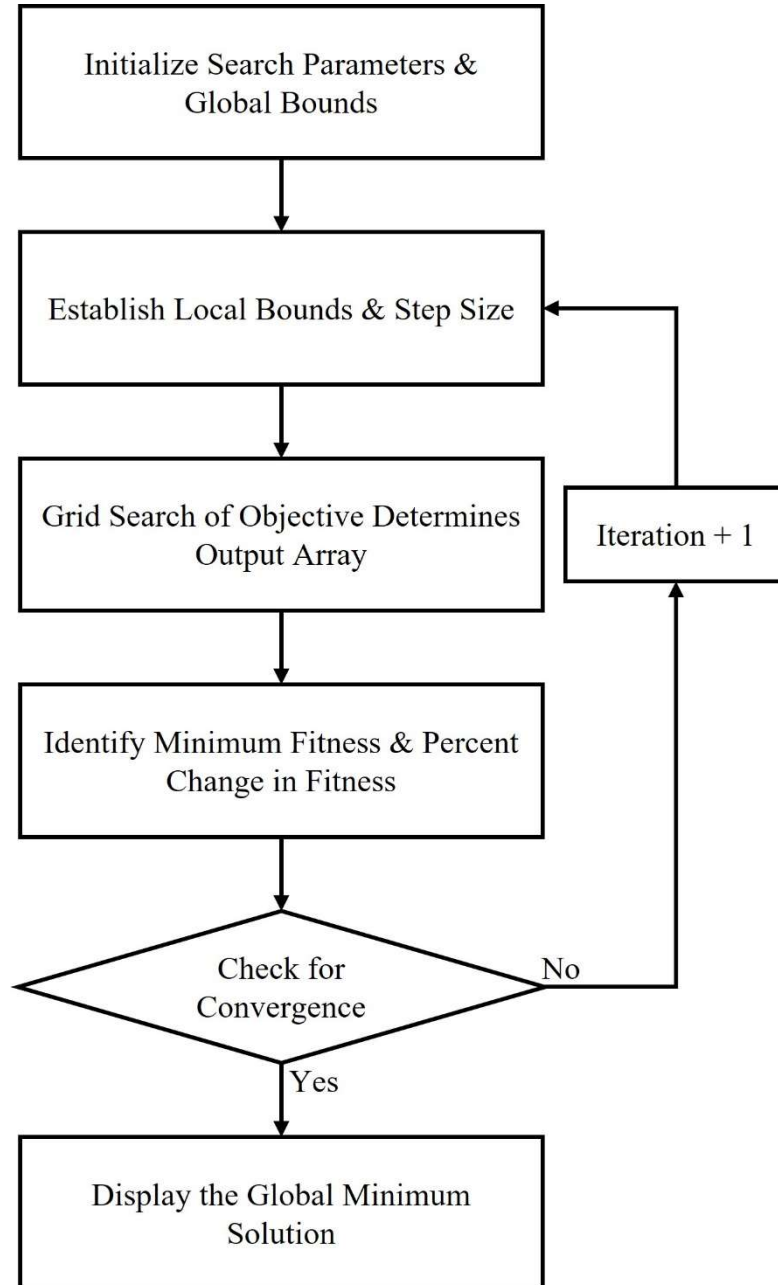
Fig. 2.6. The flow chart demonstrates the iterative limit reduction and evaluation performed by conventional parametric search-based OAs.

As the search space is reduced each iteration, the step size becomes smaller allowing for fine tuning of the optimal result. The PS algorithm then generates an array of possible combinations of input variables evenly distributed over the search space. The OFs are evaluated on all points generating an output array of corresponding OF scores. The algorithm then sorts the output array identifying the minimum OF score and thereby the current optimal combination of input variables. The percentage change in OF score of the current optimal solution is compared to the function tolerance to determine if the stopping criteria of the algorithm have been met. When the algorithm converges, or the maximum number of iterations has been met, the algorithm displays the optimal combination of input variables resulting in the minimum OF score.

2.3.2. Particle Swarm Optimization

Based on the principles of swarm intelligence, particle swarm optimization (PSO) is an iterative process in which a swarm of particles moves about the defined global search space in search of the global minimum solution. Swarm intelligence states that although individuals of the swarm on their own would not be able to solve the optimization problem, however, as a collective, through observing the successes and failures of other individuals within the entire swarm and learning from previous experience, a high-quality optimal solution to complex multi-objective optimization problems can be iteratively solved [105], [106]. Each particle within the swarm represents a combination of input variables which represents the position of the current particle within the global search space. Each particle also has an associated velocity denoting how quickly and in which direction the individual particle is moving through the search space. Each iteration of the particle swarm algorithm, the position and velocity of every particle are updated, and its next step is determined

considering the current velocity of the individual, the individual's position with respect to its personal best-known position and the individuals position with respect to the global best known position by all particles of the swarm [107], [108]. The velocity update of a particle is described in (15) and used to determine particle position in the next iteration using (16).

$$v_{ij}(it + 1) = cv_{ij}(it) + r_1 c_1 \left(x_{\min_{ij}}(it) - x_{ij}(it)\right) + r_2 c_2 \left(G_{\min_j}(it) - x_{ij}(it)\right) \quad (15)$$

$$x_{ij}(it + 1) = x_{ij}(it) + v_{ij}(it) \quad (16)$$

The position of the particle, i, is denoted by x_{ij} at a particular iteration, it, which represents a possible combination of j input variables. The current velocity of an individual particle is denoted by v_{ij} and represents the speed and direction in which the particle is moving through the search space. The fitness of each particle is evaluated every iteration, as seen in Fig. 2.7 where the global best particle position G_{min_j} is determined along with the best-known position of the particular particle $x_{min_{ij}}$. Acceleration coefficients c, c_1 and c_2 allow the effect of each term in the velocity update to be manipulated and r_1 and r_2 represent randomly generated scalar coefficients between 0 and 1. An arbitrary particle, its associated velocity and the resultant velocity vectors between the particle and the personal
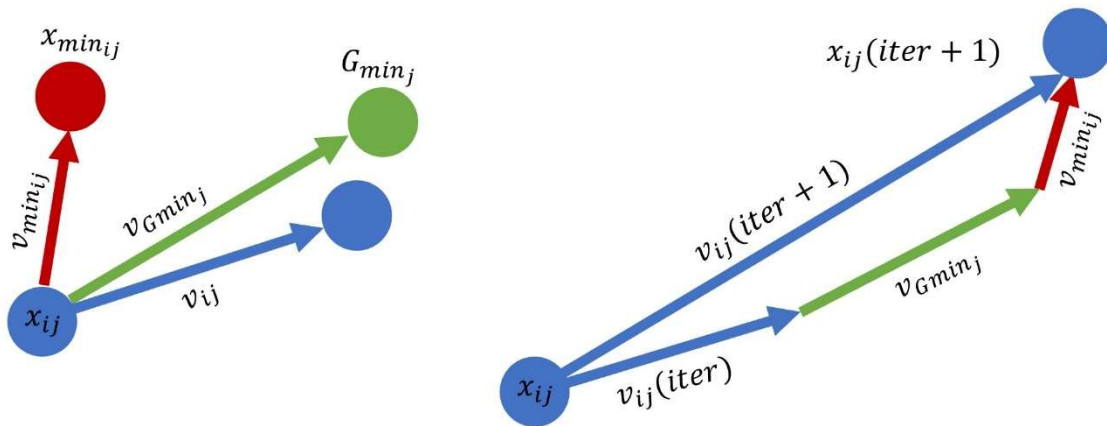
Fig. 2.7. Each particle evaluates its current position with respect to the three vectors shown and uses the resultant vector to determine its position and velocity during the next iteration.

and global best solution. The three resultant velocity vectors are added together, and the velocity and particle position of the next generation are found. The swarm size, function tolerance, maximum iterations, global limits and other algorithm parameters are set during the initialization stage, as seen in Fig. 2.8. The initial particle position and velocity are generated randomly across the search space to generate the swarm, which is then evaluated by the OFs of the algorithm. Particles are ranked based on fitness, and the global best particle position is determined to be the best-known solution of the current iteration. If the maximum number of iterations or stall iterations has been reached or the change in fitness falls below the set function tolerance, the particle swarm algorithm converges, and the global best solution is displayed. If none of these cases are met, the algorithm iterates and generates the future velocity and position of the future swarm. This iterative process ensures that particles rapidly congregate towards the global best-known solution as all velocity vectors graduality begin to mimic the direction of other particles within the swarm. Through learning from other particles, the collective swarm gains intelligence exponentially faster than an individual particle could on its own. Through tuning of acceleration coefficients, swarm size and function tolerance, the quality of solutions produced by multi-objective particle swarm OAs can be greatly improved while reducing the overall run time of the algorithm. PSO, similar to GA-based optimization, is very versatile and can be adapted to solve a wide range of optimization problems. When dealing with large search spaces, PSO often requires larger swarm sizes to maintain diverse solutions ensuring the algorithm does not converge to a local solution, slightly increasing the number of OF evaluations having an adverse effect on the run time of the algorithm. As each particle is able to make its own decisions based on its own position and velocity

47

as well as accessing the greater intelligence of the entire swarm, Particle Swarm based OAs are ideal for complex multivariable optimization problems such as multi-objective optimization of tractive IMs.
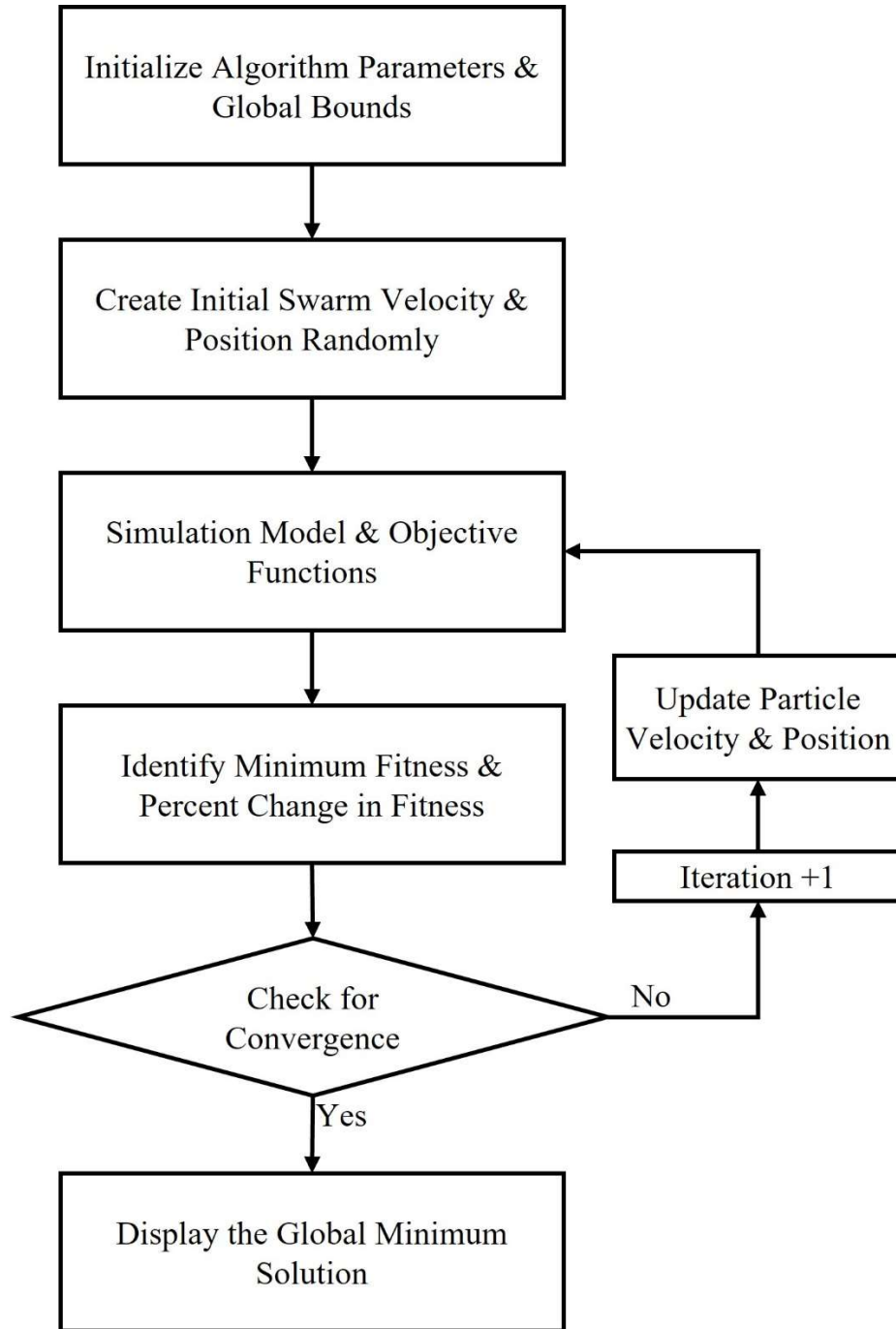
Fig. 2.8. The Iterative flow of a conventional particle swarm-based OA is depicted.

2.3.3. Genetic Algorithms

Genetic Algorithms (GA) draw inspiration from Darwin's principles of evolution, which states that through gene mutation and crossover, the fittest individuals will pass on dominant traits while weaker individuals with inferior traits will become extinct. Through simulating numerous generations, GAs are able rapidly solve for the global minimum of complex multi-objective optimization problems [109], [110]. GAs employ an iterative process where each iteration is called a generation. Each generation consists of a preset number of individuals representing a possible combination of input variables. The group of individuals within one generation is considered the current population. One or more OFs evaluate and assign a fitness value to each individual within the population that corresponds to its objective performance. In the case of multiple objectives, once an individual has been assigned an objective score for each objective, a total fitness score is assigned to the individual. Top ranking individuals with the lowest fitness scores of the current population are considered elite and are passed on to the next generation without change making up approximately five to ten percent of the next population. The remaining individuals to populate the next generation are created through the reproduction process. The first stage of reproduction consists of selecting individuals from the current population to be reproduced populating the next generation based on their fitness. The selection process is best demonstrated using a simple roulette wheel, as seen in Fig. 2.9 [60] to represent six individuals with fitness values shown in Table 2.3 and the results of selection in Table 2.4. The cumulative fitness is calculated for each individual, and a random number between zero and the total cumulative fitness is generated. The cumulative fitness range the random number falls in determines the selected individual to be reproduced in the next generation

49
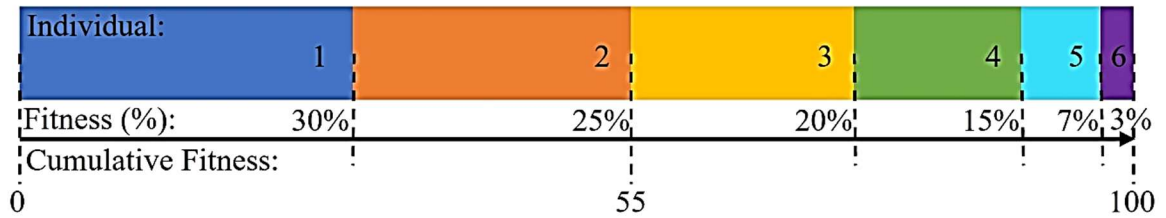
Fig. 2.9. Depicts the proportion of each individual's fitness score out of the total cumulative fitness represented by a linear roulette wheel

TABLE 2.2

ROULETTE WHEEL FITNESS

Individual	1	2	3	4	5	6
Fitness (%)	30	25	20	15	7	3
Cumulative Fitness	30	55	75	90	97	100

TABLE 2.3

ROULETTE WHEEL SELECTION

Roulette Wheel Spin	1	2	3	4	5	6
Random Fitness	54	9	64	96	28	82
Selected Individual	2	1	3	5	1	4

simulating the spinning of the roulette wheel. The selection process utilizes probability to generate the next population of six individuals containing individuals 2, 3, 4, 5 and two copies of individual 1. Individual 1 had the highest fitness value and, therefore, the highest probability of reproducing, resulting in two copies of 1 being selected for the next generation. Individual 6 no longer exists in the next generation as a result of a poor fitness score. The second stage of reproduction ensures that individuals share combinations of input variables to create entirely new individuals from two selected parents through and entirely new input variable combinations are created through individual mutations. The crossover operator combines traits of two parents at one or more random crossover points to produce two new offspring. The crossover probability may be adjusted by the optimizer

50

and determines how often the operator is performed. Consider the two individuals selected for crossover operations in Fig. 2.10(a) each containing 8 binary input variables. A crossover point is randomly generated and splits the parent function. The offspring produced clearly contain input variable combinations from both Parent A and Parent B allow for greater variation between generations and increased solution quality. Similar to crossover operations, the probability of an individual being selected for mutation is determined by the mutation probability. Mutation involves multiplying one or more input variables at random mutation location of the parent individual to inject new possible solutions into the next generation. In Fig. 2.10(b), individual 1 is selected as the parent,

Crossover Operator

Individuals Randomly Selected for Reproduction	
Individual 1	1 1 0 1 0 0 1 1
Individual 2	0 0 1 1 0 1 0 1

Crossover Point Randomly Selected	
Individual 1	1 1 0 1 0 0 1 1
Individual 2	0 0 1 1 0 1 0 1

Individual Created for Next Generation	
Individual 3	1 1 0 1 0 1 0 1
Individual 2	0 0 1 1 0 0 1 1

(a)

Mutation Operator

Individuals Randomly Selected for Reproduction	
Individual 1	1 1 0 1 0 0 1 1

Mutation Point Randomly Selected	
Individual 1	1 1 0 1 0 0 1 1

Individual Created for Next Generation	
Individual 1	1 1 0 1 1 0 1 1

(b)

Fig. 2.10. New solutions are introduced during selection. (a) Provides an example of the crossover operator applied to selected 8-bit binary numbers. (b) Demonstrates the use of the mutation operator on an individual.

51

mutations occurred at two mutation locations creating an entirely new individual for the next generation. The evolutionary algorithm iterates, as seen in Fig. 2.11. This ensures diversity amongst solutions as well as rapidly eliminating combinations of input variables with poor objective performance. Following the evaluation of each generation, the percentage change between the best know solution found within the current population, and the best-known solution of previous solutions are evaluated. If the percentage change is less than a set function tolerance indicating the algorithm has converged, or the algorithm reaches the maximum number of generations, the global optimal solution is displayed. If none of these criteria are met, reproduction generates the next generation. In the presence of multiple objectives, objective scores should be similar in magnitude and have equal effect on the total fitness of the individual. The fitness determines the best solutions of each generation, the selection process grants dominant individuals a higher probability of reproducing. Crossover ensures the traits if dominant individuals are shuffled together to create new configurations of input variables. Mutation ensures selected individuals randomly altered to improve population diversity, enhancing the overall solution quality. Through tuning of reproductive operators, GA parameters and OFs based on the specific application, the run time of the GA and the quality of the solution produced can be greatly improved. Several benefits of GA based multi-objective optimization include the use of parameter coding, simplifying complex problems to produce results quickly, reproductive operators depend on probability meaning the more generations are evaluated, the higher the solution quality and GAs are able to maintain large search spaces to avoid converging to a local minimum ensuring the global optimal solution is found. These benefits as well as the application flexible nature of GAs make them applicable to all aspects of IM design.

52
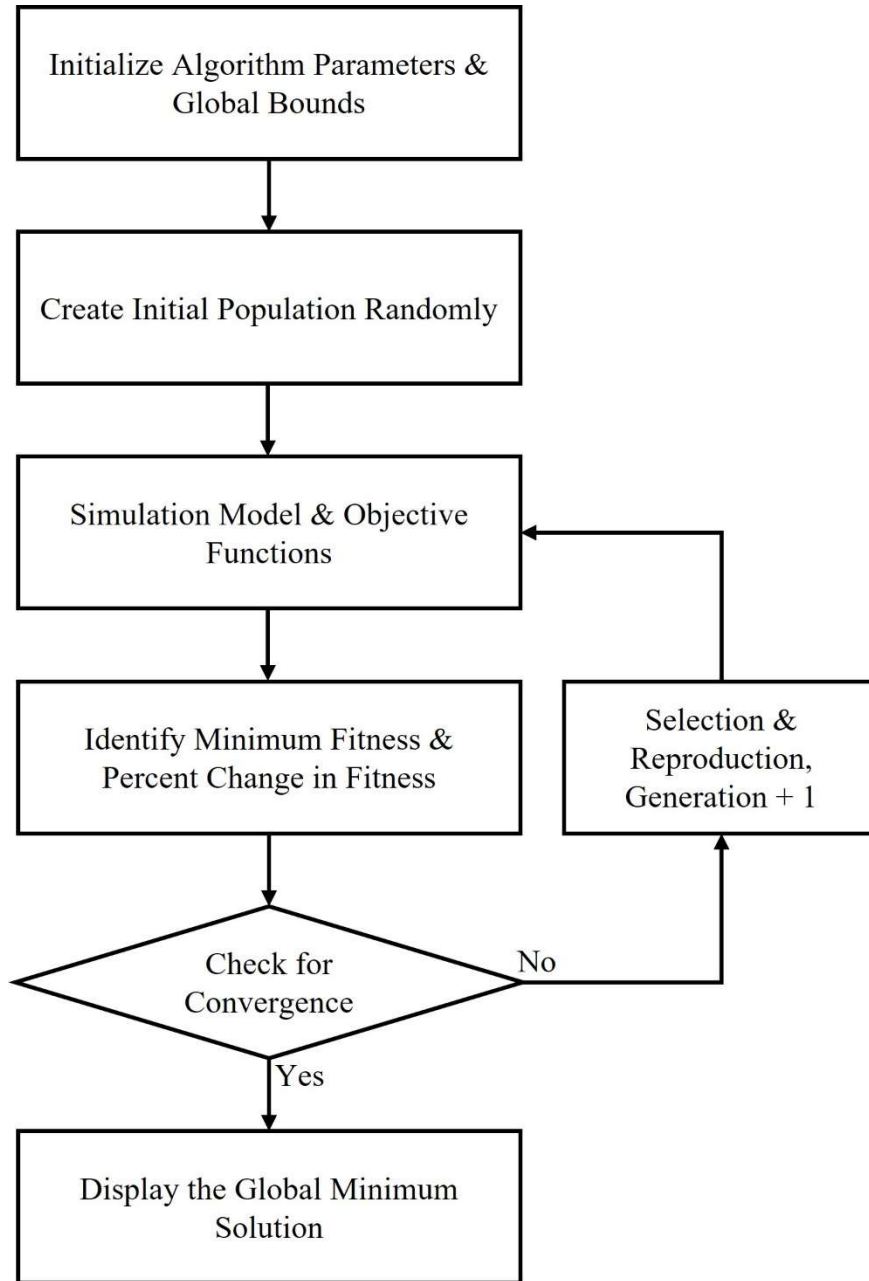
Fig. 2.11. The flow chart demonstrates the iterative process of a conventional GA.

2.3.4. Schwefel Function Minimization Case Study

The following case study will examine the performance of a PS, GA and PSO when applied to minimize a multi-variable single objective optimization test function [111]. Optimization test functions are designed to have several local maximums and minimums, potentially tricking the algorithm into converging prematurely. In addition to local minima,

53

many test functions have large search spaces and rapid fluctuations in function value. The optimization test function seen in Fig. 2.12 selected for this study is called the Schwefel Function and is represented by (17) where a_j represents the input variables to be optimized and $f(a_j)$ is the OF to be minimized.

$$f(a_j) = 418.9829d - \sum_{j=1,2,...}^{d} a_j \sin\left(\sqrt{|a_j|}\right) \tag{17}$$

The input variables are bound between [-500,500], leaving a relatively large search space for the algorithms to process. There are three prominent local minima that lie on the Schwefel Function surface and only one global minima at $f(420.9687, 420.9687) = 0$. Algorithm parameters such as the population, function tolerance, stall generations and resolution are kept constant across all three algorithms to ensure an equal comparison. Table 2.4 contains the algorithm parameters of each respective OA. The importance of this comparison is to analyze each algorithms speed through run time, number of function evaluations, stall time and solution quality to determine which algorithm would be best suited for multi-objective IM design optimization. The PS based algorithm is expected to
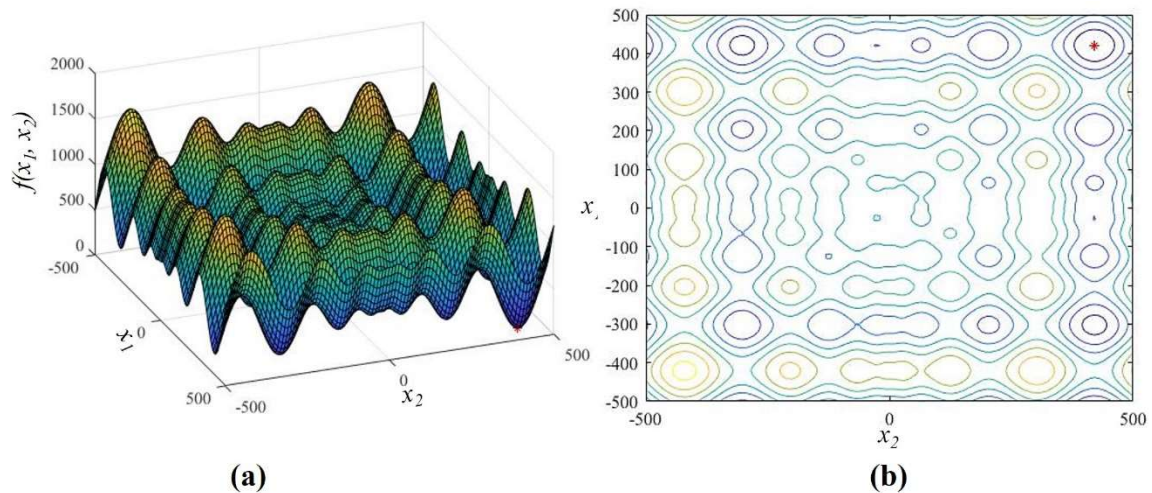
Fig. 2.12. Optimization test functions allow for algorithms to be equally compared. (a) Depicts a surface plot of the Schwefel Function. (b) Shows a contour plot of the Schwefel function with its minimum in red.

54

TABLE 2.4

OPTIMIZATION ALGORITHM PARAMETERS

PS Optimization		PSO		GA Optimization	
Parameter	Value	Parameter	Value	Parameter	Value
Maximum Iterations	25	Maximum Iterations	500	Maximum Iterations	500
Max Stall Iterations	5	Max Stall Iterations	25	Max Stall Iterations	25
Function Tolerance	10^{-6}	Function Tolerance	10^{-6}	Function Tolerance	10^{-6}
Global Upper Bound	[500, 500]	Global Upper Bound	[500, 500]	Global Upper Bound	[500, 500]
Global Lower Bound	[-500, -500]	Global Lower Bound	[-500, -500]	Global Lower Bound	[-500, -500]
Reduction Factor	25%	Swarm Size	200	Population Size	200
Resolution	100	Global Vector Constant	40%	Crossover Fraction	30%
Resolution Factor	15%	Local Vector Constant	25%	Mutation Fraction	10%

be the slowest of the three algorithms due to its high number of computations to maintain a comparable solution resolution. PS algorithms provide the most information about the Schwefel Function surface within several initial generations. After the initial generations,

the individuals located at any of the three local minima are expected to become extinct, and the algorithm should converge to the global optimal solution. Similarly, the particles of the particle swarm algorithm will be widely spread during the few initial generations. In later generations, the Particle Swarm algorithm will likely locate the global minima slightly faster than the GA. However, it will take longer to settle on a final solution. For this reason, the run time and solution quality of both the GA and the Particle Swarm algorithm will likely be similar to one another. Each algorithm will be run five times, and the average performance can be seen in Table 2.5. After running each algorithm multiple times, it is

TABLE 2.5

OPTIMIZATION ALGORITHM PERFORMANCE

Optimization Algorithm	PS	PSO	GA
Total Iterations	13	52	39
Algorithm Run Time	1.4560s	9.3813s	7.4137s
X1 Solution	420.9706	420.9687	420.9687
X2 Solution	420.9706	420.9687	420.9687
Function Value at Solution	2.633 x10^{-5}	2.5455 x10^{-5}	2.5455 x10^{-5}
Error In Solution	0.002633%	0.0025455%	0.0025455%

evident that the PS algorithm had the longest average run time. The PS algorithm was also able to identify the global minimum of the Schwefel Function surface. However, for the purpose of complex multi-objective optimization, a PS-based algorithm is to computationally inefficient. Fig. 2.13 shows the depicts the iterative improvements made by the PS, while Fig. 2.14 demonstrates the population of particles and individuals at
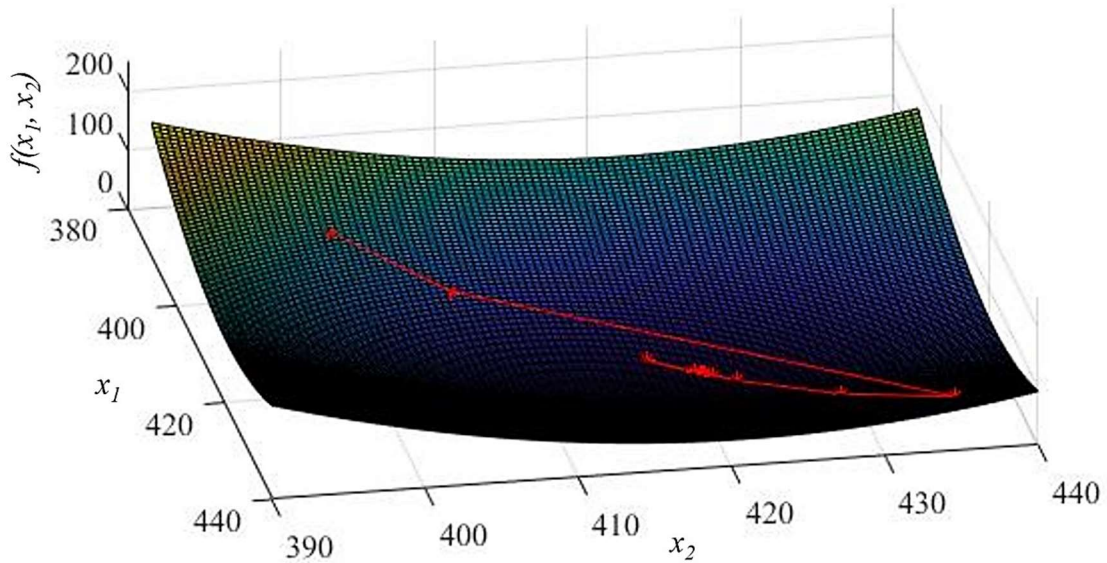
Fig. 2.13. Depicts the migration of the best-known solution of the PS algorithm over the 13 limit reduction iterations the PS algorithm performed.

56
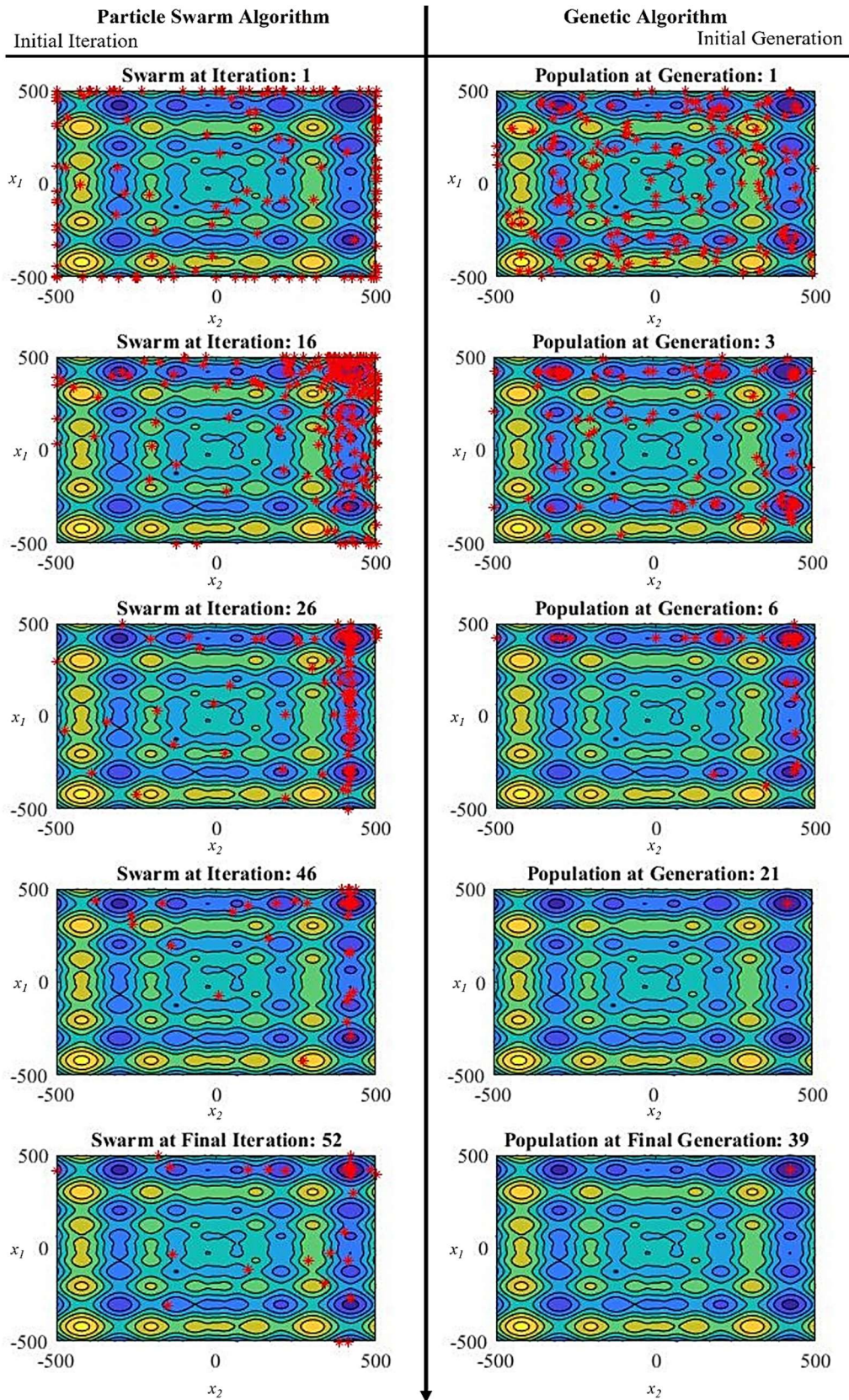
Fig. 2.14. Visualizes different stages of the particle swarm and GA optimization.

57

various stages of the algorithm. The initial populations of both the GA and The PSO are widely spread across the search space before collapsing to the lowest valleys of the Schwefel Function surface. The Particle Swarm algorithm maintains a wider spread for several generations longer than GA before both collapses on the global minima. The GA was able to converge after 39 iterations, while the PSO required an additional 11 iterations leading to the longer run time. The particle search algorithm was the quickest algorithm however had the solution yielded a larger error than particle swarm or GA-based optimization. The total population of the GA was centered about the optimal solution in later generations, which shows higher confidence in the global optimal solution as the entirety of the population has migrated to this region. In conclusion, the case study has shown that the PS-based algorithm is least suited for complex optimization. Although both the GA and PSO performed extremely well, both converging to the optimal solution in under 9.38 s, the GA settled to the global optimal solution quicker and are known to be extremely efficient at managing multiple objectives and is less susceptible to local solutions when dealing with unconstrained optimization problems. Therefore, a GA based optimization strategy is selected for multi-objective rotor bar optimization of a tractive IM.

CHAPTER 3   Eliminating Function Bias in Multi-Objective Rotor Bar

Optimization Through Novel Objective Function Modeling

3.1. Significance of Objective Function Modeling

When dealing with complex multi-objective optimization problems such as IM optimization, the magnitude and search space of both input variables and output performance used to define objectives can vary greatly. A large difference in magnitude between objective function (OF) scores can lead to an imbalance between the weight and overall score of an individual as a result of one objective dominating the total OF score. In this case, the remaining objectives have little effect on the fitness of each individual, essentially limiting the optimization to the dominating objective. To ensure a high-quality balanced solution across all objectives, the use of OF modeling allows the optimizer to manipulate the target, magnitude, and contribution of each objective towards the total fitness score of an individual. OF scalars or weights may be applied to adjust the magnitude of objectives. However, the optimizer must be careful not to lose information about the true objective while applying any form of OF scaling. The addition of an offset to balance objectives is also possible. However, it can introduce reverse bias into the objective, especially when the magnitude of the global minimum is unknown. Lastly, OF modeling is used to formulate objectives to target either maximization or minimization of the OF. GAs and other multi-objective OAs must search for either the global maximum or minimum of a search space meaning all OFs must all be modeled as either a maximization or minimization problem. In the process of targeting OFs, once again, large differences in magnitudes between objectives may arise, leading to OF bias. In the following chapter,

several forms of conventional OF modeling are analyzed with respect to their ability to provide the algorithm with a balanced comparison between multiple objectives. The drawbacks of these conventional approaches are identified and discussed, leading to the development of a novel hyperbolic tangent based OF model that eliminates OF bias while optimizing the rotor bar geometry for maximal torque and minimal losses of a tractive IM. Lastly, the performance of a multi-objective GA using conventional OFs is compared to the performance of a GA using hyperbolic tangent based OFs to demonstrate the effectiveness of hyperbolic tangent based OF modeling at eliminating function bias.

3.2. Conventional Objective Function Modeling

Torque and loss-oriented optimization of a tractive IM requires some form of OF modeling such that the torque OF is minimized while the true torque is maximized. A base design is often used as a reference in optimization functions as it is a constant and known combination of input variables and their corresponding performance. This can be used to offset or center OFs around a known starting point when applied correctly. The use of exponential based OFs can be used to exploit rapid changes in slope to amplify the global and local minimums and maximums. (18), (19), and (20) [36], [112], [113] are three examples of conventional approaches to OF modeling applied to maximize the torque. Fig. 3.1 illustrates the behavior of each OF over a 60% variation of the base torque.

$$OF_{tor_i}^1 = \frac{1}{T_{out_i}} \tag{18}$$

$$OF_{tor_i}^2 = \left(T_{ref_i} - T_{out_i}\right) \tag{19}$$

$$OF_{tor_i}^3 = \left|T_{ref_i} - T_{out_i}\right| \tag{20}$$

Conventional OF (18) uses the base torque as a reference point, linearly passing the error between the base torque and the output torque produced by the algorithm. Therefore, the

60
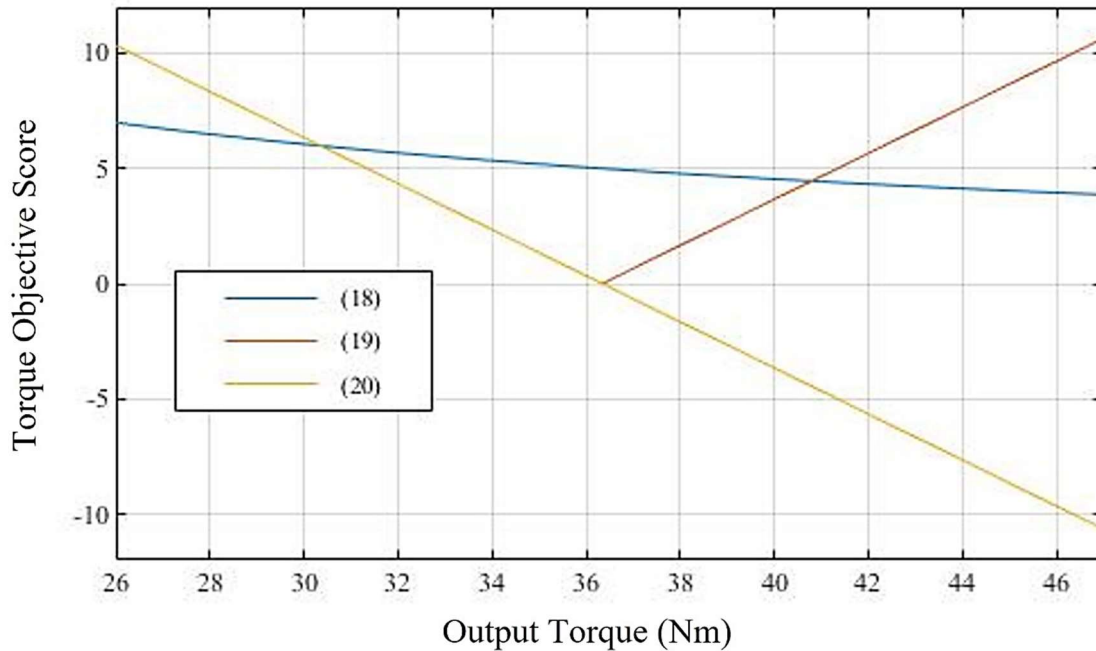
Fig. 3.1. Three conventionally used OFs given by (18), (19) and (20) are evaluated over a 60% range of the base design [36], [112], [113].

OF score is a decreasing positive integer if the output torque is less than the base torque, zero when the output torque is equal to the base torque, and an increasingly negative integer if the output torque is better than that of the base design. The drawback of this approach to OF modeling is that it introduces negative OF scores which increases algorithm complexity and may introduce OF bias negatively effecting solution quality. In addition to containing negative values, OF has an unbounded output meaning the range of possible OF scores is unknown. By taking the absolute value of the error between the base torque and the output torque in (19) eliminates the possibility of negative OF scores and bounds the minimum value of the OF to the base torque. Although the lower bound of the OF is now known, the minimum value corresponds to the base torque meaning the best possible OF score will result when the base torque is produced by the algorithm. This is useful when attempting to maintain output parameters however does not provide the GA with any incentive to improve the output torque. Finally, with the use of the base torque as a reference, an

61

exponential modification is applied to the output torque produced by the GA, to form (20). When the output torque of the GA is smaller than that of the base torque, the OF value rapidly increases, as soon as the base torque is achieved and the algorithm begins to produce output torque performance higher than that of the base torque, OF gradually approaches zero to allow for fine tuning of the objective. OF (20) strongly penalizes any individual with output torque less than the base torque, which quickly eliminates poor solutions from the population leading to quicker convergence. Once again, the lower bound of the OF is known. However, the major drawback of this type of OF modeling is that due to the slow decay of the OF after the base torque. As the output torque continues to improve, the OF value will continue to decrease at an increasingly slower rate losing its sensitivity to output torque improvement. This means that a 5% improvement over the base torque would yield an OF score 10% lower than the base design, while a 10% improvement in the output torque would only cause a 15% lower OF score despite improving the output torque by twice as much. This can lead to premature stalling of the algorithm due to a loss of sensitivity to objective change or OF bias due to a large fluctuation in magnitude in multi-objective applications. OF bias is when one objective contributes significantly more to the overall fitness score of an individual misleading the GA to favour the dominating objective over the other [114]. The result of OF bias is a low-quality optimal solution in which the performance of the dominated objective is essentially ignored, and the problem is optimized with respect to only the dominating objective. The torque and losses of a tractive IM are of different magnitude, and therefore careful OF modeling must be applied to ensure a fair comparison between both objectives. The conventional OF for torque maximization is represented by (21), in which an exponential decaying function is oriented

62

about the base torque ensuring poor fitness scores for individuals with low torque production. Equation (22) is the conventional OF for total loss minimization by simply passing the true losses as OF scores [115], [116].

$$OF_{tor_i} = \frac{1}{\left|T_{ref_i} - T_{out_i}\right|} \tag{21}$$

$$OF_{loss_i} = P_{loss_i} \tag{22}$$

To demonstrate the effect of OF bias on an individual's fitness score during multi-objective optimization of tractive IMs, Fig. 3.2 plots the OF score of (24) with respect to a 60% variation of the base torque and OF scores of (25) over the same range with respect to the total losses. Each plot contains three test points, the base point B represents the base torque and its associated OF score, A represents a 5% improvement in output torque with respect to the base torque, and its associated OF score, and C represents an output torque 5% lower than the base torque and its associated objective score. The same process is used to
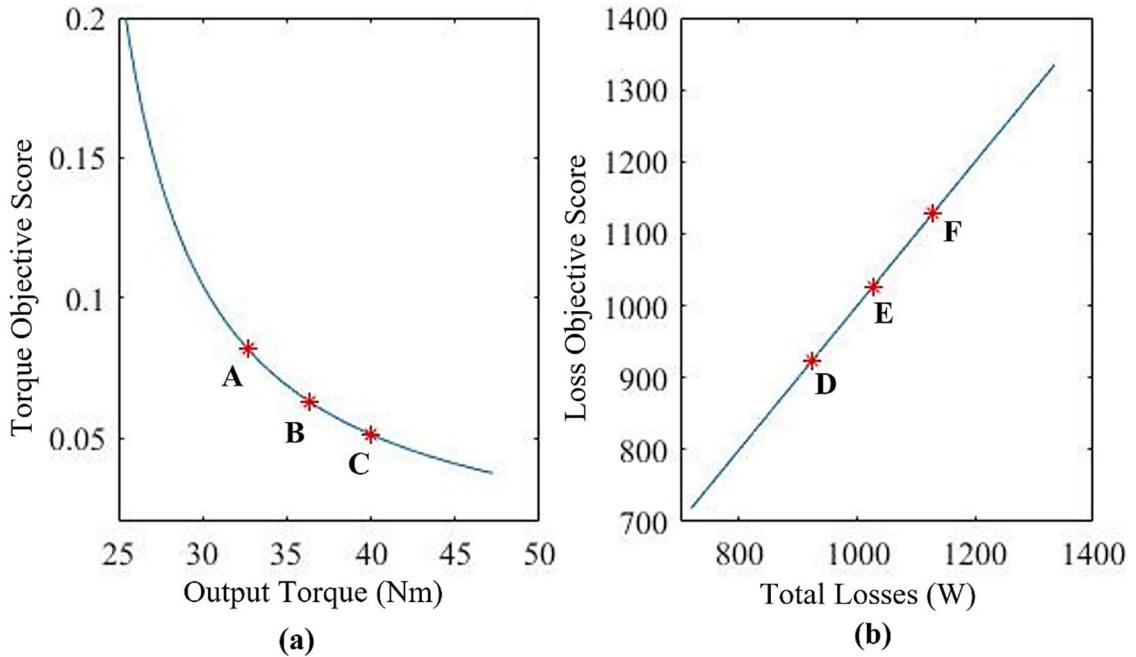
Fig. 3.2. Test points A to F have been placed on conventional OFs to demonstrate function bias. (a) Depicts the torque OF conventionally defined by (21). (b) Plots the total loss OF defined by (22).

63

determine points D, E and F with respect to the total losses. It is important to recall that each individual within a population will have one OF score for each objective which is then summed together to come up with the total fitness of the individual. To test conventional OFs for OF bias, Table 3.1 evaluates six possible individuals and their associated total fitness scores. Through observing the percentage change in total fitness score of individuals with various torques and total losses, the overall effect of each objective on the total fitness score can be determined. Analysis of the OF bias test verifies that the torque objective is clearly dominated by the loss objective as a result of a large difference in magnitude between OF scores. Any individual that saw an increase in torque was only assigned marginally lower total fitness scores. However, individuals that saw a reduction in losses were assigned 10% lower fitness scores than the base individual. Individual 6 shows an example of how the use of unbounded exponential functions can introduce reverse bias causing a poor torque to completely dominate an improvement of the same magnitude in the loss objective.

TABLE 3.1

FUNCTION BIAS TEST ON CONVENTIONAL OBJECTIVE FUNCTIONS

Individual	Base Design	1	2	3	4	5	6
Torque (Nm)	36.34	39.97	32.71	36.34	36.34	39.97	32.71
Total Losses (W)	1026.80	1026.80	1026.80	924.12	1129.48	1129.48	924.12
Torque Objective Score	0.06	0.05	0.08	0.06	0.06	0.05	0.08
Loss Objective Score	1026.80	1026.80	1026.80	924.12	1129.48	1129.48	924.12
Total Fitness Score	1026.86	1026.85	1026.88	924.18	1129.54	1129.53	924.20
Change in Fitness	0.00	0.00	0.00	10.00	-10.00	-10.00	10.00

3.3. Novel Hyperbolic Tangent Based Objective Functions

When considering multiple objectives for optimization, the ideal OF assigns an objective score for each objective between equal and known upper and lower bounds, while using the base design as a reference providing an evenly weighted transition in OF score on both sides of the base performance. To attain an unbiased comparison between multiple objectives, a novel approach to OF modeling is proposed to eliminate OF bias between the output torque and total losses of a tractive IM. The output torque and total losses of an individual are passed to the multi-objective GA though hyperbolic tangent based OFs (23) and (24) to be minimized, constraining both OF scores to equal bounds.

$$\text{OF}_{\text{tor}_i}(\text{gen}) = \frac{1}{2} \times \left(1 - \tanh\left(\left[\frac{T_{\text{out}_i}(\text{gen}) - T_{\text{base}_i}(\text{gen})}{T_{\text{base}_i}(\text{gen})}\right]\right)\right) \tag{23}$$

$$\text{OF}_{\text{loss}_i}(\text{gen}) = \frac{1}{2} \times \left(1 + \tanh\left(\left[\frac{P_{\text{loss}_i}(\text{gen}) - P_{\text{base}_i}(\text{gen})}{P_{\text{base}_i}(\text{gen})}\right]\right)\right) \tag{24}$$

OF_{tor_i} represents the OF score of an individual with respect to its output torque performance while OF_{loss_i} represents the total loss objective score. Evaluating torque and loss performance of each individual based on the base design performance ensures an equally weighted OF score with respect to an equal improvement in each objective. To demonstrate how function bias in multi-objective optimization of tractive IMs is eliminated, Fig. 3.3 depicts the plot of OF score with respect to a 30% range above and below the base performance for each objective. The objective score at the base torque is denoted by B, while E represents the total losses of the base design. To perform a function bias test, A represents a torque performance 5% lower than that of the base design, while C represents an output torque 5% higher than that of the base design. Similarly, D and F give OF scores for a total loss performance 5% below and 5% above the base design losses.

65
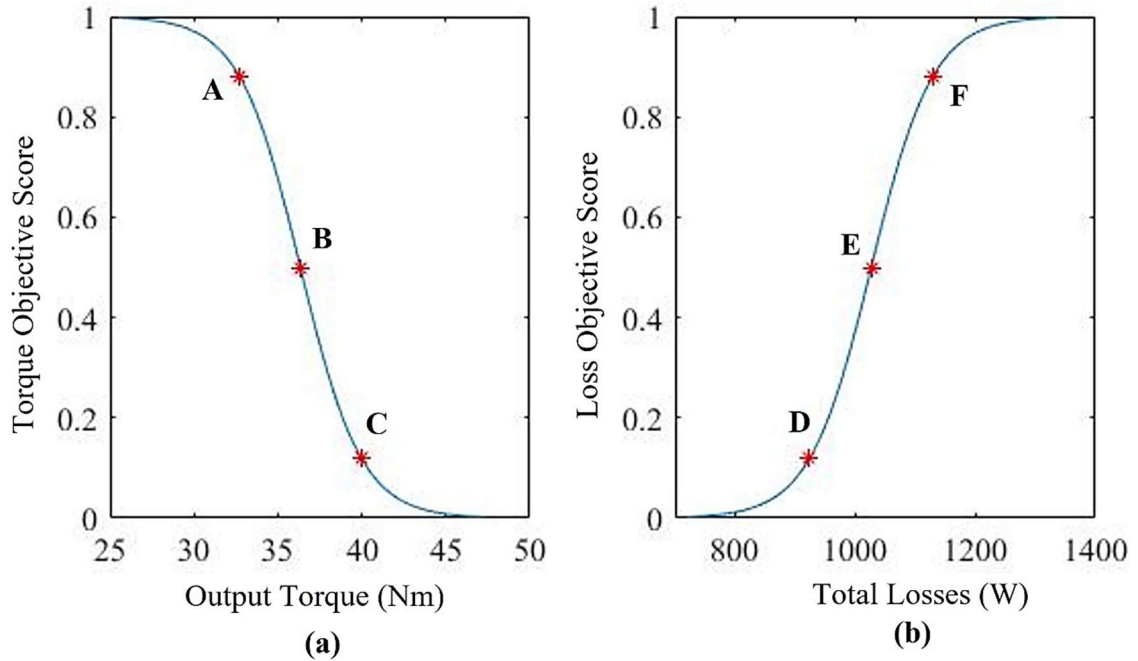
Fig. 3.3. Test points A to F have been placed on the proposed novel OFs to demonstrate the resilience to function bias. (a) Depicts the hyperbolic tangent-based torque OF defined by (23). (b) Plots the hyperbolic tangent-based total loss OF defined by (24).

Table 3.2 evaluates OF scores and total fitness of six individuals with different objective performances. To analyze the impact of an increase or decrease in either objective on the total fitness of each individual, the percentage change in total fitness of a test individual is compared to the total fitness of the base design. If no function bias exists between opposing objectives, individuals with a 5% improvement in torque while maintaining the same losses as the base design should see the same percentage increase in fitness score as an individual with 5% lower losses while maintaining the base torque performance. It can be seen from the function bias test that, as predicted, individual 1 and individual 4 both saw a 5% increase in one objective while maintaining the base performance in the other objective and the percentage change in total fitness in both cases was 38.08%. The same can be seen for individuals 2 and 3, who saw a 5% decrease in one objective while maintaining base performance in the other. Lastly, individuals 5 and 6 demonstrate that a 5% increase in one

TABLE 3.2 FUNCTION BIAS TEST ON NOVEL OBJECTIVE FUNCTIONS

Individual	Base Design	1	2	3	4	5	6
Torque (Nm)	36.34	39.97	32.71	36.34	36.34	39.97	32.71
Total Losses (W)	1026.80	1026.80	1026.80	924.12	1129.48	1129.48	924.12
Torque Objective Score	0.50	0.12	0.88	0.50	0.50	0.12	0.88
Loss Objective Score	0.50	0.50	0.50	0.12	0.88	0.88	0.12
Total Fitness Score	1.00	0.62	1.38	0.62	1.38	1.00	1.00
Change in Fitness	0.00	38.08	-38.08	38.08	-38.08	0.00	0.00

objective is offset by a 5% decrease in the opposite objective resulting in a fitness score equal to the base design. The results of the function bias test confirm that hyperbolic tangent based OFs (23) and (24) are extremely effective at eliminating OF bias when performing multi-objective design optimization of a tractive IM. To allow the optimizer to have more control over the hyperbolic tangent based OFs, (25) and (26) have been modified to incorporate a bias factor K_{Bias} representing a scalar between 0 and 1 and scaling factors for each objective K_{tor} and K_{loss}. The bias factor allows the optimizer to inject bias into the optimization problem in the case that one objective is more significant than the opposing objective.

$$OF_{tor_i}(gen) = (1 - K_{Bias}) \times \left(1 - \tanh\left(K_{tor} \times \left[\frac{T_{out_i}(gen) - T_{ref}(gen)}{T_{ref}(gen)}\right]\right)\right) \quad (25)$$

$$OF_{loss_i}(gen) = (K_{Bias}) \times \left(1 + \tanh\left(K_{loss} \times \left[\frac{P_{loss_i}(gen) - P_{ref}(gen)}{P_{ref}(gen)}\right]\right)\right) \quad (26)$$

Scaling factors allows the optimizer to tune the transition region of each respective OF short transition regions reward even the smallest increase in objective performance significantly. However, quickly loses its sensitivity of any further improvement. This is

67

ideal when the improvement in a specific objective is expected to be small as poor solutions are quickly extinct. Long transition regions allow the GA to gather more information for the fine tuning of objectives as larger changes in objective score result in significantly higher fitness when compared to individuals with smaller improvements in objective performance. If the transition region is too wide, however, the OFs will flatten out, and only a minimal change in fitness will be observed over the entire search space. The effect of bias and scaling factors on the OF scores are depicted in Fig. 3.4. Table 3.3, 3.4, and 3.5 proposes the three cases. The first case applies no bias to either objective and small scaling factors and serves as a reference giving an even contribution to both objectives and a moderate transition region. The second case applies a bias toward the loss objective by 25% while maintaining the same moderate scaling factor resulting in the loss
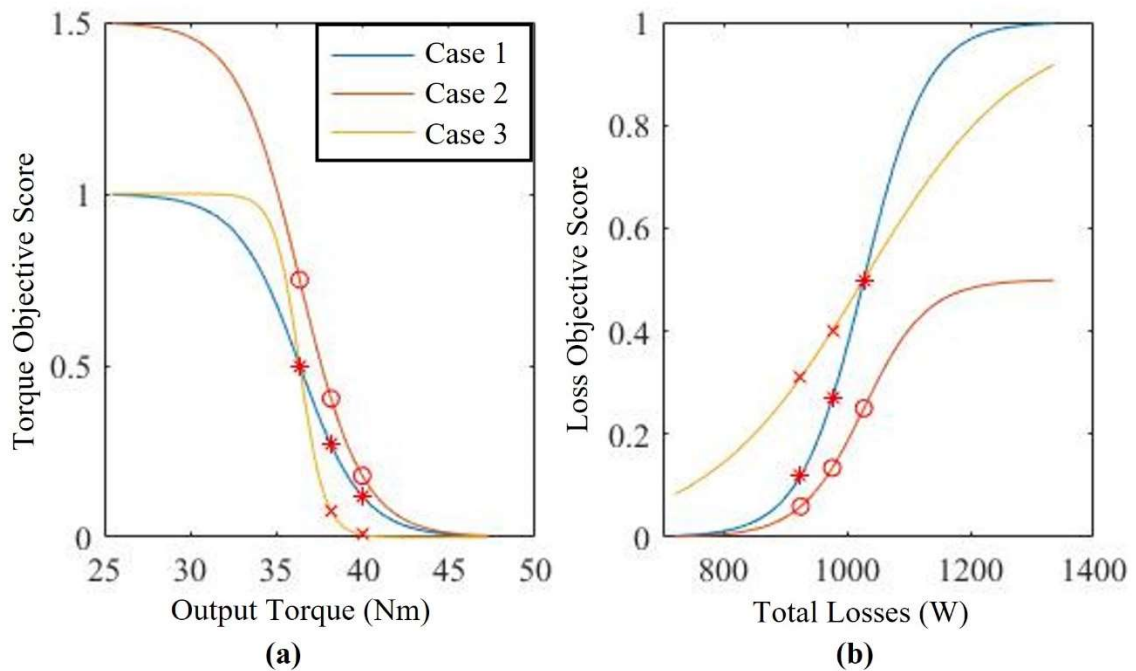
Fig. 3.4. Nine test points have been placed on the proposed novel OFs to demonstrate bias and scaling factors. (a) Depicts the hyperbolic tangent-based torque OF defined by (25) under three cases. (b) Plots the hyperbolic tangent-based total loss OF defined by (26).

68

TABLE 3.3

NOVEL OBJECTIVE FUNCTION BIAS AND SCALING TEST - CASE 1

Case 1: No Bias and No Transition Scaling					
Individual	Base Design	1	2	3	4
Torque (Nm)	36.34	38.1570	39.9740	36.34	36.34
Total Losses (W)	1026.80	1026.80	1026.80	975.46	924.12
OF Tor Score	0.50	0.2689	0.1192	0.50	0.50
OF Loss Score	0.50	0.50	0.50	0.2689	0.1192
Total Fitness Score	1.00	0.7689	0.6192	0.7689	0.6192
Change in Fitness	0	23.1059	38.0797	23.1059	38.0797
Contribution of Torque Objective	50.0	34.9755	19.2510	65.0245	80.7490
Contribution of Loss Objective	50.0	65.0245	80.7490	34.9755	19.2510

TABLE 3.4

NOVEL OBJECTIVE FUNCTION BIAS AND SCALING TEST - CASE 2

Case 2: 50% Bias Towards Torque Objective and No Transition Scaling					
Individual	Base Design	1	2	3	4
Torque (Nm)	36.340	38.157	39.974	36.340	36.340
Total Losses (W)	1026.80	1026.80	1026.80	975.460	924.120
OF Tor Score	0.750	0.403	0.179	0.750	0.750
OF Loss Score	0.250	0.250	0.250	0.134	0.060
Total Fitness Score	1.0	0.653	0.429	0.884	0.810
Change in Fitness	0	34.659	57.120	11.553	19.040
Contribution of Torque Objective	75.0	61.739	41.698	84.796	92.638
Contribution of Loss Objective	25.0	38.261	58.302	15.204	7.362

TABLE 3.5

NOVEL OBJECTIVE FUNCTION BIAS AND SCALING TEST - CASE 3

Case 3: No Bias with Positive Torque & Negative Loss Scaling					
Individual	Base Design	1	2	3	4
Torque (Nm)	36.34	38.1570	39.9740	36.34	36.34
Total Losses (W)	1026.80	1026.80	1026.80	975.46	924.12
OF Tor Score	0.50	0.0759	0.0067	0.50	0.50
OF Loss Score	0.50	0.50	0.50	0.4013	0.310
Total Fitness Score	1.0	0.5759	0.5067	0.9013	0.810
Change in Fitness	0	42.4142	49.3307	9.8688	18.9974
Contribution of Torque Objective	50.0	13.1731	1.3209	55.4747	61.7265
Contribution of Loss Objective	50.0	86.8269	98.6791	44.5253	38.2735

objective contributing 25% more to the total fitness of an individual. The third case applies

no bias to either objective. However, it scales the transition region of the torque objective

to be narrow while the loss objective's transition region is extremely wide. Test points are

taken at the base performance of each objective as well as at a performance 2% and 5%

better than the base performance and represent a small improvement and a large

improvement in objective performance, respectively. These test points can be seen for each

case in figure 3.4 denoted by points A to E. In each case, four individuals are evaluated

based on their objective performance, the contribution of each objective score to the total

fitness of each individual is calculated, and the change in total fitness is then compared to

the total fitness of the base design to determine the performance of OFs (25) and (26). Case

one demonstrates that with no bias and moderate scaling, both OFs contribute equally to

the overall fitness score of each individual. Individuals 1 and 3 who saw small

improvements in one objective saw small improvements in total fitness over the base design, while individuals 2 and 4 who saw large improvements in one objective were rewarded significantly lower OF scores resulting in a larger change in total fitness with respect to the base design. When bias is applied towards the loss objective, the base individual confirms that the torque objective is now only contributing 25% to the overall fitness score while the loss objective is contributing 75%. For this reason, individuals 3 and 4 who saw an increase in loss performance are seen to have a greater change in total fitness than individuals 1 and 2 who saw an equal improvement in the torque objective. The effect of scaling on the OFs ability to differentiate between a small and large improvement in objective performance is demonstrated by the third case. The torque objective is seen to have a narrow transition region, and therefore the difference in percentage change between the fitness score of individual 1 and individual 2 is only 6% despite individual 2 having a 3% larger improvement in objective performance. The loss objective has been scaled to have an extremely wide transition region resulting in fitness scores of individuals 3 and 4 being very close. This case demonstrates the importance of tuning OFs to fit the application. A narrow transition region will quickly result in a low objective score however is not sensitive to larger improvements in objective performance, while a wide transition region may not converge to a low objective score because the function demands too much improvement from the objective. When tuned correctly, hyperbolic tangent based OFs are the ideal method for constraining the objectives of multi-objective optimization of tractive IMs, ensuring an equal comparison between all objectives.

CHAPTER 4   Enhanced Solution Quality Multi-Objective Rotor Bar

Optimization Through Adaptive Restart Capabilities

To further enhance the robustness, performance and solution quality of the non-dominated multi-objective GA used for torque density and operating efficiency optimization, aspects of both conventional PS and particle swarm OAs are adapted and applied to the GA. To reduce the function tolerance, number of stall iterations, and the maximum number of generations required for the GA to converge, resulting in reduced run times and total function evaluations, an adaptive restart condition is applied prompting the GA to restart unless certain restart criteria are met. Adopting the local search space reduction method employed by PS algorithms, the local limits of the algorithm are decreased allowing the same number of individuals within the population to evaluate a smaller, more focused local search space centered about the best solution known to the algorithm. In addition to restricting the search space of the algorithm, the centroid of all OFs is updated each restart iteration, ensuring OFs maintain sensitivity to larger improvements in performance over numerous iterations. Similar to particle swarm-based optimization, updating the best know solution known as the centroid each restart iteration allows the OFs to learn from the precious best-known solution maintaining its effectiveness at offering unbiased OF scores. The iterative flow of the non-dominated adaptive restart GA can be seen in Fig. 4.1 and begins with the initialization of all parameters and the generation of the first population. In the case of the first iteration, the best know solution is the base performance of baseline tractive IM and the local limits are set to the global limits set by the design constraints. The initial population of individuals are fed to the permeance based equivalent circuit model to determine their tractive performance with
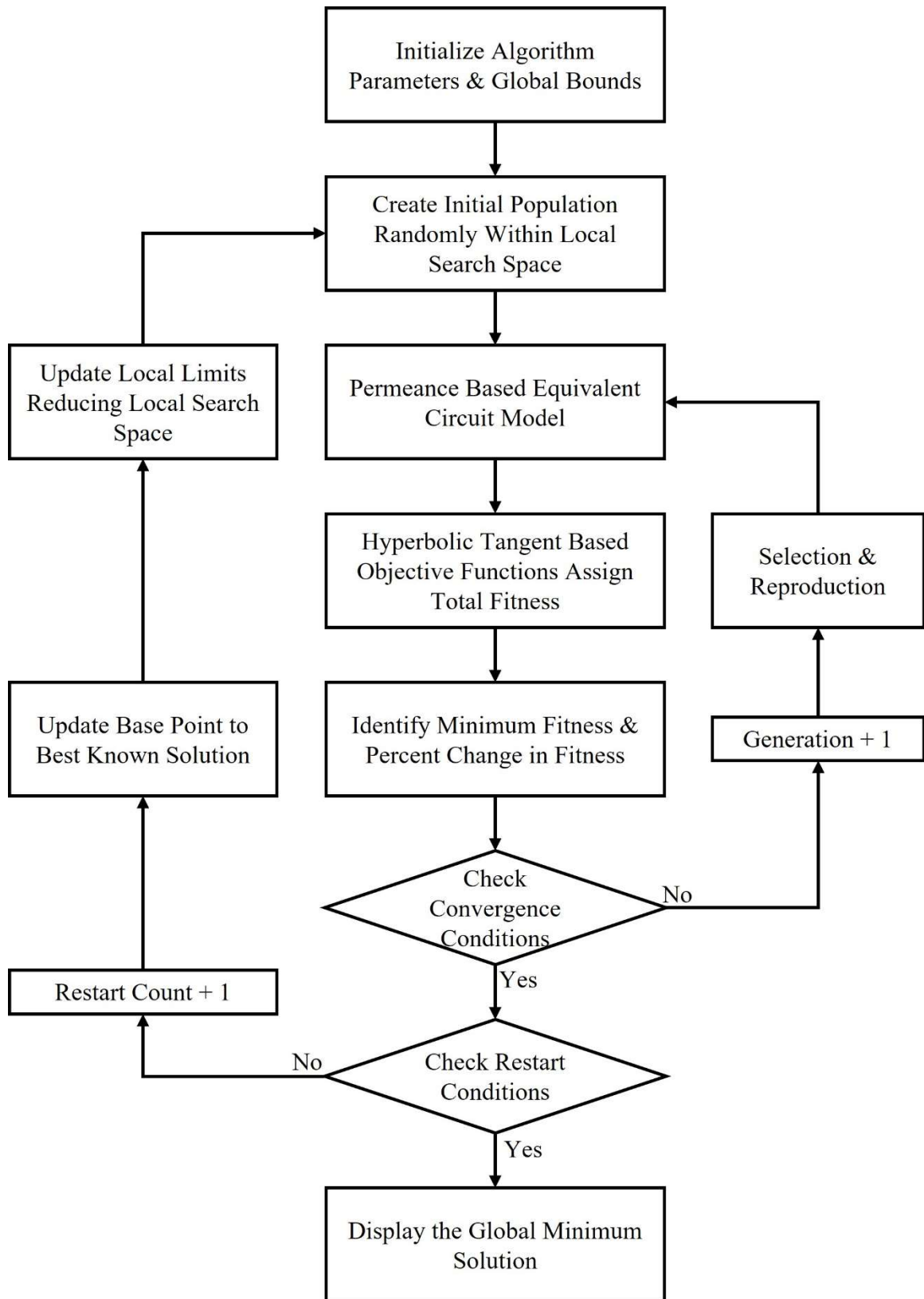
Fig. 4.1. The nested iterative flow of the proposed non-dominated, novel adaptive restart GA for to be implemented to optimize the rotor bar of the baseline IM.

73

through the hyperbolic tangent based OFs assigning a non-dominated total fitness value to each individual. The change in total fitness of the best know solution at each generation is evaluated, and if the function tolerance has not been met, the current population undergoes selection to create the next generation of individuals. If the function tolerance is met, the GA has converged to the best-known solution of the optimization problem and the restart tolerance is checked. The restart tolerance monitors the change in improvement between the base design and the optimal solution produced by the GA at each restart iteration. If the respect to the output torque and losses. Each individual's tractive performance is then evaluated, and the restart tolerance or the maximum number of restarts are checked. If either is met, the adaptive restart algorithm converges to a global optimal solution that is displayed to the optimizer. If the restart tolerance is not met, the adaptive restart GA updates the upper and lower bounds of the algorithms search space with respect to each geometric input variable is reduced. The advantage of reducing input variable bounds with respect to the best-known performance of the centroid is that it gives the adaptive restart GA the ability to reduce the search space concentrating the population in an area where the current best-known combination of input variables is present while assigning an unbiased total fitness score to each individual of the current population. Every restart iteration is that the bounds of the search space are reduced by (27) and (28), in which the local limits are centered around the centroid and decreased by the reduction coefficient K_{red}.

$$L_{ub_j}(\text{iter}) = c_j(\text{iter} - 1) + (1 - K_{red}) \times \left| L_{ub_j}(\text{iter} - 1) - c_j(\text{iter} - 1) \right| \quad (27)$$

$$L_{lb_j}(\text{iter}) = c_j(\text{iter} - 1) - (1 - K_{red}) \times \left| L_{lb_j}(\text{iter} - 1) - c_j(\text{iter} - 1) \right| \quad (28)$$

The best-known local solution is denoted by c_j representing the best-known combination of input variables and their associated performance. Similar to the search space reduction

74

seen in PS algorithms, the reduction in search space focuses the adaptive restart GA on combinations of input variables that result in higher objective performance. The population examines smaller search spaces in less time while at a higher resolution resulting in a reduction in run time of the overall algorithm while increasing the quality of the global optimal centroid produced. To further reduce the run time of the adaptive restart GA, the function tolerance and stall iterations of the algorithm should be set higher than conventional GAs allowing the algorithm to converge quickly while sacrificing the solution quality of local centroids. The restart tolerance, however, should be set low forcing the algorithm to continue to iteratively restart until no more improvement over the base design is observed in either objective producing a high-quality local centroid is produced which is then considered the global centroid containing the geometry and objective performance of the optimal design. Each adaptive restart performed enhances the confidence that the global centroid produced is in fact, the global optimal solution producing the ideal rotor bar geometry for a tractive IM.

CHAPTER 5   Rotor Bar Optimization Considering Dynamic Operating Conditions Through Energy Center of Gravity Clustering

5.1. Significance of Considering Dynamic Operating Conditions

Industrial IMs designed to run at a single operating frequency under similar load conditions may be optimized to offer peak objective performance for a single specific operating point. The same is not true for tractive IMs must perform optimally across the extremely wide operating ranges required for vehicle applications. To truly arrive at the optimal rotor bar geometry for a tractive IM, optimization must be performed under various dynamic operating conditions since the best rotor bar geometry under one operating condition may negatively affect the objective performance under different operating conditions. Considering the dynamic operation of the motor to be optimized ensured a balanced objective improvement performance across all operating points guaranteeing the solution produced by the non-dominated adaptive restart GA is the optimal rotor bar geometry for all operating conditions. Dynamic optimization presents a number of challenges as it introduces a number of new performance points associated with each rotor bar design which need to be balanced between operating points and between multiple performance objectives in order to evaluate the total fitness of each individual without function bias. As the number of test operating points selected for optimization increases, the number of function evaluations also increases, causing longer run times and therefore, the number of test operating points selected must be mindfully chosen. Significant operating points must be identified to refine the number of operating test points required to generate a fair representation of the operating range based on performance objectives.

5.2. Core Loss Prediction Under Dynamic Operating Conditions

To accurately simulate the performance objectives of a tractive IM, changes in the operating frequency and its effect on the magnetic loading represented by the flux density of the core must be considered. The core loss of induction machines corresponds to approximately 15% to 25% of its total losses when considering a combination of eddy current, hysteresis and excess losses [37], [117]–[119]. These losses are influenced by material properties such as the permeability and conductivity of the core and geometrical parameters such as the lamination thickness. The core loss is also directly influenced by the supply frequency and the flux density present during the current operating condition. Therefore, the relation between core loss, flux density and frequency must be taken into account in the equivalent circuit model. Conventionally, this relationship between core loss, frequency and flux density was modeled using core loss coefficients generated at several known frequencies and corresponding flux densities. During intermediate operating frequencies and flux densities, core loss coefficients of the closest known frequencies and flux densities are used influencing the accuracy of the simulated motor performance. To improve the accuracy of the permeance based equivalent circuit model further under dynamic operating conditions, a single objective adaptive restart GA is used to predict the core loss coefficients associated with a specific operating frequency and flux density. As a result of the increased accuracy of the permeance based equivalent circuit model, the solution quality of the global optimal solution is higher.

5.2.1. Core Loss Prediction Using Adaptive Restart Genetic Algorithm

A two-stage approach is taken to predict the core loss and respective core loss coefficients under any operating conditions to improve the accuracy of core loss modeling. An adaptive restart GA performs a surface fit in the first stage of the prediction algorithm to generate an equation relating the total core loss to various supply frequency and flux density levels [120]. The second stage uses the adaptive restart GA and curve fitting techniques to tune the core loss coefficients with respect to various supply frequencies. The results produced by this two-step prediction algorithm will then be applied to the permeance based equivalent circuit model at the test operating points selected for optimization. Starting from this set of reference core loss points taken at known frequencies and flux densities, the first stage of the process is to create a surface on which all test points are contained. The adaptive restart GA minimizes the error between the core loss surface and the reference points in the first stage, as seen in Fig. 5.1. This fitted surface and associated equation can then be used to predict the core loss at any arbitrary combination of frequency and flux density. The surface is represented by (29) where $P_{surf}(f_n, B_m)$ is the total core loss with respect to any arbitrary frequency, f_n, and flux densities, B_n, the coefficients α_1 to α_7 are combined to create the input variable vector tuned by the adaptive restart GA. The OF (30) to be minimized by the adaptive restart GA represents the root mean squared error of the reference core loss points P_{ref} and those calculated using (29), where (n) and (m) represent total reference frequencies and flux densities, respectively.

$$P_{surf}(f_n, B_m) = \alpha_1 f_n B_m{}^{\alpha_2} + \alpha_3 f_n{}^2 B_m{}^2 (1 + \alpha_4 B_m{}^{\alpha_5}) + \alpha_6 f_n{}^{1.5} B_m{}^{1.5} + \alpha_7 \quad (29)$$

$$\varepsilon_{rsm} = \sqrt{\frac{\sum_n \sum_m (P_{surf}(f_n, B_m) - P_{ref}(f_n, B_m))^2}{n \cdot m}} \quad (30)$$

78
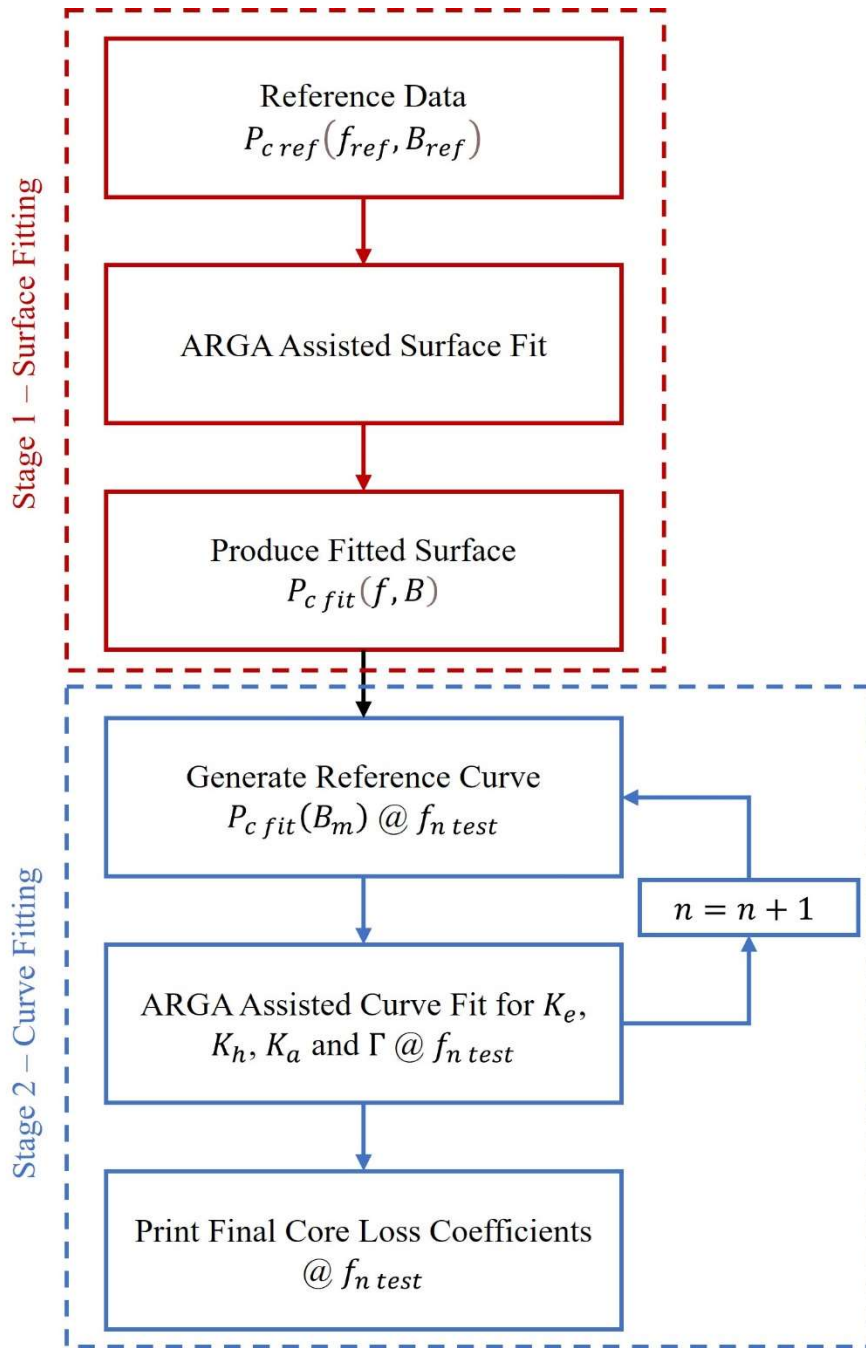
Fig. 5.1. The iterative flow of the two-stage core loss prediction method under dynamic operating conditions using a single objective adaptive restart GA.

When the adaptive restart GA converges producing optimal coefficients for (29), the algorithm moves into stage two. Specific test frequencies are selected that correspond to significant operating points that fall into frequencies not represented by the reference frequencies. At each of these test frequencies, several core loss points are taken at varying

flux densities using the fitted surface. These new test points will be used as a reference for a curve fit performed at this stage. The core loss coefficients K_a, K_h, K_e and Γ in (31) make up the input variable vector to be tuned by the adaptive restart GA. Once one set of core loss coefficients has been determined, the algorithm moves to the next test frequency generating new sets of coefficients that corresponding to test frequencies.

$$P_{curve}(f_{n\,test}, B_m) = K_h f_{n\,test} B_m{}^{\Gamma} + K_e f_{n\,test}{}^2 B_m{}^2 + K_a f_{n\,test}{}^{1.5} B_m{}^{1.5} \qquad (31)$$

The significance of this approach is through generating a specific set of core loss coefficients at each test frequency, the permeance based equivalent circuit model is capable of accurately consider dynamic operating coefficients Improving the solution quality of the global optimal design.

5.2.2. Adaptive Restart Genetic Algorithm Performance

In stage one of the prediction algorithm, the final fitted surface evaluated over a wide range of operating frequencies and flux densities is depicted in Fig. 5.2(a). The reference points are depicted on the surface showing a close correlation between the core loss at reference points and the predicted core loss using fitted (29). The adaptive restart GA was able to minimize the total RMS error at all reference points to 0.9576 W producing a combination of coefficients α_1 to α_7 with the maximum error of 3.0647 W at one operating point. The error response surface depicts the true error in watts between the reference and calculated core loss at each reference frequency and flux density after the first stage of the prediction algorithm is shown in Fig. 5.2(b). The accuracy of the fitted equation generated by stage one of the algorithm is essential to the prediction of core loss coefficients at desired operating points the fitted equation is used to calculate the predicted

80
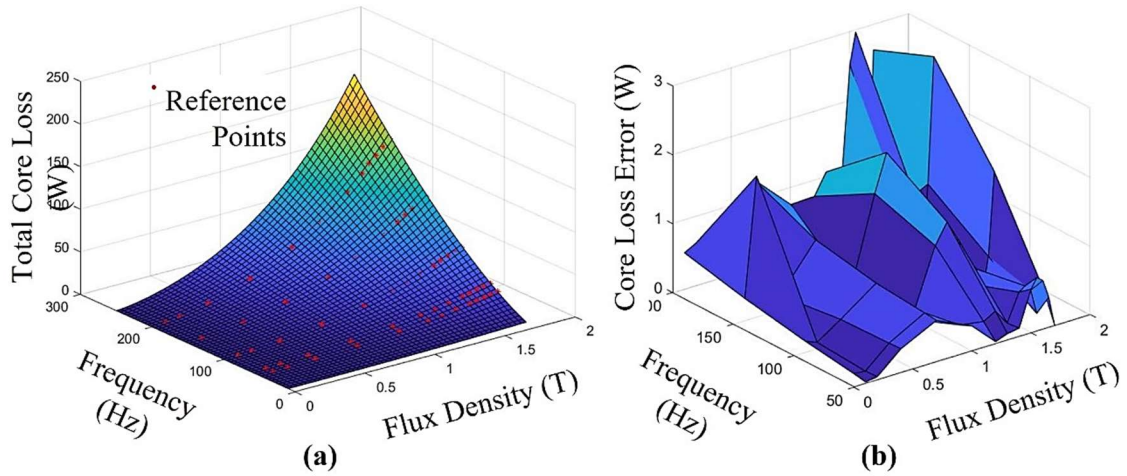
Fig. 5.2. Results of stage one of the core loss prediction is visualized. (a) Depicts fitted surface created during stage one of core loss prediction algorithm with respect to test points in red. (b) Depicts the error between the reference and calculated core loss.

core loss at desired operating points which can then be used as a reference by the adaptive restart GA during the second stage. Fig. 5.3(a) depicts the test points in red and the fitted curve generated by the adaptive restart GA at each respective operating frequency. The average RMS error across all test frequencies was minimized to 0.1738 W, with the maximum error at any operating point being 0.3632 W, as seen from the error response curves in Fig. 5.3(b). The algorithm converges once the function tolerance is reached,
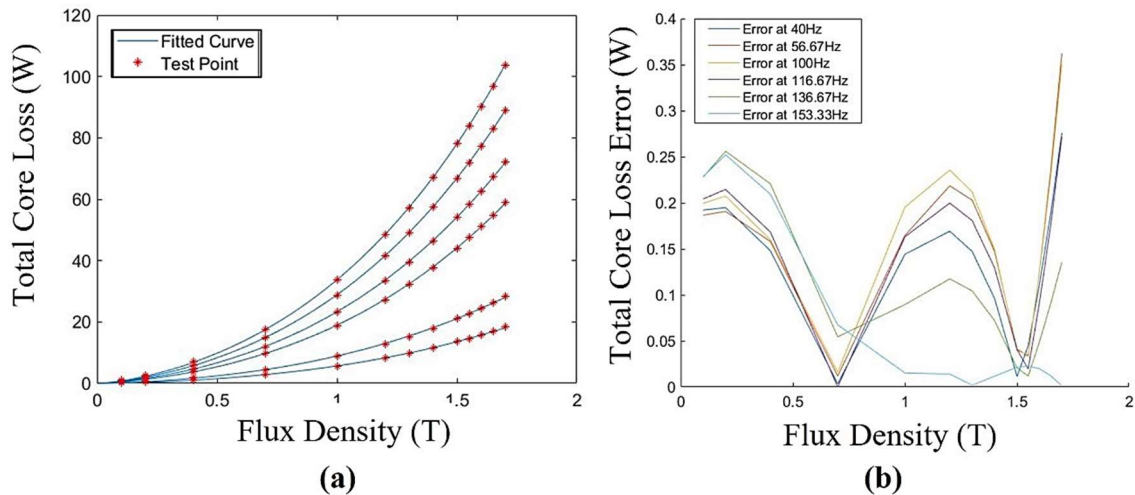
Fig. 5.3. Results of stage two of the core loss prediction algorithm. (a) Depicts fitted curves of core loss prediction algorithm with respect to test points in red. (b) Depicts the error between the reference and calculated core loss of each curve.

81

displaying the core loss coefficients K_a, K_h, K_e and Γ that correspond to each operating frequency, allowing these coefficients to be considered as variable with respect to the supply frequency and flux density, enhancing the capability the permeance based equivalent circuit model to predict the performance under dynamic conditions.

5.3. Considering Dynamic Operation Through Drive Cycle Based Testing

To analyze the dynamic performance of any tractive vehicle under true road conditions, common road test conditions must be established, capturing the speed, distance and duration of the road test, ensuring an equal comparison between vehicle performance results can be made. For this reason, common speed profiles called drive-cycles have been created to represent the speed profile of the test vehicle over the total test duration [121]. As a result of different traffic and vehicle laws in different countries around the world, the selected drive cycle must be based on the specific application of the vehicle. The United States commonly utilize the FTP-75 drive cycle representing urban driving conditions with frequent stops and low to moderate speeds while including two high speed sections simulating highway driving. To simulate exclusively high-speed highway driving conditions, the highway fuel economy test cycle (HWFET) to determine the fuel consumption of combustion engines or the energy consumption in the case of EVs. To normalize a drive cycle across all countries, the global harmonized drive cycles (WLTC) were created. Three classes defined by the vehicles power to mass ratio were defined to unify the results produced by dynamic vehicle simulation. The WLTC Class 3 drive cycle shown in Fig. 5.4 may be used to simulate a tractive EV found in the North American and European markets. The WLTC Class three drive cycle incorporates two different urban driving sections, a rural driving section and one high speed highway section to encompass

82
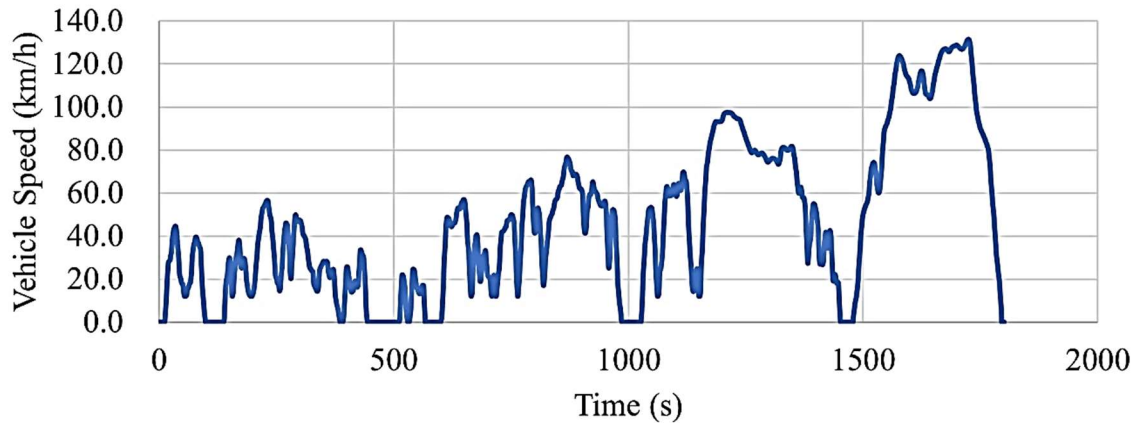
Fig. 5.4. The speed profile of the WLTC Class 3 drive cycle is shown over the total cycle time.

all operating ranges encountered by the vehicle under real world conditions. To segregate urban, rural and highway-based drive cycles, a statistical study called the Artemis Project performed in Europe created the three drive cycle configurations. One Artemis Cycle represents urban, rural and highway driving respectively and offers a more detailed analysis of one specific driving condition. The total distance covered, total duration and average speed of each of these drive cycles are displayed in Table 5.1, providing an overview of the average driving conditions encountered during each respective cycle. To measure the

TABLE 5.1

OVERVIEW OF VARIOUS DRIVE CYCLES

Drive Cycle	Total Distance Traveled (km)	Total Drive Cycle Time (s)	Average Vehicle Speed (km/h)
FTP-75	23.262	1800	46.5
WLTC	17.77	1874	34.1
Artemis Urban	4.87	993	17.6
Artemis Rural	17.272	1082	57.5
Artemis Highway 150	29.545	1068	99.6
Artemis Highway 130	28.735	1068	96.9

performance of a tractive IM prototype under controlled lab conditions with respect to dynamic performance, expensive experimental test equipment including a dynamometer and power electronic control modules for both the tractive IM and the dynamometer is required to perform drive cycle based experimental testing [122]–[124]. Depending on the purpose of the drive cycle test, and the measurement equipment used during the duration of the test, the results produced by experimental drive cycle testing can be used to evaluate and validate motor models, control algorithms and vehicle dynamics models as well as identify significant operating points for design optimization purposes. The IM is considered the device under test (DUT), which is aligned opposite the dynamometer and coupled through a torque transducer, as seen in Fig. 5.5. The torque transducer measures the real torque applied on the shaft at any instance in time which is used by the torque-oriented control strategy of the dynamometer control module. An encoder measures the true rotor speed of the DUT, which is recorded and used by the speed-oriented control
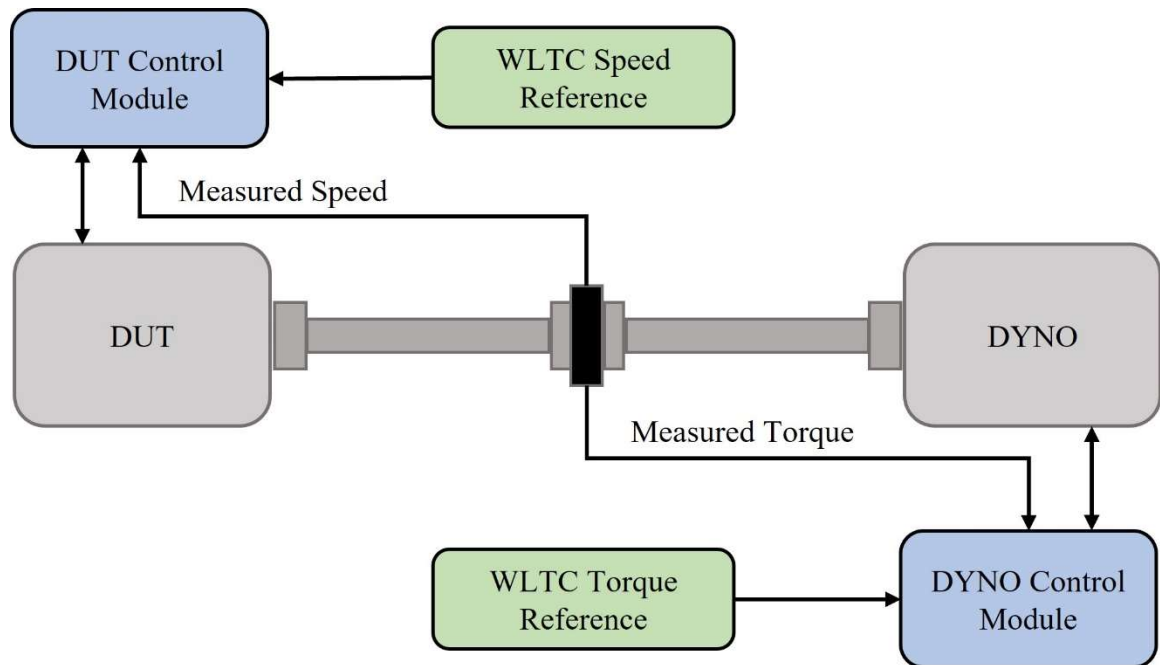
Fig. 5.5. The experimental test setup required to perform drive cycle testing of tractive IMs is depicted.

84

strategy of the DUT's control module. The dynamometer control algorithm measures the difference in the measured torque and the torque profile generated by a vehicle dynamics model with respect to the baseline IM in an attempt to maintain a minimum error over the course of the test, ensuring the WLTC Class 3 drive cycle profile is followed. The Speed oriented control strategy used to control the DUT works in a similar fashion using the speed profile of the WLTC Class 3 drive cycle as a reference [125]. The dynamometer imitates the load applied to the axel of the vehicle specified by the vehicle dynamic model-based drive cycle simulation. As the DUT's control strategy follows the speed profile of the WLTC Class 3, operating regions in which the vehicle experiences high dynamic resistive forces such as rapid acceleration or an inclined road, the dynamometer applies the equivalent resistive torque opposing the DUT's ability to maintain the reference speed, increasing the error between reference and actual speed prompting the control strategy of the DUT to increase the power injected into the motor. As a result of the extensive test setup and smaller size of the baseline IM, a vehicle dynamics model must be developed in order to allow for simulated drive cycle-based testing, which can then be experimentally validated at specific operating conditions determined by the simulated motor performance.

5.3.1. Electric Vehicle Dynamics Modeling

The vehicle dynamic model considers numerous vehicle specific parameters simulating the resistive forces acting on the vehicle during the simulated drive cycle [126]. These resistive forces must be matched by the drive system of the vehicle in order to maintain the current velocity and acceleration of the vehicle, therefore, representing the load on the wheels over the course of the WLTC Class three cycle. To derive the load demanded by the vehicle with respect the tractive IM, several vehicle specific parameters

85

must be considered. The tire radius, drive train configuration, and torque split ratio of the test vehicle are used to define how much of the total vehicle load is distributed to the motor being analyzed. Considering a simple vehicle dynamic model depicted in figure 5.6. [127], [128], modeling the vehicle weight, G_{curb}, with respect to the road gradient, α, the vehicles current speed, v, and acceleration, a. Four dynamic resistive forces oppose the tractive force produced by vehicles motor at the wheels. Equation (32) is used to determine the Rolling Resistance, L_r, which is a result of tire deformation at the contact point with the road resisting forward motion.

$$L_r = K_{roll}\, G_{curb}\, \cos(\alpha) \tag{32}$$

The rolling resistance depends on the total weight of the vehicle, the slope of the road and the rolling resistance coefficient, K_{roll}, which depends on the road quality, tire pressure and vehicle speed. The aerodynamic resistance, L_a, depends on the frontal cross-sectional area of the vehicle, SA, vehicle speed, air density, ρ, and the crag coefficient c_{drag} in (33).

$$L_a = \frac{1}{2}\,\rho c_{drag} \cdot SA \cdot v^2 \tag{33}$$
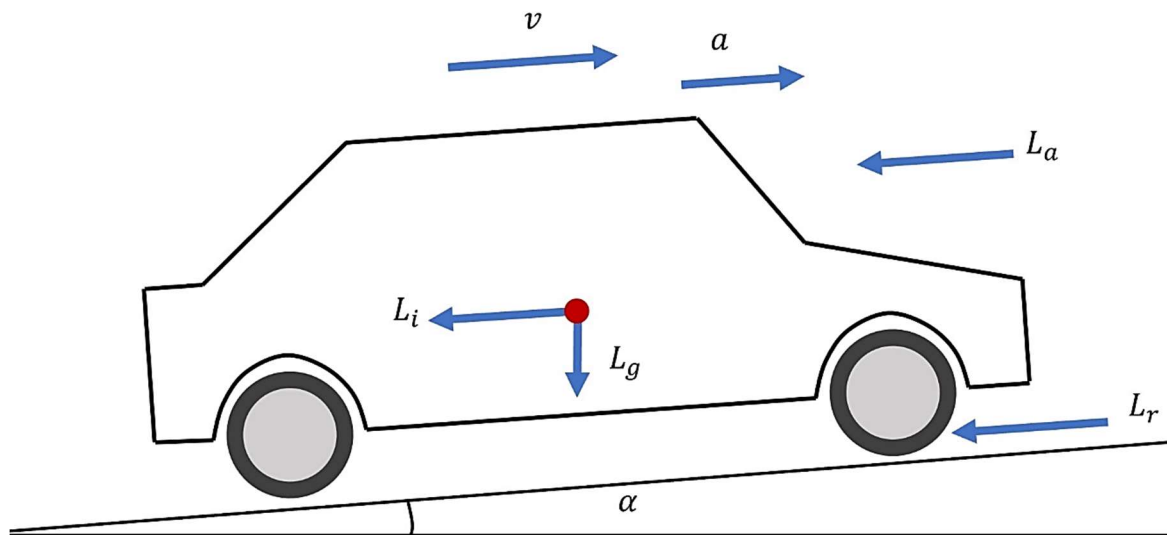
Fig. 5.6. Vehicle dynamics model used to determine the torque requirements of the WLTC Class 3 drive cycle.

The drag coefficient depends on a number of factors, including elevation, vehicle shape, weather conditions and other dynamic resistive effects. To model the increased load on the vehicle when travelling uphill, the gradient resistance, L_g, is given by (34), which depends on the vehicles weight and the slope of the road over the course of the drive cycle.

$$L_g = G_{curb} \sin(\alpha) \tag{34}$$

Lastly, the effect of inertial forces that represent the force required to accelerate an object with respect to its mass is calculated using (35).

$$L_i = \frac{G_{curb}}{g} \cdot a \tag{35}$$

The mass of the vehicle is calculated by dividing the total vehicle weight by the force of gravity, g, and is multiplied by the current acceleration of the vehicle to determine the inertial resistance, L_i. When summed together, these four resistive forces determine the load profile demanded by the WLTC Class 3 with respect to the wheels of the vehicle. To determine the load profile of the baseline tractive IM, the load is split with respect to the torque split ratio of the EV and then converted to the load on the axel of the vehicle determining the baseline tractive IM load profile demanded by the WLTC Class 3. Finally, the energy consumption associated with each operating point can be derived from the power required by the tractive IM, which can be calculated by multiplying the torque and speed at ever operating point. The complexity of the vehicle dynamics model depends on the application and purpose of the simulation and can integrate control algorithms and IM simulations. However, for the requirements of this application, a simple vehicle dynamics model is sufficient.

5.3.2. Simulated Dynamic Operating Points Over WLTC Class 3 Drive Cycle

The use of drive cycle simulation through a vehicle dynamics model can be used to analyze many aspects of vehicle level as well as motor level performance depending on the accuracy and complexity of the dynamic model, motor simulation and control algorithm used to evaluate the drive cycle. Since the objective of this dive cycle simulation is to determine the associated load torque profile with respect to the speed profile given by the WLTC Class 3 drive cycle and the associated energy consumed at each operating point, the drive cycle simulation does not require any control algorithm or electric motor simulation. Instead, the speed, $v(t)$, given by the drive cycle with respect to time, t, is input to the conventional vehicle dynamics model as seen in Fig. 5.7. The current acceleration required to calculate the inertial resistance of the vehicle is calculated, as seen in (36), using the change in velocity from the current and previous time step over time change.

$$a(t) = \frac{v(t) - v(t - t_{step})}{t_{step}} \tag{36}$$

The vehicle dynamics model calculates the total resistive load acting on the vehicle at the given time and converts the vehicle torque to the axle torque with respect to the torque split ratio of the EV. The current speed and torque are multiplied together to find the current power to plot the torque, and energy consumption is plotted against time.
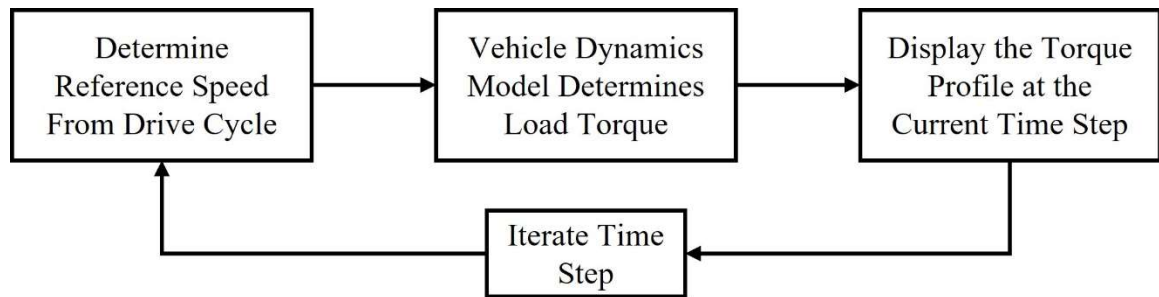
Fig. 5.7. Iterative flow of drive cycle simulation to determine the torque profile with respect to the vehicle.

The algorithm iterates, updating the drive cycle time by time step, t_{step}, which is determined by the resolution setting the quality of the results generated by the simulation. When all speed points have been simulated and the maximum time has been reached, full speed and torque profiles with respect to the WLTC Class 3 drive cycle are produced, as seen in Fig. 5.8. The entire torque speed range encompassing all operating points generated over the duration of the WLTC Class 3 drive cycle and their corresponding energy consumption is depicted in Fig. 5.9. The torque and energy consumption profiles generated through this simple drive cycle simulation can be used to determine significant operating points for design optimization purposes as well as experimentally validated by the baseline prototype tractive IM. The number of operating points collected during the drive cycle test represents a large set of numbers, making it impossible to optimize on all operating points. A strategy to reduce the number of operating points while identifying the most significant operating points for dynamic optimization must be developed.
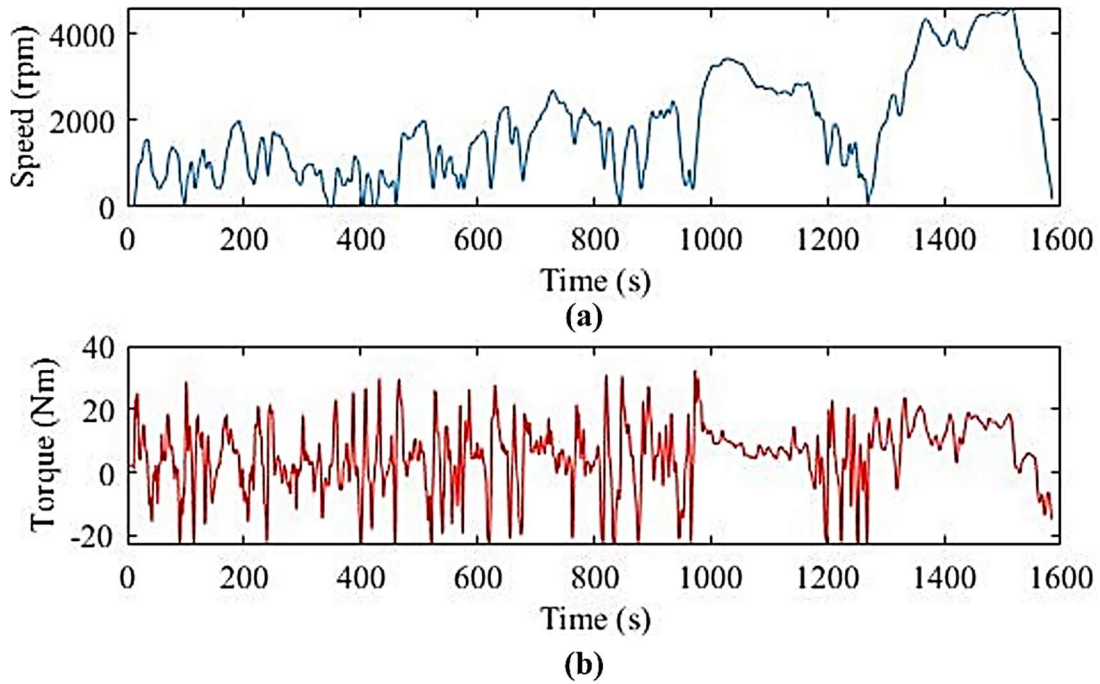
Fig. 5.8. Results of WLTC drive cycle simulation. (a) Depicts the rotor speed profile of the simulated baseline IM. (b) The resulting load torque profile over the WLTC drive cycle.
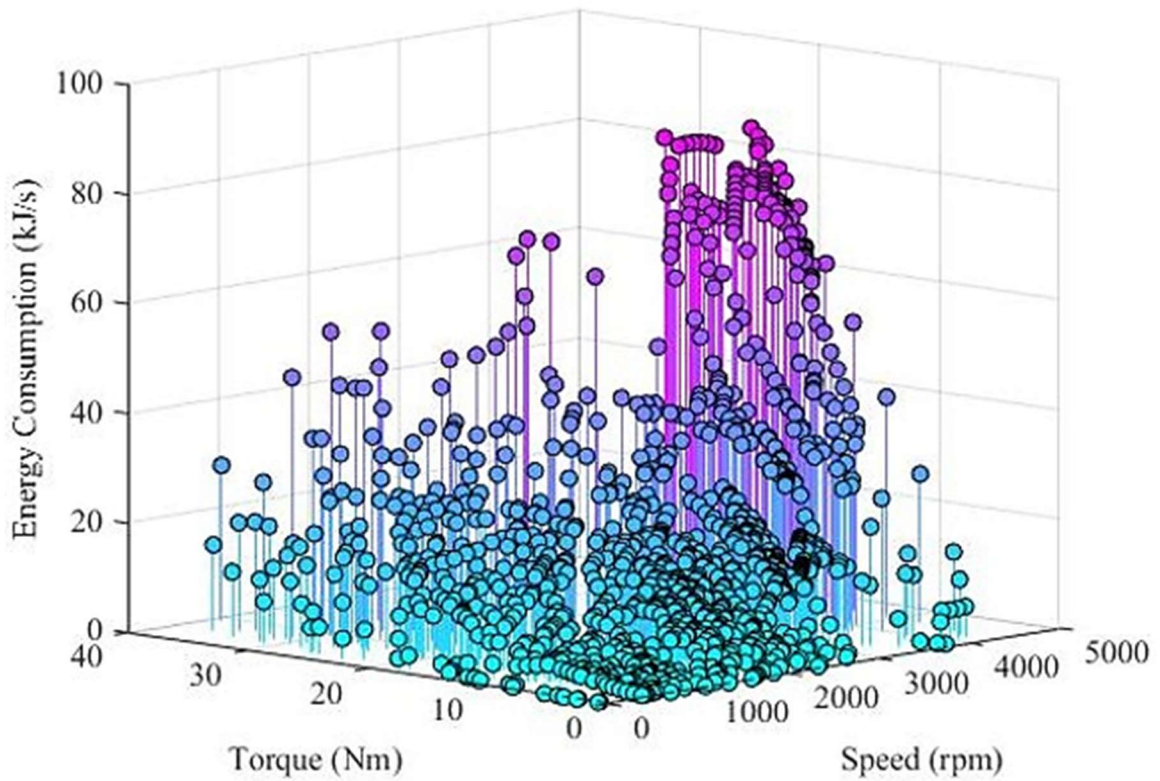
Fig. 5.9. The torque-speed profile generated over the WTLC drive cycle simulation and the associated energy consumption at each operating point.

90

5.4. Operating Point Reduction Through Energy Center of Gravity Method

The data sets collected by drive cycle-based simulation and experimental testing contain extremely large sets of operating points with respect to the torque and speed of the tractive IM. Therefore, a data processing method must be developed to represent the average operating point with respect to a subregion of the total operating range [129]. The operating points contained within each subregion are considered a cluster and are then represented by a single average operating point called the centroid. The number of centroids produced is determined by the number of subregions that represent the entire operating range. The simplest method to generate the centroid is through calculating the mean torque and speed of all operating points contained in the cluster. Although this method provides the true mean operating point to represent the cluster, the purpose of the WLTC Class 3 drive cycle simulation and experimental testing of baseline tractive IM was to identify operating points with high energy consumption for use in targeted, dynamic optimization [130]–[133]. The use of Energy Center of Gravity Clustering considers the energy consumption at each operating point while calculating the centroid of each cluster, ensuring the centroids produced to provide a better representation of the subregion with respect to areas of high energy consumption than the true mean (37) is used to calculate the total energy consumption, E_{c_r}, of each respective cluster, r, using the energy consumption, E_{ir} and velocity, v_{ir}, of every individual within the cluster denoted by i.

$$E_{c_r} = \sum_{i=1,2,3...}^{N_i} E_{ir} v_{ir} \tag{37}$$

When the total energy of the cluster is known, (38) and (39) calculate the weighted centroid speed, v_{c_r} and torque, T_{c_r}, respectively.

$$v_{c_r} = \frac{1}{E_{c_r}} \sum_{i=1,2,3...}^{N_i} E_{ir} v_{ir} \tag{38}$$

91

$$T_{C_r} = \frac{1}{E_{c_r}} \Sigma_{i=1,2,3...}^{N_i} E_{ir} T_{ir} \hspace{3cm} (39)$$

When applied to the operating points produced by the WLTC Class 3 drive cycle simulation, the total operating region is split into nine equal sub regions creating nine clusters of operating points to be analyzed with respect to the energy consumption of each point. The Energy Center of Gravity Clustering algorithm iterates through all subregions resulting in the centroids depicted in Fig. 5.10, among the sub-region each centroid represents. A comparison between the centroid produced by the energy center of gravity clustering algorithm and the true mean can be drawn from Fig. 5.11, demonstrating a significant difference between centroid locations of with respect to the torque-speed range. The energy consumption of each cluster's centroid listed in Table 5.2 clearly indicates that the centroid location produced by the energy center of gravity clustering algorithm was selected based on higher energy consumption. The significance of using energy center of gravity clustering to represent operating points of higher energy consumption as they carry
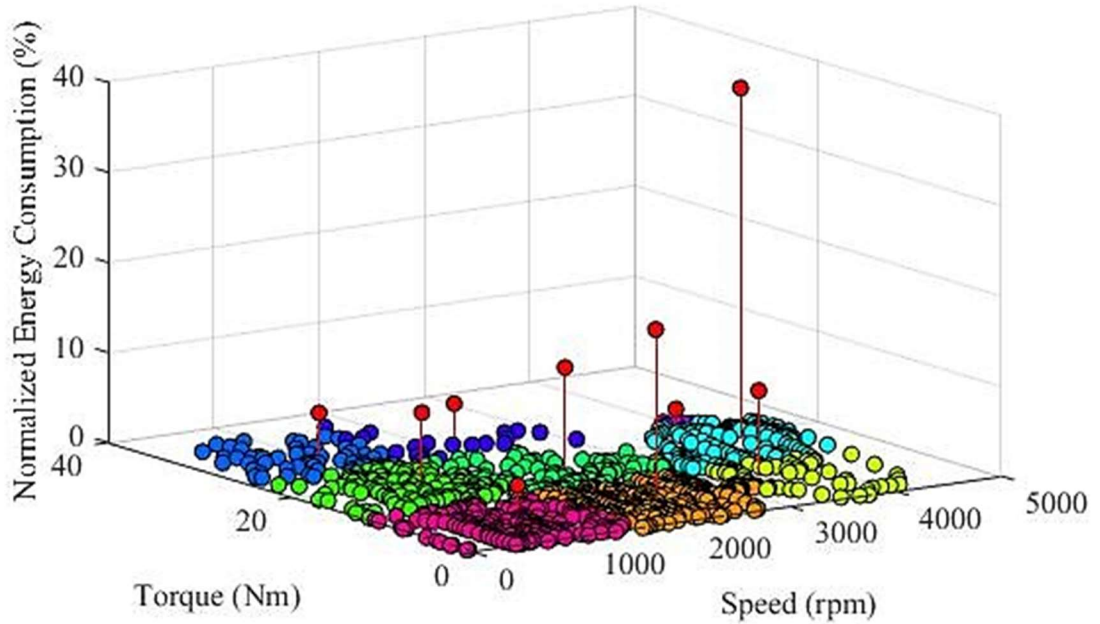
Fig. 5.10. The centroid of each sub-region is highlighted in red among the measured operating points from the WLTC drive cycle test.

92
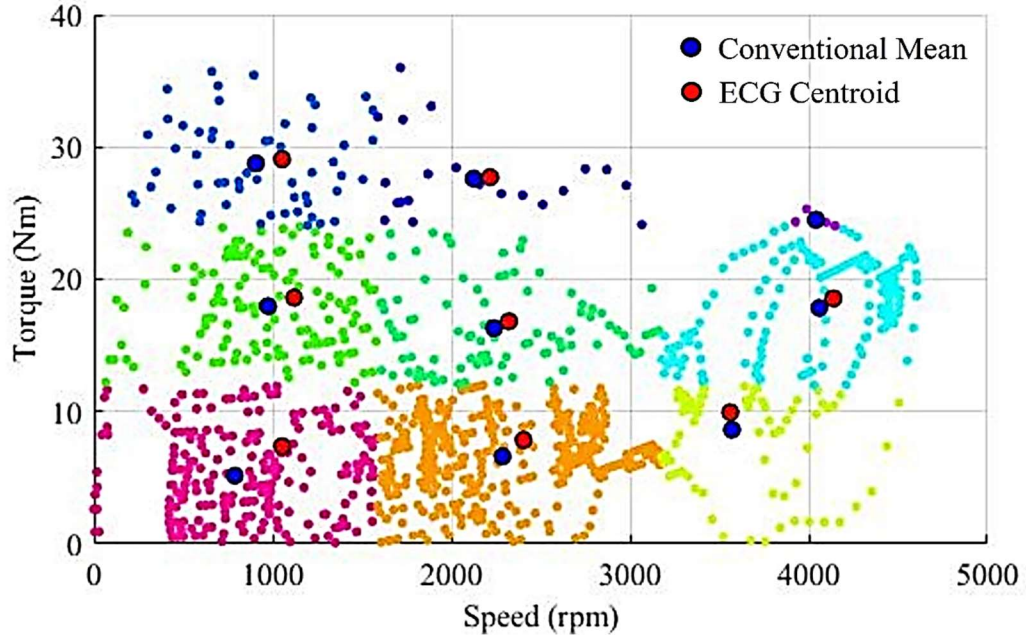
Fig. 5.11. The centroid position on the torque-speed sub-region with respect to the conventional mean demonstrates the effect of energy center of gravity clustering.

TABLE 5.2

CONVENTIONAL MEAN AND ENERGY CENTER OF GRAVITY CLUSTERING

Clustering Method	Conventional Mean		Energy Center of Gravity Centroid		Normalized Energy
Sub-Region	Mean Torque	Mean Speed	Centroid Torque	Centroid Speed	(%)
1	789.1866	5.1581	1053.4309	7.3832	3.4568
2	2286.6940	6.6177	2403.9938	7.8528	18.2779
3	3570.7375	8.6276	3561.3429	9.9367	8.8947
4	974.8661	17.9718	1120.3805	18.6103	7.9422
5	2240.0364	16.3047	2322.4715	16.8170	11.4676
6	4059.8764	17.8372	4138.2247	18.5539	38.8926
7	906.6508	28.7649	1053.5298	29.0700	4.8411
8	2125.7289	27.6165	2217.6596	27.7165	4.3020
9	4040.5779	24.5042	4041.3998	24.5075	1.5873

more significance when optimizing the energy losses of baseline tractive IM. The dynamic rotor bar optimization will be carried out with respect to the performance of the baseline IM on all 9 operating points produced, ensuring the full scope of possible operating conditions over the WLTC Class 3 drive cycle is considered.

5.5. Optimization Considering Multiple Operating Points

To optimize the rotor bar geometry with respect to dynamic operating conditions, each possible rotor bar represented by an individual must be evaluated at all 9 operating conditions with respect to both the output torque and the losses. To avoid overwhelming the GA by passing a total of 18 OF scores for each individual within the population or adding unnecessary steps by optimizing each operating point individually, modifications need to be made to the evaluation of the PECM and the OFs of the non-dominated adaptive restart GA to allow for dynamic optimization through (40) and (41).

$$OF_{tor_i}(gen) = \sum_{r=1,2,3...}^{N_r}(E_c) \times \left(1 - \tanh\left(K_{tor} \times \left[\frac{T_{out_{ir}}(gen) - T_{best_r}(gen)}{T_{base_r}(gen)}\right]\right)\right) \quad (40)$$

$$OF_{loss_i}(gen) = \sum_{r=1,2,3...}^{N_r}(E_c) \times \left(1 + \tanh\left(K_{tor} \times \left[\frac{P_{loss_{ir}}(gen) - P_{best_r}(gen)}{P_{base_r}(gen)}\right]\right)\right) \quad (41)$$

Rather than passing the torque and loss performance under each operating condition as its own objective score, the performance with respect to the torque, $T_{out_{ir}}$, produced by an individual, i, under each operating conditions, r, is assigned a torque objective fitness score, OF_{tor_i}, and a loss objective fitness is assigned as OF_{loss_i}. The use of hyperbolic tangent based OFs ensure an equal contribution to the overall objective fitness with respect to each operating point is maintained. The contribution to the objective fitness at each operating point is then scaled by the normalized energy consumption, E_{c_r}, under the current operating conditions produced by the energy center of gravity clustering algorithm. By

94

applying weights with respect to energy consumption, the objective fitness will place a higher value on individuals that result in objective improvements under operating conditions that demand higher energy consumption. The torque and loss objective fitness scores are then passed as the two objective scores to the non-dominated adaptive restart GA, which are then combined to produce the total fitness of the individual. The iterative performance calculation carried out under every operating condition by the permeance based equivalent circuit model add a significant number of computations to the algorithm resulting in longer run times. The benefit of targeted dynamic optimization justifies the increased run time as the global optimal rotor bar design produced represents an improved design with respect to the base design across every significant operating condition. The proposed non-dominated adaptive restart GA is now capable of geometric rotor bar optimization for improved torque and minimized losses considering a dynamic operation.

CHAPTER 6   Tractive Induction Motor Rotor Bar Optimization Using a Novel Non-dominated Adaptive Restart Genetic Algorithm Considering Dynamic Operating Conditions

6.1. Novel Adaptive Restart Genetic Algorithm Performance

The adaptive restart GA has been modified to improve the algorithm's robustness against stalling and local solutions while improving the overall confidence and quality of the final optimal solution produced. The PECM is capable of rapidly predicting the performance at specifically chosen operating points and relay the weighted objective score through novel hyperbolic tangent based objective functions ensuring a balanced improvement with respect to both objectives. Through limit reduction, the overall runtime of the algorithm is maintained at considerably low levels while the solution quality has been further enhanced as the search space is more thoroughly explored each restart iteration. The non-dominated adaptive restart GA can now be implemented to optimize the rotor bar of the baseline IM for improved output torque and reduced total losses at every operating point identified by the energy center of gravity clustering of the WLTC Class 3 drive cycle-based torque-speed profile of the baseline IM. The adaptive restart GA parameters are listed in Table 6.1, the restart tolerance and function tolerance have both been set to $10^{-4,}$ and the minimum and the maximum number of restarts are two and ten, respectively. The GA parameters limit each run to 500 generations of a population of 200 individuals while allowing a maximum number of 150 stalls to analyze the effect of restart parameters in improving the OA's resistance to excessive stalling. The algorithm is limited to a 300 second maximum run time to ensure the optimal rotor bar is produced quickly

96

TABLE 6.1

ADAPTIVE RESTART GENETIC ALGORITHM PARAMETERS AND TOLERANCES

GA Parameters		Restart Parameters	
Parameter	**Value**	**Parameter**	**Value**
Maximum Generations	500	**Maximum Restart Iterations**	10
Maximum Stall Generations	150	**Minimum Restart Iterations**	2
Function Tolerance	10^{-4}	**Restart Tolerance**	10^{-4}
Population Size	200	**Reduction Factor**	10%
Pareto Fraction	50%	**Maximum Run Time (s)**	300
Crossover Rate	20%		
Mutation Rate	10%		

while maintaining a high solution quality. The pareto fraction represents the number of

high scoring individuals of the population are kept at the end of each iteration, in this case.

The non-dominated adaptive restart GA converged to a global optimal solution after seven

restart iterations, during which an average of 356 generations were evaluated during each

iteration before the function tolerance was reached. The total run time of the adaptive

TABLE 6.2

ADAPTIVE RESTART GENETIC ALGORITHM PERFORMANCE

Adaptive Restart GA Performance			
Performance Parameter	**Value**	**Performance Parameter**	**Value**
Total Number of Restarts	7	**Centroid Output Torque OF Score**	0.279
Algorithm Run Time (s)	98.91	**Centroid Total Loss OF Score**	0.483
Average Number of Generations	357	**Total Centroid OF Score**	0.742
Maximum Number of Stall Generations	32		

restart GA was 98.91 seconds which is well below the maximum run time, ensuring a rapid optimal design. Table 6.2 indicates that the maximum number of stall generations in which no improvement in objective function score is noticed, was only 32 generations which indicates the adaptive restart GA is incredibly resistant to stalling despite a high pareto fraction and maximum stall generation limit. From the objective function scores of the torque and losses after converging. The loss objective score of 0.483 is very close to the baseline losses of 0.5, indicating that the losses were only slightly reduced. This does not indicate the presence of a dominant objective, however, as there is no bias between objectives. The torque produced by the optimal solution increased by such a large amount that despite only a small reduction in the loss objective score, the optimal rotor bar produced saw a greater reduction in total objective function score and was therefore selected as the global solution. The local limits with respect to the centroid evolution over the seven restart iterations is depicted in Fig. 6.1 with respect to one input variable. Through
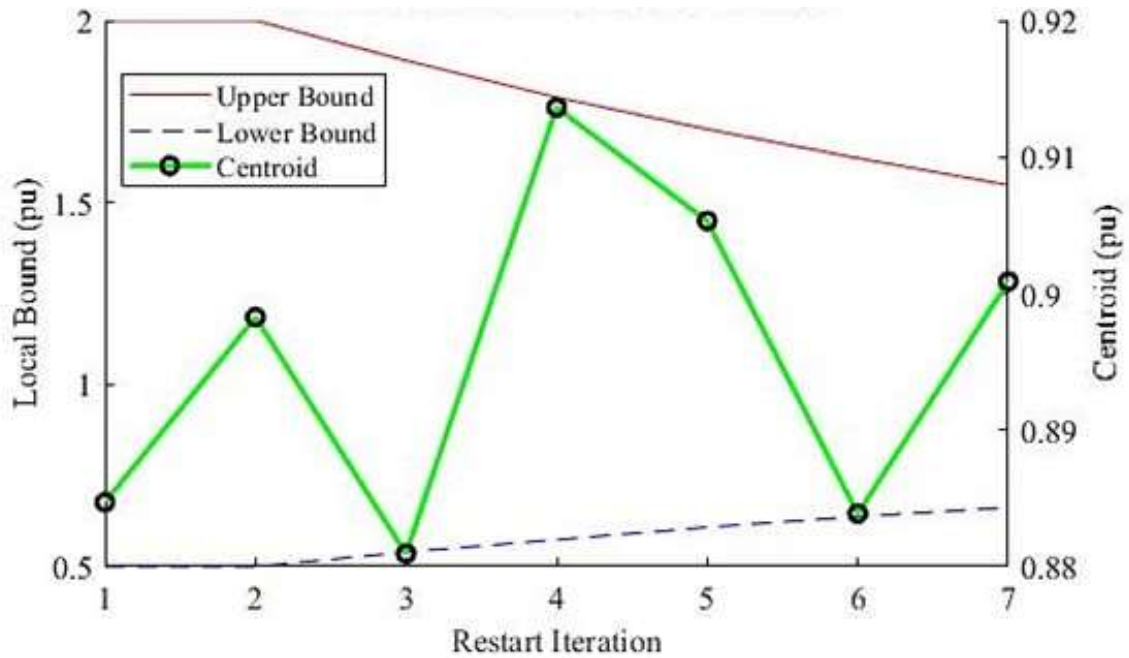
Fig. 6.1. The local upper and lower bound with respect to one input variable and centroid evolution with respect to each restart iteration.

reducing the search space each iteration, the population becomes crowded in a more focused area allowing for a refined search and improving the overall solution quality of the global optimal rotor bar geometry produced. It should be noted that until the minimum number of restart iterations is reached, the local bounds remain at initial global bounds. This ensures the initial iterations are allowed to explore the largest possible search space. The torque and loss performance of the best individual across all cumulative generations is depicted in Fig. 6.2 and shows the spike in both objective targets is seen when the algorithm resets and the population is once again randomly initialized. The normalized torque and loss performance is based on the performance of the optimal rotor bar as a per unit value of the base design and the normalized energy consumption of each sub-region. The local optimal set of input variables, assigned as the centroid at each restart iteration,
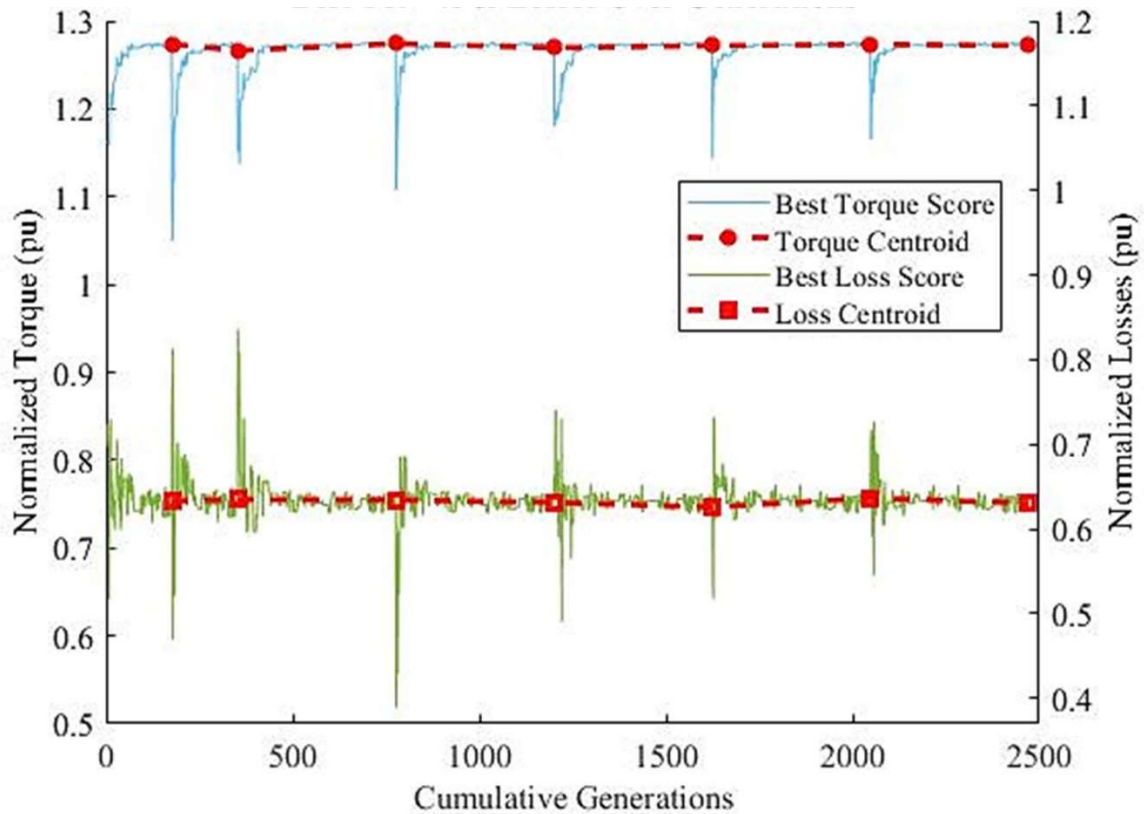
Fig. 6.2. Normalized torque and losses of the best-known solution at each generation across all restart iterations and the respective centroids.

represents the current best-known solution and is seen to change slightly between restart iterations as better solutions are found. The input variables may greatly vary between restart iterations. However, the torque and loss performance must remain competitive, and therefore only small increases in centroid performance occur. The centroid produced by the seventh restart iteration represents the global optimal solution and optimal rotor bar geometry which must be validated and compared to the baseline rotor bar.

The proposed novel, non-dominated adaptive restart GA is capable of rapid, unbiased, multi-objective optimization, as seen in the results presented in this section. The algorithm was able to resist stalling, while considering dynamic operating conditions, quickly resulting in an optimal rotor bar geometry with greater torque performance and a considerable reduction in total losses. From the results presented in this section, it can be confirmed that the algorithm level objectives are met by the proposed method. The following section will analyze the optimal bar produced, validating and comparing the optimized rotor bar performance to that of the base design.

6.2. Comparison of Optimal Rotor Bar Geometry and Validation

To analyze the solution quality and effectiveness of the proposed adaptive restart GA, the optimal rotor bar produced must be compared to that of the baseline design. Some preliminary conclusions were drawn based on the objective function scores of the centroid, which through the validation and evaluation of the optimal rotor bar must be confirmed to achieve motor and vehicle level objectives. The optimal rotor bar depicted in figure 6.3 over the baseline bar geometry shows that the rotor bar has decreased in overall height and width, resulting in a lower cross-sectional area. The torque region at the top of the rotor bar had become elongated to produce a higher output torque causing higher losses at the

100
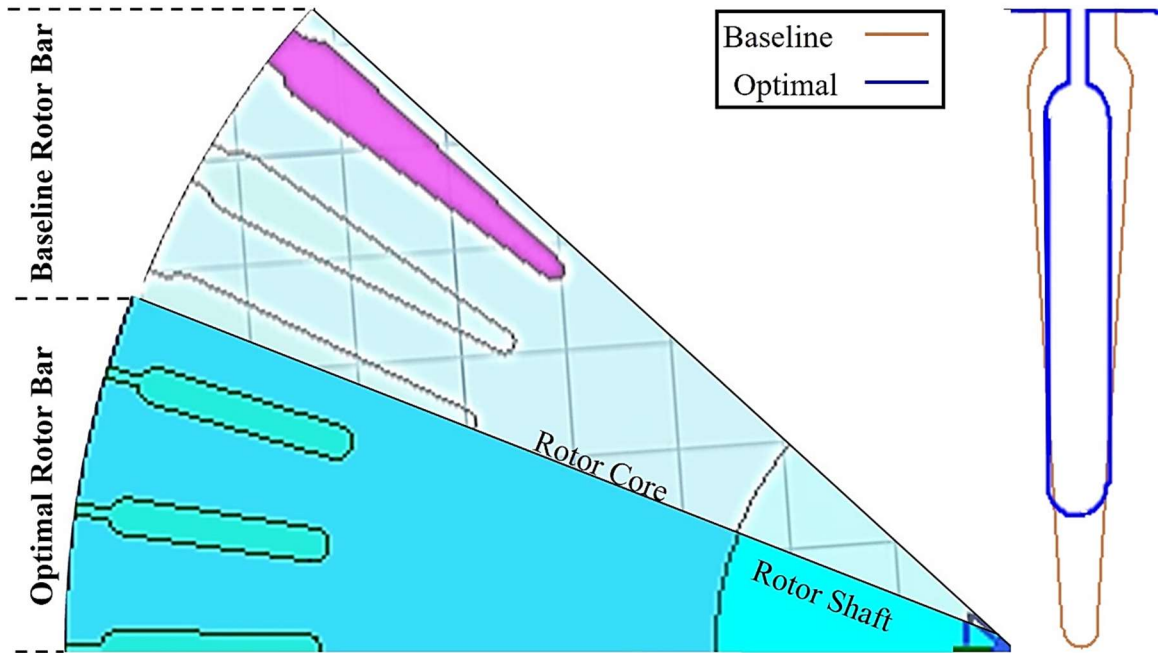
Fig. 6.3. A rotor section of both the baseline rotor and optimal rotor depicted the relative size of the rotor bara with respect to the rotor while an overlay compares the change in size and shape to one another.

tooth tops and the upper portion of the bar. However likely balanced out by the increased width in the lower portion of the bar. With the expected increase in torque and reduction in losses expected to bring an increase in efficiency and torque density, the optimal rotor bar will be evaluated under the same operating conditions measured during the experimental tests conducted on the baseline IM. This not only ensures a direct comparison between the baseline rotor bar performance and the optimal geometry produced by the proposed method, this also ensures different operating points than the significant operating points produced by the energy center of gravity method and used by the adaptive restart GA. Comparing the performance on a different set of operating points ensures that the optimal rotor bar geometry produced, in fact, represents the global optimal solution across all operating conditions experienced by the baseline tractive IM both in the constant torque and power regions. Fig. 6.4 plots the measured torque, losses and efficiency of the baseline IM against the performance of the optimal rotor bar calculated using the PECM and FEA.

101
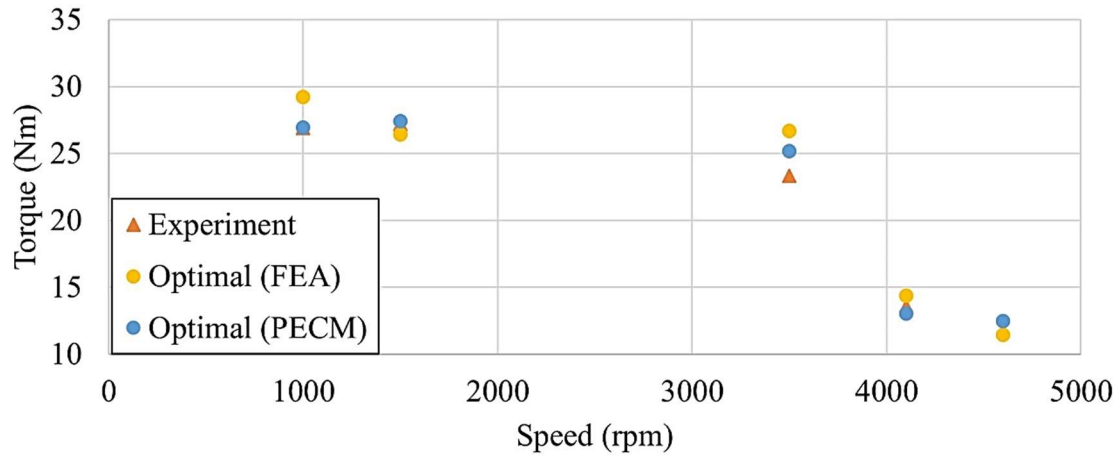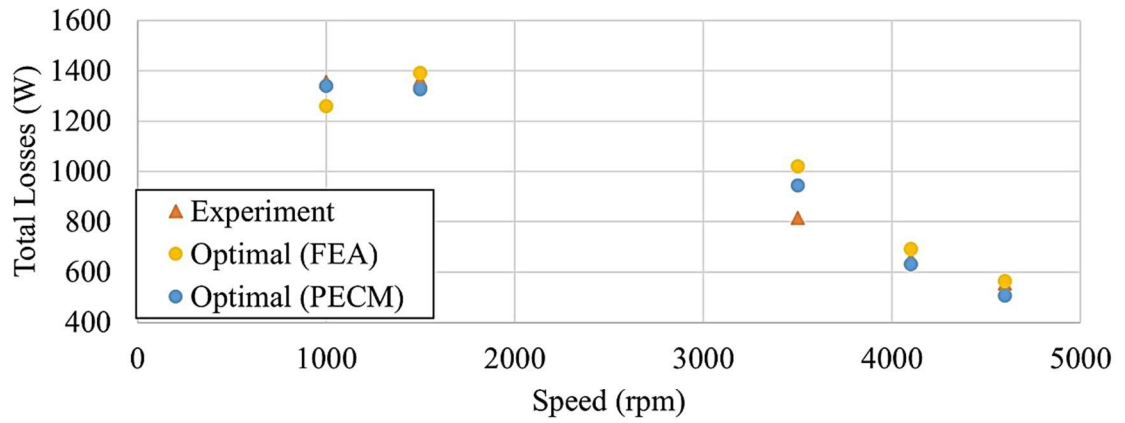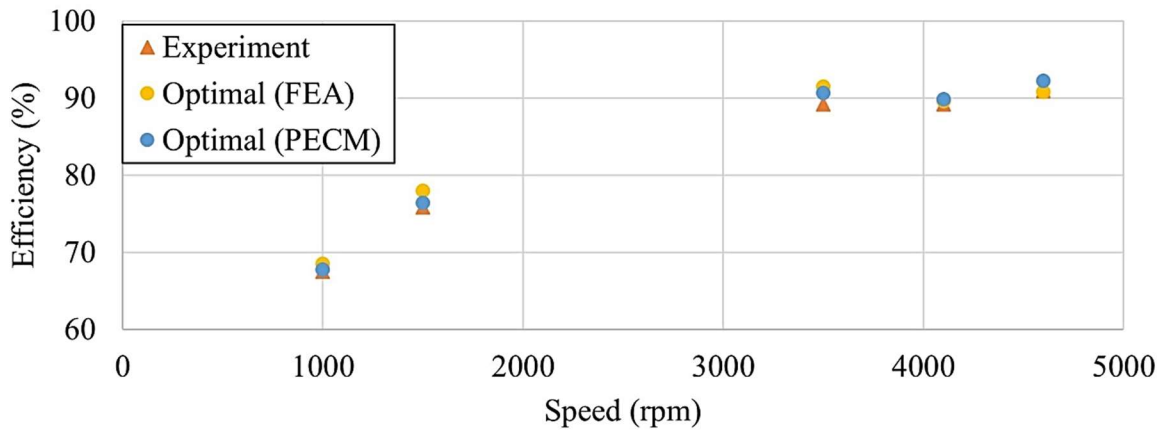
Fig. 6.4. Torque, total loss and operating efficiency validation on 5 test points of the optimal rotor bar produced by the novel, non-dominated adaptive restart GA. (a) Depicts the large torque improvement. (b) Validates the total losses produced by the optimized rotor IM. (c) Depicts the efficiency validation of the optimized rotor bar design.

The PECM was able to predict the torque with an average error of 7.16%, the total losses within an average error of 7.89% and the efficiency to 1.12% average error, which are consistent with the baseline validation and within acceptable margins. FEA also revealed that the even under high loading conditions, the flux density in the tooth tops was maintained below the maximum flux density of 1.7 T, satisfying the optimization problems constraint. The figure also indicates only small reductions in the losses while the torque is seen to have increased substantially at every operating test point compared to the measured performance of the baseline IM. The output torque and total losses of the baseline and optimal IM are displayed in Table 6.3. The output torque was increased at every operating test point by a minimum of 6% and an average of 7.5%, while the total losses were also successfully reduced at every operating point by an average of 0.5%. Although the losses were reduced by the desired 3%, the torque was increased by such a large factor, that the overall increase in output power while the total losses are similar, both the torque density and efficiency have been increased. As the weight of the IM has not changed significantly, the torque density can be assumed to also increase by a factor of 7.5%, while Table 6.4 displays the efficiency calculated at each operating point for the baseline and optimal design. The operating efficiency was also successfully increased by 1.3%.

The optimal rotor bar has been validated against FEA, and the performance improvement at every operating test point analyzed, it can be concluded that the optimal rotor bar produced by the proposed novel, non-dominated adaptive restart GA is capable of producing 7.5% higher output torque while offering 0.56% lower total losses resulting in an optimized IM with improved torque density and 1.3% higher operating efficiency achieving the motor, and vehicle level objectives.

TABLE 6.3

TORQUE AND LOSS PERFORMANCE OF BASELINE AND OPTIMAL ROTOR BAR

Baseline IM Performance		Optimized IM Performance		Performance Improvement	
Output Torque (Nm)	Total Losses (W)	Output Torque (Nm)	Total Losses (W)	Torque Increase	Total Loss Reduction
25.2191	1,346.2986	26.9349	1,339.8836	6.8036	-0.4765
25.5091	1,331.4606	27.4203	1,326.8101	7.4921	-0.3493
23.7204	955.5482	25.1636	944.7842	6.0843	-1.1265
11.9630	632.0332	13.0545	630.9877	9.1241	-0.1654
11.5548	510.5318	12.4846	507.2355	8.0469	-0.6457
25.2191	1,346.2986	26.9349	1,339.8836	6.8036	-0.4765
25.5091	1,331.4606	27.4203	1,326.8101	7.4921	-0.3493
		Average Change		**7.5102**	**-0.5527**

TABLE 6.4

THE EFFICIENCY PERFORMANCE OF BASELINE AND OPTIMAL ROTOR BAR

Baseline vs. Optimal Efficiency Performance		
Baseline IM (%)	Optimized IM (%)	Percent Increase (%)
66.2348	67.7951	2.3558
75.0589	76.4498	1.8531
90.0975	90.7080	0.6777
89.0431	89.8815	0.9415
91.5984	92.2218	0.6805
66.2348	67.7951	2.3558
75.0589	76.4498	1.8531
Average Change		**1.3017**

CHAPTER 7   Research Summary

7.1. Conclusions

In conclusion, to develop an algorithm capable of dynamic multi-objective optimization of a tractive induction machine rotor bar for higher torque and lower losses, a novel, robust non-dominated adaptive restart GA was proposed and developed to ensure high quality solutions and low run times while eliminating function bias between objectives. Through the incorporation of drive cycle based operating points, the non-dominated adaptive restart GA is able to optimize the rotor bar geometry of a tractive IM with respect to output torque and total losses under dynamic operating conditions. The optimal rotor bar produced by the newly proposed non-dominated adaptive restart GA is capable of producing an average of 7.51% higher torque and 0.553% lower losses across all significant operating points resulting in a tractive IM with an equal increase in torque density as the machine weight remained constant and an operating efficiency increase of an average 1.3%. Although the losses were not improved by the target 3%, the optimal rotor bar design produced offers more than 5.51% large improvement in the output torque than the target 3%. Therefore, the smaller improvement in losses is justified by the overall IM performance. The optimized tractive IM with higher torque density and operating efficiency may now be used in a commercially available EV resulting in better tractive performance and extended rangers. Through the proposed method, objectives at every level of the optimization problem were met by the proposed deliverables resulting in the global objective being achieved.

7.2. Future Research on Rotor Bar Optimization of Tractive IMs

To pursue geometric rotor bar optimization further, the permeance based equivalent circuit model may be modified to incorporate the effects of rotor bar skewing and pitching, allowing the rotor skew and rotor slot pitch to be an input to the OA. This increases the number of possible rotor bar designs the algorithm can generate. However, it would introduce complex mathematics into the analytical model and increase the run time of the algorithm, which will need to be addressed. The incorporation of double caged rotor bar geometries would also greatly increase the number of possible solutions. However, the analytical model would likely need to be modified to toggle between single and double cage-based models depending on the input of the OA, greatly increasing the complexity of the model. Lastly, rotor bar optimization should be expanded to incorporate major stator components into the optimization as well, allowing both the rotor and stator to be optimized simultaneously. This may require reducing the number of rotor-based input variables in order to maintain a reasonable number of inputs to the OA, while a large number of additional constraints and limitations will be introduced into the optimization problem.

REFERENCES

[1]   Total greenhouse gas emissions. Our World in Data. [Online]. Available: https://ourworldindata.org/grapher/total-ghg-emissions?tab=chart&country=~OWID_WRL

[2]   D. Gielen, F. Boshell, D. Saygin, M. D. Bazilian, N. Wagner, and R. Gorini, "The role of renewable energy in the global energy transformation," *Energy Strategy Reviews*, vol. 24, pp. 38–50, April 2019. doi: 10.1016/J.ESR.2019.01.006.

[3]   H. Ritchie, M. Roser, and P. Rosado. (2020). Greenhouse gas emissions. Our World in Data. [Online]. Available: https://ourworldindata.org/co2-and-other-greenhouse-gas-emissions

[4]   (2022, May) "Facility Greenhouse Gas Reporting: Overview of 2020 Reported Emissions'. Government of Canada. Canada. [Online]. Available : https://www.canada.ca/en/environment-climate-change/services/climate-change/greenhouse-gas-emissions/facility-reporting/overview-2020.html#shr-pg0

[5]   A. Bellini, F. Filippetti, C. Tassoni, and G. A. Capolino, "Advances in diagnostic techniques for induction machines," *IEEE Trans. Industrial Electronics*, vol. 55, no. 12, pp. 4109–4126, 2008. doi: 10.1109/TIE.2008.2007527.

[6]   Global EV outlook 2021 - Introduction. IEA. [Online]. Available: https://www.iea.org/reports/global-ev-outlook-2021/introduction#overview

[7]   Audi MediaCenter (2017) Audi e-tron Sportback concept. [Online]. Available: https://www.audi-mediacenter.com/en/photos/detail/audi-e-tron-sportback-concept-44496

[8]   H. de Keulenaer, "Energy efficient motor driven systems," *Energy and Environment*, vol. 15, no. 5, pp. 873–905, 2004. doi: 10.1260/0958305042886688.

[9]   P. C. Krause, O. Wasynczuk, and S. D. Sudhoff. (2002). *Analysis of Electric Machinery and Drive Systems*. [Online]. Available: https://ieeexplore.ieee.org/book/5265638

[10]   F. Blaabjerg, H. Wang, I. Vernica, B. Liu and P. Davari, "Reliability of Power Electronic Systems for EV/HEV Applications," in Proceedings of the IEEE, vol. 109, no. 6, pp. 1060-1076, June 2021, doi: 10.1109/JPROC.2020.3031041

[11]   L. Yan and X. Song, "Design and implementation of Luenberger model-based predictive torque control of induction machine for robustness improvement," *IEEE Trans. Power Electronics*, vol. 35, no. 3, pp. 2257–2262, Mar. 2020. doi: 10.1109/TPEL.2019.2939283.

[12]   M. Karamuk, "A survey on electric vehicle powertrain systems," in *Proc. Int. Aegean Conf. Electr. Mach. Power Electron. Electromotion Joint Conf.*, 2011, pp. 315–324. doi: 10.1109/ACEMP.2011.6490617.

[13]   H. E. Jordan, R. C. Zowarka, T. J. Hotz, and J. R. Uglum, "Induction motor performance testing with an inverter power supply: Part 1," *IEEE Trans. Magnetics*, vol. 43, no. 1, pp. 242–245, Jan. 2007. doi: 10.1109/TMAG.2006.887671.

[14] R. C. Zowarka, T. J. Hotz, J. R. Uglum, and H. E. Jordan, "Induction motor performance testing with an inverter power supply: Part 2," *IEEE Trans. Magnetics*, vol. 43, no. 1, pp. 275–278, Jan. 2007. doi: 10.1109/TMAG.2006.887599.

[15] Global EV outlook 2021 - Policies to promote electric vehicle deployment. IEA. [Online]. Available: https://www.iea.org/reports/global-ev-outlook-2021/policies-to-promote-electric-vehicle-deployment

[16] G. K. Singh, "Multi-phase induction machine drive research - A survey," *Electric Power Systems Research*, vol. 61, no. 2, pp. 139–147, Mar. 2002. doi: 10.1016/S0378-7796(02)00007-X.

[17] EV30@30 campaign. Clean Energy Ministerial [Online]. Available: https://www.cleanenergyministerial.org/initiatives-campaigns/ev3030-campaign

[18] Global plug-in electric vehicle market share in 2021, by main producers. Statista. [Online]. Available: https://www.statista.com/statistics/541390/global-sales-of-plug-in-electric-vehicle-manufacturers

[19] Global Electric car registrations and market share, 2015-2020. IEA. [Online]. Available: https://www.iea.org/data-and-statistics/charts/global-electric-car-registrations-and-market-share-2015-2020

[20] Transport sector CO2 emissions by mode in the Sustainable Development Scenario, 2000-2030. IEA. [Online]. Available: https://www.iea.org/data-and-statistics/charts/transport-sector-co2-emissions-by-mode-in-the-sustainable-development-scenario-2000-2030

[21] List of eligible vehicles under the iZEV Program. Transport Canada. [Online]. Available: https://tc.canada.ca/en/road-transportation/innovative-technologies/zero-emission-vehicles/list-eligible-vehicles-under-izev-program

[22] "Stellantis plants in Windsor, Brampton to get $3.6B in upgrades for EV production," *CBC News*, May 2, 2022. [Online]. Available: https://www.cbc.ca/news/canada/windsor/prime-minister-ontario-premier-stellantis-windsor-announcement-1.6437954

[23] Electric Vehicle Database. [Online]. Available: https://ev-database.org/#sort:path~type~order=.rank~number~desc|range-slider-range:prev~next=0~1200|range-slider-acceleration:prev~next=2~23|range-slider-topspeed:prev~next=110~450|range-slider-battery:prev~next=10~200|range-slider-towweight:prev~next=0~2500|range-slider-fastcharge:prev~next=0~1500|paging:currentPage=0|paging:number=9

[24] EVSpecifications - Electric vehicle specifications, electric car news, EV comparisons. [Online]. Available: https://www.evspecifications.com

[25] Mark Kane. (2022, Feb). Compare Electric Cars: EV Range, Specs, Pricing & More. INSIDEEVs. [Online]. Available: https://insideevs.com/reviews/344001/compare-evs

[26] B. Bilgin and A. Emadi, "Electric motors in electrified transportation: A step toward achieving a sustainable and highly efficient transportation system," *IEEE Power*

Electronics Magazine, vol. 1, no. 2, pp. 10–17, Jun. 2014. doi: 10.1109/MPEL.2014.2312275.

[27] J. Zhang, B. Wang, Y. Yu, H. Cai, X. Zhang, and D. Xu, "Angle compensation-based voltage redistribution for induction motor drives in the field-weakening windup region," in *Proc. 22nd Int. Conf. Electr. Mach. Syst.*, (*ICEMS*), Aug. 2019. pp. 1-6. doi: 10.1109/ICEMS.2019.8921483.

[28] C. S. N. Shiau, C. Samaras, R. Hauffe, and J. J. Michalek, "Impact of battery weight and charging patterns on the economic and environmental benefits of plug-in hybrid vehicles," *Energy Policy*, vol. 37, no. 7, pp. 2653–2663, July 2009. doi: 10.1016/J.ENPOL.2009.02.040.

[29] C. Lai, G. Feng, Z. Li, and N. C. Kar, "Computation-efficient decoupled multiparameter estimation of PMSMs from massive redundant measurements," *IEEE Trans. Power Electronics*, vol. 35, no. 10, pp. 10729–10740, Oct. 2020. doi: 10.1109/TPEL.2020.2980315.

[30] A. Vagati, G. Pellegrino, and P. Guglielmi, "Comparison between SPM and IPM motor drives for EV application," in *Proc. Int. Conf. Electri. Mach.*, (*ICEM*), 2010, pp. 1-6. doi: 10.1109/ICELMACH.2010.5607911.

[31] Y. Guan, Z. Q. Zhu, I. A. A. Afinowi, J. C. Mipo, and P. Farah, "Comparison between induction machine and interior permanent magnet machine for electric vehicle application," *17th Int. Conf. Electr. Mach. Syst.,* (ICEMS), 2014, pp. 144-150. doi: 10.1109/ICEMS.2014.7013454.

[32] K. Kim, J. Bae, W. H. Kim, S. H. Ham, S. Cho, and J. Lee, "Design and comparison between IM and PMSM for hybrid electrical vehicles," in *Proc. Digests. 2010 14th Biennial IEEE Conf. Electromagnetic Field Computation,* (*CEFC*), 2010, pp. 1-1. doi: 10.1109/CEFC.2010.5481798.

[33] Viktor Bobek, "PMSM electrical parameters measurement," F. Semiconductor Inc., AN4680, 2013. [Online]. Available: https://wenku.baidu.com/view/f1e90d56f7ec4afe04a1df4d.html

[34] G. Bramerdorfer, G. Weidenholzer, S. Silber, W. Amrhein, and S. Lanser, "Measurement-based nonlinear modeling of PMSMs," in *Proc. IECON 2015 - 41st Annu. Conf. IEEE Ind. Electron. Soc.*, 2015, pp. 2036–2041. doi: 10.1109/IECON.2015.7392400.

[35] G. Bramerdorfer, A. Cavagnino, and S. Vaschetto, "Cost-optimal machine designs fulfilling efficiency requirements: A comparison of IMs and PMSMs," in *Proc. IEEE Int. Electr. Mach. Drives Conf.,* (*IEMDC*), 2017, pp. 1-8, doi: 10.1109/IEMDC.2017.8002044.

[36] S. Mallik *et al.*, "Efficiency and cost optimized design of an induction motor using genetic algorithm," *IEEE Trans. Industrial Electronics*, vol. 64, no. 12, pp. 9854–9863, Dec. 2017, doi: 10.1109/TIE.2017.2703687.

[37] Y. C. Zhuang, H. Yu, and J. Xia, "A novel adaptive genetic algorithm applied to optimizing linear induction machines." in *Proc. Int. Conf. Electr. Mach. Syst.,* 2008, pp. 3435-3438.

109

[38] M. A. Kabir, M. Z. M. Jaffar, Z. Wan, and I. Husain "Design, optimization, and experimental evaluation of multilayer ac winding for induction machine," IEEE T*rans. Ind. Appl.,* vol. 55, no. 4, pp. 3630-3639, July-Aug. 2019. doi: 10.1109/TIA.2019.2910775.

[39] O. Dobzhanskyi, E. Amiri and R. Gouws, "Comparison analysis of electric motors with two degrees of mechanical freedom: PM synchronous motor vs induction motor," 2016 II International Young Scientists Forum on Applied Physics and Engineering (YSF), 2016, pp. 14-17, doi: 10.1109/YSF.2016.7753750.

[40] E. Gary, A. Magno and R. Jorge, "Design, analysis and validation of a six-phase induction machine from a commercial three-phase for academic research," *I*EEE Latin America Transactions, vol. 18, no. 11, pp. 1943-1952, Nov. 2020. doi: 10.1109/TLA.2020.9398636.

[41] M. J. Akhtar and R. K. Behera, "Optimal design of stator and rotor slot of induction motor for electric vehicle applications," *IET Electr. Syst. Transp.*, vol. 9, no. 1, pp. 35–43, Mar. 2019, doi: 10.1049/iet-est.2018.5050.

[42] A. Mollaeian, E. Ghosh, H. Dhulipati, J. Tjong, and N. C. Kar, "3-D sub-domain analytical model to calculate magnetic flux density in induction machines with semi-closed slots under no-load condition," *IEEE Trans.* Magnetics, vol. 53, no. 6, pp. 1-5, June 2017, Art no. 7206905. doi: 10.1109/TMAG.2017.2658543

[43] H. Tang, M. Zhang, Y. Dong, W. Li, and L. Li, "Influence of the opening width of stator semi-closed slot and the dimension of the closed slot on the magnetic field distribution and temperature field of the permanent magnet synchronous motor," *IET Electr. Power Appl.*, vol. 14, no. 2, pp. 1642–1652, Sep. 2020. doi: 10.1049/iet-epa.2019.0736.

[44] A. S. Abdel-Khalik, M. I. Daoud, S. Ahmed, A. A. Elserougi, and A. M. Massoud, "Parameter identification of five-phase induction machines with single layer windings," *IEEE Trans. Industrial Electronics*, vol. 61, no. 10, pp. 5139–5154, 2014. doi: 10.1109/TIE.2013.2297294.

[45] Y. Xu, Z. Xu, and M. Ai, "Application of ring winding in induction motor," *IEEE Trans. Applied Superconductivity*, vol. 31, no. 8, pp. 1-5, Nov. 2021. doi: 10.1109/TASC.2021.3107809.

[46] S. Mallampalli, Z. Q. Zhu, J. C. Mipo, and S. Personnaz, "Six-phase pole-changing winding induction machines with improved performance*," IEEE Trans. Energy Conversion*, vol. 36, no. 1, pp. 534–546, Mar. 2021. doi: 10.1109/TEC.2020.3009190.

[47] J. M. Apsley and S. Williamson, "Analysis of multiphase induction machines with winding faults," *IEEE Trans. Industry Applications*, vol. 42, no. 2, pp. 465–472, Mar. 2006. doi: 10.1109/TIA.2005.863915.

[48] A. S. Abdel-Khalik, M. S. Abdel-Majeed, and S. Ahmed, "Effect of winding configuration on six-phase induction machine parameters and performance," *IEEE Access*, vol. 8, pp. 223009–223020, 2020. doi: 10.1109/ACCESS.2020.3044025.

110

[49]   G. Rezazadeh, F. Tahami, G. A. Capolino, S. Vaschetto, Z. Nasiri-Gheidari, and H. Henao, "Improvement of concentrated winding layouts for six-phase squirrel cage induction motors," *IEEE Trans. Energy Conversion*, vol. 35, no. 4, pp. 1727–1735, Dec. 2020. doi: 10.1109/TEC.2020.2995433.

[50]   D. J. Kim, J. W. Jung, J. P. Hong, K. J. Kim, and C. J. Park, "A study on the design process of noise reduction in induction motors," *IEEE Trans. Magnetics*, vol. 48, no. 11, pp. 4638–4641, 2012. doi: 10.1109/TMAG.2012.2197187.

[51]   M. A. Khoshhava, H. A. Zarchi, and G. A. Markadeh, "Optimal design of a dual stator winding induction motor with minimum rate reduction level," *IEEE Trans. Industrial Electronics*, vol. 68, no. 2, pp. 1016–1024, Feb. 2021. doi: 10.1109/TIE.2020.2967690.

[52]   K. Sedef, A. Maheri, M. Yilmaz, and A. Daadbin, "Performances of AC induction motors with different number of poles in urban electric cars," in *Proc. 3rd Int. Symp. Environ. Friendly Energies. Appl.,* (*EFEA*), 2014, pp. 1-5. doi: 10.1109/EFEA.2014.7059946.

[53]   T. Gundogdu, Z. Q. Zhu, and J. C. Mipo, "Influence of stator slot and pole number combination on rotor bar current waveform and performance of induction machines," in *Proc. 20th Int. Conf. Electr. Mach. Syst.,* (*ICEMS*), 2017. pp. 1-6. doi: 10.1109/ICEMS.2017.8055937.

[54]   K. Gyftakis, J. Kappatou, and A. Safacas, "FEM study of asynchronous cage motors combining NEMA's classes A and D slot geometry," in *Proc. 19th Int. Conf. Electr. Mach.,* (*ICEM*), 2010, pp. 1-6. doi: 10.1109/ICELMACH.2010.5607691.

[55]   K. W. Jeon, T. K. Chung, and S. C. Hahn, "NEMA class A slot shape optimization of induction motor for electric vehicle using response surface method," in *Proc. Int. Conf. Electr. Mach. Syst.,* (*ICEMS*), 2011, pp. 1-4. doi: 10.1109/ICEMS.2011.6073692.

[56]   V. F. Syvokobylenko and S. N. Tkachenko, "Bar diagnostics of double cage or deep bar rotor of an induction motor," in *Proc. Int. Conf. Ind. Eng. Appl. Manuf.,* (*ICIEAM*), 2020, pp. 1-7. doi: 10.1109/ICIEAM48468.2020.9111880.

[57]   C. G. Heo, H. M. Kim, and G. S. Park, "A design of rotor bar inclination in squirrel cage induction motor," *IEEE Trans. Magnetics*, vol. 53, no. 11, pp. 1-4, Nov. 2017. doi: 10.1109/TMAG.2017.2696977.

[58]   J. Marault, A. Tounzi, F. Gillon, and M. Hecquet, "Efficient approach based on equivalent electric circuit model to determine rotor bar currents of squirrel cage induction machines," *IEEE Trans. Magnetics*, vol. 57, no. 2, pp. 1-5, Feb. 2021. doi: 10.1109/TMAG.2020.3011612.

[59]   D. Zhang, C. S. Park, and C. S. Koh, "A new optimal design method of rotor slot of three-phase squirrel cage induction motor for NEMA class D speed-torque characteristic using multi-objective optimization algorithm," *IEEE Trans. Magnetics*, vol. 48, no. 2, pp. 879-882, 2012. doi: 10.1109/TMAG.2011.2174040.

[60]   H. K. Kwan. (2018, March 13). *Global Optimization Algorithms and Design Applications.* (1.2 ed.). ISBN13: 9781988307046

111

[61] A. P. Yadav, R. Madani, N. Amiri, J. Jatskevich, and A. Davoudi, "Induction machine parameterization from limited transient data using convex optimization," *IEEE Trans. Industrial Electronics*, vol. 69, no. 2, pp. 1254–1265, Feb. 2022. doi: 10.1109/TIE.2021.3060668.

[62] N. Taran, D. M. Ionel, and D. G. Dorrell, "Two-level surrogate-assisted differential evolution multi-objective optimization of electric machines using 3-D FEA," *IEEE Trans. Magnetics*, vol. 54, no. 11, Nov. 2018. doi: 10.1109/TMAG.2018.2856858.

[63] C. López-Torres, A. G. Espinosa, J. R. Riba, and L. Romeral, "Design and optimization for vehicle driving cycle of rare-earth-free SynRM based on coupled lumped thermal and magnetic networks," *IEEE Trans. Vehicular Technology,* vol. 67, no. 1, pp. 196–205, Jan. 2018. doi: 10.1109/TVT.2017.2739020.

[64] N. Zhao and N. Schofield, "An induction machine design with parameter optimization for a 120-kW electric vehicle," *IEEE Trans. Transportation Electrification*, vol. 6, no. 2, pp. 592–601, Jun. 2020. doi: 10.1109/TTE.2020.2993456.

[65] G. Bramerdorfer, A. C. Zavoianu, S. Silber, E. Lughofer, and W. Amrhein, "Speed improvements for the optimization of electrical machines - A survey," in *Proc. IEEE Int. Electr. Mach. Drives Conf.*, (*IEMDC*), 2015, pp. 1748–1754. doi: 10.1109/IEMDC.2015.7409300.

[66] L. Alberti, N. Bianchi, and S. Bolognani, "A very rapid prediction of IM performance combining analytical and finite-element analysis," *IEEE Trans. Industry Applications*, vol. 44, no. 5, pp. 1505–1512, 2008. doi: 10.1109/TIA.2008.2002185.

[67] T. Garbiec, M. Jagiela, and M. Kulik, "Application of nonlinear complex polyharmonic finite-element models of high-speed solid-rotor induction motors," *IEEE Trans. Magnetics*, vol. 56, no. 4, pp. 1-4, Apr. 2020, doi: 10.1109/TMAG.2019.2953987.

[68] T. Schuhmann, B. Cebulski, and S. Paul, "Comparison of time-harmonic and transient finite element calculation of a squirrel cage induction machine for electric vehicles," in *Proc. Int. Conf. Electr. Mach.,* (*ICEM*), 2014, pp. 1037–1043. doi: 10.1109/ICELMACH.2014.6960309.

[69] D. K. Kim and B. il Kwon, "A novel equivalent circuit model of linear induction motor based on finite element analysis and its coupling with external circuits," *IEEE Trans. Magnetics*, vol. 42, no. 10, pp. 3407–3409, 2006, doi: 10.1109/TMAG.2006.879078.

[70] L. Montier, T. Henneron, S. Clenet, and B. Goursaud, "Model order reduction applied to a linear finite element model of a squirrel cage induction machine based on POD approach," *IEEE Trans. Magnetics*, vol. 57, no. 6, pp.1-4, Jun. 2021. doi: 10.1109/TMAG.2021.3066678.

[71] T. A. Lipo, "Magnetic circuits," *Introduction to AC Machine Design*, *IEEE*, 2018, pp. 1–50. doi: 10.1002/9781119352181.CH1.

[72]   T. M. Wolbank, R. Woehrnschimmel, and H. Hauser, "Transient magnetic modeling and measurements of sensorless controlled induction machines," *IEEE Trans. Magnetics*, vol. 38, no. 5, pp. 3279–3284, Sep. 2002. doi: 10.1109/TMAG.2002.803312.

[73]   J. Brudny, J. Lecointe, F. Morganti, F. Zidat, and R. Romary, "Use of the external magnetic field for induction machine leakage inductance distinction," *IEEE Trans. Magnetics,* vol. 46, no. 6, pp. 2205–2208, Jun. 2010. doi: 10.1109/TMAG.2010.2049005.

[74]   A. Repo, P. Rasilo, A. Niemenmaa, and A. Arkkio, "Identification of electromagnetic torque model for induction machines with numerical magnetic field solution," *IEEE Trans. Magnetics*, vol. 44, no. 6, pp. 1586–1589, Jun. 2008. doi: 10.1109/TMAG.2007.916143.

[75]   F. Sarapulov, S. Sarapulov, and I. Smolyanov, "Compensated linear induction motor characteristics research by detailed magnetic equivalent circuit," in *Proc. Int. Conf. Ind. Eng. Appl. Manuf.,* (*ICIEAM*), 2017. doi: 10.1109/ICIEAM.2017.8076314.

[76]   M. Amrhein and P. T. Krein, "Induction machine modeling approach based on 3-D magnetic equivalent circuit framework," *IEEE Trans. Energy Conversion*, vol. 25, no. 2, pp. 339–347, Jun. 2010. doi: 10.1109/TEC.2010.2046998.

[77]   M. Tezcan, A. G. Yetgin, A. I. Canakoglu, B. Cevher, M. Turan, and M. Ayaz, "Investigation of the effects of the equivalent circuit parameters on induction motor torque using three different equivalent circuit models," *MATEC Web of Conferences*, vol. 157, 2018. doi: 10.1051/matecconf/201815701019.

[78]   A. Boglietti, A. Cavagnino, and M. Lazzari, "Computational algorithms for induction motor equivalent circuit parameter determination-Part II: Skin effect and magnetizing characteristics," *IEEE Trans. Industrial Electronics*, vol. 58, no. 9, pp. 3734–3740, Sep. 2011, doi: 10.1109/TIE.2010.2084975.

[79]   A. Boglietti, A. Cavagnino, and M. Lazzari, "Computational algorithms for induction-motor equivalent circuit parameter determination-Part I: Resistances and leakage reactances," *IEEE Trans. Industrial Electronics*, vol. 58, no. 9, pp. 3734–3740, Sep. 2011. doi: 10.1109/TIE.2010.2084974.

[80]   N. Ullah, F. Khan, W. Ullah, M. Umair, and Z. Khattak, "Magnetic equivalent circuit models using global reluctance networks methodology for design of permanent magnet flux switching machine," *15th Int. Bhurban Conf. Appl. Sci. Technol.,* (IBCAST), 2018, pp. 397-404. doi: 10.1109/IBCAST.2018.8312255.

[81]   A. Fatima *et al*., "Permeance-based equivalent circuit modeling of induction machines considering leakage reactances and non-linearities for steady-state performance prediction," in *Proc. 47th Annu. Conf. IEEE Ind. Electron.* Society, 2021, pp. 1-6. doi: 10.1109/IECON48115.2021.9589909.

[82]   J. Marault, A. Tounzi, F. Gillon, and M. Hecquet, "Efficient approach based on equivalent electric circuit model to determine rotor bar currents of squirrel cage induction machines," *IEEE Trans. Magnetics*, vol. 57, no. 2, pp. 1-5, Feb. 2021. doi: 10.1109/TMAG.2020.3011612.

113

[83] A. Boglietti, A. Cavagnino, and M. Lazzari, "Computational algorithms for induction-motor equivalent circuit parameter determination-Part I: Resistances and leakage reactances," *IEEE Trans. Industrial Electronics*, vol. 58, no. 9, pp. 3723–3733, Sep. 2011. doi: 10.1109/TIE.2010.2084974.

[84] A. Boglietti, A. Cavagnino, and M. Lazzari, "Computational algorithms for induction motor equivalent circuit parameter determination-Part II: Skin effect and magnetizing characteristics," *IEEE Trans. Industrial Electronics*, vol. 58, no. 9, pp. 3734–3740, Sep. 2011. doi: 10.1109/TIE.2010.2084975.

[85] K. Hafiz, G. Nanda, and N. C. Kar, "Performance analysis of aluminum- and copper-rotor induction generators considering skin and thermal effects," *IEEE Trans. Industrial Electronics*, vol. 57, no. 1, pp. 181–192, Jan. 2010. doi: 10.1109/TIE.2009.2034177.

[86] A. C. Zăvoianu, G. Bramerdorfer, E. Lughofer, S. Silber, W. Amrhein, and E. Peter Klement, "Hybridization of multi-objective evolutionary algorithms and artificial neural networks for optimizing the performance of electrical drives," *Eng. Appl. Artif. Intell.*, vol. 26, no. 8, pp. 1781–1794, Sep. 2013. doi: 10.1016/J.ENGAPPAI.2013.06.002.

[87] J. le Besnerais, V. Lanfranchi, M. Hecquet, R. Romary, and P. Brochet, "Optimal slot opening width for magnetic noise reduction in induction motors," *IEEE Trans. Energy Conversion*, vol. 24, no. 4, pp. 869–874, Dec. 2009. doi: 10.1109/TEC.2009.2025421.

[88] G. Joksimović, E. Levi, A. Kajević, M. Mezzarobba and A. Tessarolo, "Optimal Selection of Rotor Bar Number for Minimizing Torque and Current Pulsations Due to Rotor Slot Harmonics in Three-Phase Cage Induction Motors," in IEEE Access, vol. 8, pp. 228572-228585, 2020, doi: 10.1109/ACCESS.2020.3045766.

[89] S. P. Han and O. L. Mangasarian, "Exact penalty functions in nonlinear programming," *Mathematical Programming*, vol. 17, no. 1, pp. 251–269, Dec. 1979. doi: 10.1007/BF01588250.

[90] J. B. Lasserre, "A globally convergent algorithm for exact penalty functions," *European Journal of Operational Research*, vol. 7, no. 4, pp. 389–395, 1981. doi: 10.1016/0377-2217(81)90097-7.

[91] E. Rosenberg, "Exact penalty functions and stability in locally Lipschitz programming," *Mathematical Programming*, vol. 30, no. 3, pp. 340–356, Oct. 1984. doi: 10.1007/BF02591938.

[92] Z. Meng, M. Jiang, and C. Dang, "Evolutionary algorithm for zero-one constrained optimization problems based on objective penalty function," in *Proc. Int. Conf. Comput. Intell. Security, (CIS*), 2010, pp. 132–136. doi: 10.1109/CIS.2010.36.

[93] Z. Wang and S. Liu, "A new smooth method for the l1 exact penalty function for inequality constrained optimization," in *Proc. 3rd Int. Joint Conf. Comput. Sciences. Optimization*, (*CSO*) 2010, pp. 110–113. doi: 10.1109/CSO.2010.157.

[94]   A. Mallick, S. Roy, S. S. Chaudhuri, and S. Roy, "Study of parametric optimization of the Cuckoo Search algorithm," *Int. Conf. Control, Instrum. Energy. Communication,* (*CIEC*), 2014, pp. 767–772. doi: 10.1109/CIEC.2014.6959194.

[95]   S. Halgas and M. Tadeusiewicz, "Improvement of the search method for parametric fault diagnosis of analog integrated circuits," in *Proc. 23rd Int. Conf. Mixed Design of Integrated Circuits and Systems*, (*MIXDES*) 2016, pp. 359–362. doi: 10.1109/MIXDES.2016.7529765.

[96]   J. Kennedy and R. Eberhart, "Particle swarm optimization," in *Proc. Int. Conf. Neural Networks*, 1995, vol. 4, pp. 1942–1948. doi: 10.1109/ICNN.1995.488968.

[97]   Y. Shi and R. C. Eberhart, "Empirical study of particle swarm optimization," in *Proc. Congress on Evolutionary Computation*, (*CEC*), 1999, vol. 3, pp. 1945–1950. doi: 10.1109/CEC.1999.785511.

[98]   V. P. Sakthivel, R. Bhuvaneswari, and S. Subramanian, "An improved particle swarm optimization for induction motor parameter determination," *International Journal of Computer Applications*, vol. 1, no. 2, pp. 71–76, Feb. 2010. doi: 10.5120/44-150.

[99]   K. T. Chaturvedi, M. Pandit, and L. Srivastava, "Particle swarm optimization with time varying acceleration coefficients for non-convex economic power dispatch," *International Journal of Electrical Power and Energy Systems*, vol. 31, no. 6, pp. 249–257, Jul. 2009. doi: 10.1016/J.IJEPES.2009.01.010.

[100] M. G. Bijan and P. Pillay, "Efficiency estimation of the induction machine by particle swarm optimization using rapid test data with range constraints," *IEEE Trans. Industrial Electronics*, vol. 66, no. 8, pp. 5883–5894, Aug. 2019. doi: 10.1109/TIE.2018.2873121.

[101] A. Trentin, P. Zanchetta, P. Wheeler, J. Clare, R. Wood, and D. Katsis, "A New Method for Induction Motors Parameter Estimation Using Genetic Algorithms and Transient Speed measurements," Conference Record of the 2006 IEEE Industry Applications Conference Forty-First IAS Annual Meeting, 2006, pp. 2435-2440. doi: 10.1109/IAS.2006.256881.

[102] A. Trentin, P. Zanchetta, P. Wheeler, and J. Clare, "Improved Vector Control of Induction Motor Drives Using Genetic Algorithms-based Machine and Control Parameters Estimation," *European Conf. Power Electron.* Applications, 2007, pp. 1-8. doi: 10.1109/EPE.2007.4417732.

[103] X. S. Yang and S. Deb, "Engineering optimisation by cuckoo search," *Int. J. Mathematical Modelling and Numerical Optimisation*, vol. 1, no. 4, pp. 330–343, 2010. doi: 10.1504/IJMMNO.2010.035430.

[104] M. T. Goodrich and P. Pszona, "Cole's parametric search technique made practical," Cornell University, 2013. [Online]. Available: https://doi.org/10.48550/arXiv.1306.3000

[105] A. Chatterjee and P. Siarry, "Nonlinear inertia weight variation for dynamic adaptation in particle swarm optimization," *Computers and Operations Research*, vol. 33, no. 3, pp. 859–871, Mar. 2006. doi: 10.1016/J.COR.2004.08.012.

115

[106] C. Guangyi, G. Wei, and H. Kaisheng, "On line parameter identification of an induction motor using improved particle swarm optimization," in *Proc. 26th Chinese Control Conference*, (*CCC*), 2007, pp. 745–749. doi: 10.1109/CHICC.2006.4347151.

[107] Y. Shi and R. C. Eberhart, "Parameter selection in particle swarm optimization," *Lecture Notes in Computer Science* , Berlin, Springer, 2005, vol. 1447, pp. 591–600, 1998, doi: 10.1007/BFB0040810.

[108] M. Rayyam and M. Zazi, "Particle swarm optimization of a non-linear Kalman filter for sensorles control of induction motors," *7th Int. IEEE Conf. Renewable Energy Research. Appl.*, (*ICRERA*), 2018, pp. 1016–1020. doi: 10.1109/ICRERA.2018.8566984.

[109] A. Gupta, R. Machavaram, T. Kshatriya and S. Ranjan, "Multi-Objective Design Optimization of a Three Phase Squirrel Cage Induction Motor for Electric Propulsion System using Genetic Algorithm," *2020 IEEE First Int. Conf. Smart Technologies for Power, Energy and Control, (STPEC)*, 2020, pp. 1-6, doi: 10.1109/STPEC49749.2020.9297776.

[110] F. Alonge, F. D'Ippolito, and F. M. Raimondi, "Least squares and genetic algorithms for parameter identification of induction motors," *Control Engineering Practice*, vol. 9, no. 6, pp. 647–657, Jun. 2001, doi: 10.1016/S0967-0661(01)00024-7.

[111] S. Surjanovic and D. Bingham, "Schwefel Function." Simon Fraser University. [Online]. Available: https://www.sfu.ca/~ssurjano/schwef.html

[112] M. di Nardo, A. Marfoli, M. Degano, C. Gerada, and W. Chen, "Rotor design optimization of squirrel cage induction motor-Part II: results discussion," *IEEE Trans. Energy Conversion*, vol. 36, no. 2, pp. 1280–1288, Jun. 2021. doi: 10.1109/TEC.2020.3020263.

[113] A. Marfoli, M. di Nardo, M. Degano, C. Gerada, and W. Chen, "Rotor design optimization of squirrel cage induction motor-Part I: problem statement," *IEEE Trans. Energy Conversion*, vol. 36, no. 2, pp. 1271–1279, Jun. 2021. doi: 10.1109/TEC.2020.3019934.

[114] K. Bitsi, O. Wallmark, and S. Bosga, "Many-objective optimization of IPM and induction motors for automotive application," in *Proc. 21st European Conf. Power Electron. Appl.*, (*EPE 2019 ECCE Europe*), Sep. 2019, pp.1-10. doi: 10.23919/EPE.2019.8914848.

[115] L. A. Pereira, S. Haffner, G. Nicol, and T. F. Dias, "Multiobjective optimization of five-phase induction machines based on NSGA-II," *IEEE Trans. Industrial Electronics*, vol. 64, no. 12, pp. 9844–9853, Dec. 2017. doi: 10.1109/TIE.2017.2701768.

[116] K. Postoyankova, V. Polishchuk and A. Shuvalova, "Research of a Genetic Algorithm for Identification of Induction Motor Parameters," 2021 International Conference on Industrial Engineering, Applications and Manufacturing (ICIEAM), 2021, pp. 334-338, doi: 10.1109/ICIEAM51226.2021.9446342.

[117] Y. Chen and P. Pillay, "An improved formula for lamination core loss calculations in machines operating with high frequency and high flux density excitation,". in *Proc. Conf. Record. 2002 IEEE Ind. Appl. Conf. 37th IAS Annu.* Meeting. (Cat. No.02CH37344), 2002, pp. 759-766. doi: 10.1109/IAS.2002.1042645.

[118] M. Nour and P. Thirugnanam, "Investigation of voltage and frequency variation on induction motor core and copper losses," *7th Int. Conf. Modeling, Simulation. Applied Optimization,* (*ICMSAO*), 2017, pp. 1-5. doi: 10.1109/ICMSAO.2017.7934894.

[119] O. Laldin, E. Dlala, and A. Arkkio, "Circuit models for predicting core losses in the stator and rotor of a caged induction machine with sinusoidal supplies," *IEEE Trans. Magnetics*, vol. 47, no. 5, pp. 1054–1057, May 2011. doi: 10.1109/TMAG.2010.2097582.

[120] B. D. S. G. Vidanalage, M. S. Toulabi, T. Stachl, A. Lombardi, J. Tjong, and N. C. Kar, "Winding function-based analytical modeling of core loss in an induction machine considering slotting effects and the frequency-dependent B-H curve characteristics," *IEEE Trans. Magnetics*, 2022. doi: 10.1109/TMAG.2022.3148759.

[121] "The different driving cycles," *Car Engineer*. [Online]. Available: https://www.car-engineer.com/the-different-driving-cycles

[122] A. K. Atalay, D. A. Kocabas, M. Imeryuz, and M. O. Gulbahce, "Analysis of problems in a load system driven by multiple tandem induction motors," in *Proc. 15th Int. Conf.* MECHATRONIKA, 2012, pp. 1-5.

[123] M. Kitzberger, G. Bramerdorfer, S. Silber, H. Mitterhofer, and W. Amrhein, "Influence of hysteresis and eddy current losses on electric drive energy balance in driving cycle operation," in *Proc. 8th Int. Electr. Drives Prod. Conf.*, (*EDPC*), 2018, pp. 1-7. doi: 10.1109/EDPC.2018.8658302.

[124] V. Ruuskanen, J. Nerg, J. Pyrhonen, S. Ruotsalainen, and R. Kennel, "Drive cycle analysis of a permanent-magnet traction motor based on magnetostatic finite-element analysis," *IEEE Trans. Vehicular Technology*, vol. 64, no. 3, pp. 1249–1254, Mar. 2015. doi: 10.1109/TVT.2014.2329014.

[125] Y. Zhang, H. Peng, and W. Hofmann, "Load cycle-based design optimization of induction motor drives for highly dynamic applications," in *Proc. IEEE Int. Conf. Ind. Technology*, vol. 2019, pp. 286–291. doi: 10.1109/ICIT.2019.8754948.

[126] F. Gao, Q. Hu, J. Ma, and X. Han, "A simplified vehicle dynamics model for motion planner designed by nonlinear model predictive control," *Applied Sciences*, vol. 11, no. 21, Nov. 2021. doi: 10.3390/app11219887.

[127] K. Reeves, A. Montazeri and C. J. Tayor, "Validation of a Hybrid Electric Vehicle dynamics model for energy management and vehicle stability control," 2016 IEEE 25th International Symposium on Industrial Electronics (ISIE), 2016, pp. 849-854, doi: 10.1109/ISIE.2016.7745000.

[128] S. Oman, "Dynamic characteristics of vehicles," [Online]. Available: https://web.fs.uni-

lj.si/kserv/images/upload/2_Pedagoska_dejavnost/2_Stopnja/Dinamika_vozil/Dok umenti/Vaje/Dynamic-characteristics-of-vehicle.pdf

[129] B. Asad, T. Vaimann, A. Belahcen, A. Kallaste, A. Rassõlkin, and M. N. Iqbal, "The cluster computation-based hybrid fem– analytical model of induction motor for fault diagnostics," *Applied Sciences*, vol. 10, no. 21, pp. 1–15, Nov. 2020. doi: 10.3390/app10217572.

[130] L. Chen, J. Wang, P. Lazari, and X. Chen, "Optimizations of a permanent magnet machine targeting different driving cycles for electric vehicles," in *Proc. IEEE Int. Electr. Mach. Drives Conf.*, (*IEMDC*), 2013, pp. 855–862. doi: 10.1109/IEMDC.2013.6556198.

[131] E. Carraro, M. Morandin, and N. Bianchi, "Optimization of a traction PMASR motor according to a given driving cycle," in *Proc. IEEE Transp. Electrifi. Conf. Expo*, (*ITEC*), 2014, pp. 1-6. doi: 10.1109/ITEC.2014.6861838.

[132] P. Korta, L. V. Iyer, C. Lai, K. Mukherjee, J. Tjong, and N. C. Kar, "A novel hybrid approach towards drive-cycle based design and optimization of a fractional slot concentrated winding SPMSM for bevs," *IEEE Energy Convers. Congr. Expo.*, (*ECCE*), 2017, pp. 2086–2092. doi: 10.1109/ECCE.2017.8096415.

[133] D. Sitaram, H. L. Phalachandra, S. Gautham, H. V. Swathi, and T. P. Sagar, "Energy efficient data center management under availability constraints," in *Proc. 9th Annu. IEEE Int. Syst. Conf.*, (*SysCon*), 2015, pp. 377–381. doi: 10.1109/SYSCON.2015.7116780.

VITA AUCTORIS

NAME:	**Tim Stachl**
PLACE OF BIRTH:	Braunau am Inn, AUT
YEAR OF BIRTH:	1997
EDUCATION:	Riverside Secondary School, Windsor, ON, 2015
	University of Windsor, B.A.Sc., Windsor, ON, 2019